



Norwegian University of  
Science and Technology

# Numerical Investigation of Flow Field subject to Vibrating Structure

**Sondre Leonhardsen**

Master of Energy and Environmental Engineering

Submission date: June 2017

Supervisor: Ole Gunnar Dahlhaug, EPT

Co-supervisor: Chirag Trivedi, EPT

Carl Bergan, EPT

Bjørn Winther Solemslie, EPT

Norwegian University of Science and Technology

Department of Energy and Process Engineering



EPT-M-2017-47

**MASTER THESIS**

for

Student Sondre Leonhardsen

Spring 2017

*Numerical Investigation of Flow Field subject to Vibrating Structure*  
*Numerisk analyse av strømningsfeltet i en vibrerende struktur*

**Background**

Hydropower is an important and stable source of renewable energy. Hydropower contributes over 21% of global electricity generation. Hydraulic turbines are the important component of a hydropower plant and convert available hydropower into electricity. Variations in either power generation from wind, solar or other power generators or demand directly affects the hydraulic turbines. Such turbines must constantly adjust their power output to accommodate these variations irrespective of the design point, the best efficiency point (BEP). Hydraulic turbines include stationary and rotating components. The interaction of the components, mainly between the runner blades and guide vanes, is critical when the frequency of the rotor-stator interaction approaches the runner natural frequency. This causes resonance in the turbine runner and the premature failure of the blades. Several turbines have experienced such problems in the last few years. When blades are subject to vibration and the main challenge is how to control forced vibration of the blades. Basic mechanics behind the fluid-structure coupling is not completely understood, and the current work will help to understand the vortex shedding frequency occurring at the trailing edge of a hydrofoil.

**Objectives**

- I. Investigate and identify where the cavitation occurs in the existing cascade test rig at the Waterpower laboratory.
- II. Investigate vortex shedding frequency and find a new blade geometry for the cascade test rig where the lock in frequency will occur outside the velocity range of the tests.

**The following tasks are to be considered:**

1. Literature study on the vortex shedding at the trailing edge of hydro profiles utilized in high head Francis turbines
2. Parametric study of a hydrofoil in order to see the relationship between geometry and vortex shedding frequency.
3. Investigate the vortex shedding frequency versus blade flutter
4. If there is time available: Investigate the vortex shedding frequency versus cavitation.
5. Previous and further work shall be submitted as a publication for the conference: 7<sup>th</sup> *International symposium on Current Research in Hydraulic Turbines (CRHT-VII)* at Kathmandu University in April 2017.

Within 14 days of receiving the written text on the master thesis, the candidate shall submit a research plan for his project to the department.

When the thesis is evaluated, emphasis is put on processing of the results, and that they are presented in tabular and/or graphic form in a clear manner, and that they are analyzed carefully.

The thesis should be formulated as a research report with summary both in English and Norwegian, conclusion, literature references, table of contents etc. During the preparation of the text, the candidate should make an effort to produce a well-structured and easily readable report. In order to ease the evaluation of the thesis, it is important that the cross-references are correct. In the making of the report, strong emphasis should be placed on both a thorough discussion of the results and an orderly presentation.

The candidate is requested to initiate and keep close contact with his/her academic supervisor(s) throughout the working period. The candidate must follow the rules and regulations of NTNU as well as passive directions given by the Department of Energy and Process Engineering.

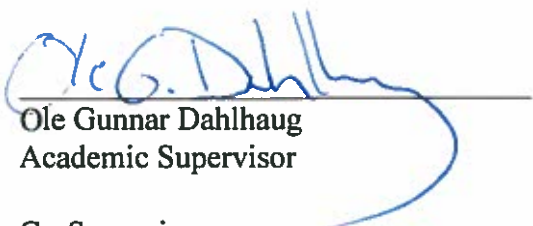
Risk assessment of the candidate's work shall be carried out according to the department's procedures. The risk assessment must be documented and included as part of the final report. Events related to the candidate's work adversely affecting the health, safety or security, must be documented and included as part of the final report. If the documentation on risk assessment represents a large number of pages, the full version is to be submitted electronically to the supervisor and an excerpt is included in the report.

Pursuant to "Regulations concerning the supplementary provisions to the technology study program/Master of Science" at NTNU §20, the Department reserves the permission to utilize all the results and data for teaching and research purposes as well as in future publications.

The final report is to be submitted digitally in DAIM. An executive summary of the thesis including title, student's name, supervisor's name, year, department name, and NTNU's logo and name, shall be submitted to the department as a separate pdf file. Based on an agreement with the supervisor, the final report and other material and documents may be given to the supervisor in digital format.

- Work to be done in the Waterpower laboratory
- Field work

Department of Energy and Process Engineering, 15. January 2017

  
Ole Gunnar Dahlhaug  
Academic Supervisor

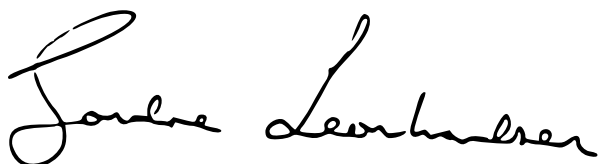
- Co-Supervisors:
- Chirag Trivedi
  - Carl Bergan
  - Bjørn Winther Solemslie

# Preface

This master thesis has been written at the Waterpower Laboratory at the Department of Energy and Process Engineering as part of fulfilling the requirements of the Energy and Environmental Engineering program at the Norwegian University of Science and Technology. The work presented in this thesis has contributed to a research project called HiFrancis, where the credible prediction and identification of hydrodynamic damping and added mass of water in High-Head Francis turbines is among the main challenges. Some aspects of the work presented in this thesis are a continuation of the knowledge obtained in a Specialisation Project carried out in the autumn semester of 2016.

I would like to thank my supervisor, Professor Ole Gunnar Dahlhaug, for great discussions and an exciting, yet complex, problem. Through this year, I have gotten to know Chirag Trivedi, PostDoc at the Waterpower Laboratory, whom I want to make special thanks to for his availability, help with the numerical tools and for motivating me in this work. I also want to thank PostDoc Bjørn Winther Solemslie and PhD candidates Carl Werdelin Bergan, Erik Os Tengs, Einar Agnalt, Erik Volent and Igor Iliev for being great discussion partners. These people have thought me the power and limitations of both numerical and experimental techniques and the joy and challenges of research.

The trip to Nepal in April with participation at the *International Symposium on Current Research in Hydraulic Turbines - 7<sup>th</sup> series* at Kathmandu University with my fellow students at the Waterpower Laboratory, will forever be a great memory. The working environment at the Waterpower Laboratory has been above all expectations, thanks to all the great people there.

A handwritten signature in black ink, reading "Sondre Leonhardsen". The signature is written in a cursive, flowing style with a large initial 'S'.

Sondre Leonhardsen  
Trondheim, June 16, 2017



# Abstract

Hydraulic turbines are more often than before running at off-design conditions. The flow conditions outside the best efficiency point may increase the mechanical load, and hence fatigue, on the turbine blades. The flow-induced vibration caused by Rotor-Stator-Interaction (RSI) is one of the main issues as the frequency of the pressure pulsations caused by RSI often lie close to the natural frequency of the turbine. The interaction between fluid and structure during transient operation, are yet to be fully understood. Credible estimation of the added mass effect, natural frequencies and hydrodynamic damping is the main challenge.

A hydrofoil test rig was developed to better understand the interaction between fluid flow and structure. Experimental measurements showed large vibration amplitudes during the lock-in condition. The lock-in condition was present at flow velocities around 11 m/s and a frequency of 623 Hz. Another problem experienced during the experimental measurements was that cavitation occurred at velocities higher than 25 m/s.

The first objective of this master thesis was to move the lock-in condition to a lower flow velocity. The lock-in condition is experienced to occur for low flow velocities in High-Head Francis Turbines. Numerical fluid flow and structure analyses were conducted to design a new hydrofoil where the objective is met. The available measurement data from the experiment was used as a reference for the numerical model. Different trailing edge (TE) profiles were tested to increase the vortex shedding frequency of the hydrofoil. By changing the TE and move the chamfer point of the hydrofoil 100 mm closer to the leading edge (LE), the expected new lock-in condition velocity is around 7.9 m/s. Also, the vortex shedding amplitude is expected to be reduced to a tenth of the amplitude of the original design.

The second objective of this thesis was to investigate and identify cavitation in the test rig. Low-pressure zones of the flow around the hydrofoil were identified at the top and bottom of the LE and at the chamfer point. The formation of water vapour was found to mainly originate from the top of the LE. The amount of water vapour in the test section varied periodically with similar frequency as found in experimental observations. The vortex shedding frequency of the hydrofoil was lowered as water vapour was included in the domain.

**Keywords:** Hydropower, High-Head Francis turbines, Flow-Induced Vibration, Lock-In, CFD





# Sammendrag

Vannkraftturbiner operer oftere utenfor beste driftspunkt. Strømningen gjennom turbinen under slike driftsforhold kan øke den mekaniske belastningen på turbinbladene, som igjen fører til utmatting. Strømningsindusert vibrasjon forårsaket av rotor og stator interaksjon er en av hovedproblemene da frekvensen på trykkpulsasjonene forårsaket av interaksjonen ofte ligger nære turbinens egenfrekvens. Interaksjonen mellom fluid og struktur under transiente driftsforhold er ikke fullt forstått. Troverdige beregning av effekten av vannets masse, egenfrekvenser og hydrodynamisk demping er hovedutfordringene.

Et eksperimentelt oppsett med en hydrofoil ble utviklet for å bedre forstå interaksjonen mellom fluid og struktur. Eksperimentelle målinger viste store vibrasjoner under lock-in. Lock-in skjedde ved en hastighet på omkring 11 m/s og en frekvens på 623 Hz. Et annet problem som ble oppdaget under målingene var at kavitasjon oppstod ved hastigheter høyere enn 25 m/s.

Det første målet med denne masteroppgaven var å flytte lock-in til en lavere hastighet. Lock-in punktet ligger generelt omkring de lave hastighetene for turbiner. Numeriske strømnings- og strukturanalyser ble gjennomført for å designe en ny hydrofoil som tilfredsstillte målet. Tilgjengelige måledata har vært benyttet som referanse til den numeriske modellen. Ulike avløpsgeometrier for hydrofoilen ble testet med formål i å finne en avløpsgeometri som økte virvelavløsningen. Ved å endre avløpsgeometrien og flytte knekkpunktet til hydrofoilen 100 mm nærmere innløpsfronten, er det nye lock-in området forventet å ligge omkring 7.9 m/s. Amplituden på virvelavløsningen er i tillegg forventet å bli redusert til en tiendel av amplituden for det opprinnelige designet.

Det andre målet med oppgaven var å utforske og identifisere kavitasjonen observert under målingene. Lavtrykkssoner omkring hydrofoilen ble identifisert omkring innløpsfronten og det tykkeste punktet. Området hvor kavitasjonen stammet fra var i hovedsak på toppen av innløpsfronten. Mengden vanndamp i test-seksjonen varierte periodisk med samme frekvens som observert under eksperimentelle målinger. Virvelavløsningens frekvens viste seg å være lavere når kavitasjon ble inkludert i modellen.

**Nøkkelord:** Vannkraft, Høytrykks Francisturbiner, Strømningsindusert vibrasjon, Lock-In, CFD



# Contents

<b>1</b>	<b>Introduction</b>	<b>1</b>
1.1	Problem Statement and Objectives . . . . .	2
1.2	Outline . . . . .	2
<b>2</b>	<b>Theoretical Background and Summary of Previous Work</b>	<b>5</b>
2.1	The Francis Turbine . . . . .	5
2.1.1	Flow-Induced Vibration in High-Head Francis Turbines . . . . .	6
2.2	Flow Past Bluff Bodies . . . . .	8
2.2.1	The Formation of Vortices . . . . .	8
2.2.2	Identification of a Vortex . . . . .	10
2.2.3	Trailing Edge Profiles of Hydro Turbine Blades . . . . .	11
2.2.4	The Lock-in Effect . . . . .	15
2.3	Turbulent Boundary Layers . . . . .	16
2.3.1	Turbulence Modelling . . . . .	16
2.4	Cavitation . . . . .	19
2.4.1	Bubble Dynamics . . . . .	20
<b>3</b>	<b>Methodology</b>	<b>21</b>
3.1	The Cascade Test Rig . . . . .	21
3.2	Numerical Fluid Flow Investigations . . . . .	23
3.2.1	Design Strategy . . . . .	23
3.2.2	Computational Domain . . . . .	26
3.2.3	Numerical Setup . . . . .	27
3.2.4	Mesh Quality and Convergence . . . . .	28
3.2.5	Data Analysis . . . . .	31
3.2.6	Results Design Step 1 . . . . .	32
3.2.7	Final Numerical Model . . . . .	35
3.2.8	Cavitation Modelling . . . . .	40
3.3	Natural Frequencies . . . . .	43
<b>4</b>	<b>Results and Discussion</b>	<b>47</b>
4.1	Design of a New Hydrofoil Geometry . . . . .	47
4.1.1	Final Hydrofoil Design . . . . .	47
4.1.2	Change of Natural Frequency . . . . .	56
4.1.3	New Lock-In Condition . . . . .	58
4.2	Cavitation . . . . .	59

4.3	General Discussions . . . . .	66
<b>5</b>	<b>Conclusions</b>	<b>69</b>
<b>6</b>	<b>Further Work</b>	<b>71</b>
	<b>Bibliography</b>	<b>73</b>
	<b>Appendices</b>	
	Appendix A: Pressure Loss Calculation . . . . .	
	Appendix B: Modal Analysis Mesh Independence . . . . .	A-2
	Appendix C: Paper Submitted to the <i>International symposium on Current Research in Hydraulic Turbines (CHRT-VII)</i> . . . . .	A-4
	Appendix D: Risk Assessment . . . . .	A-15

# List of Figures

2.1	Francis turbine cross-section. . . . .	5
2.2	Classification of turbines based on specific speed. . . . .	6
2.3	Guide vane position at different operating conditions. . . . .	7
2.4	Rolling-up of shear layers behind a bluff body. . . . .	9
2.5	Flow regimes. . . . .	10
2.6	Experimental results from Donaldson. . . . .	12
2.7	Trailing edge profiles investigated by Heskestad and Olberts. . . . .	13
2.8	Trailing edge profiles used for the blades of hydraulic turbines. . . . .	14
2.9	The lock-in condition. . . . .	15
2.10	Cavitation erosion in a Francis turbine. . . . .	19
3.1	Cross-section of the cascade test rig. . . . .	21
3.2	The hydrofoil design in the cascade test rig with measures. . . . .	22
3.3	The hydrofoil part. . . . .	22
3.4	Vibration amplitude of hydrofoil as function of velocity. . . . .	23
3.5	Trailing edge designs with constant thickness hydrofoils. . . . .	24
3.6	Work flow design strategy. . . . .	26
3.7	Monitor points in the fluid domain. . . . .	28
3.8	Final 2D mesh and blocking. . . . .	29
3.9	Results mesh convergence study. . . . .	30
3.10	Velocity contour of original hydrofoil at 10 m/s and monitor points. . . . .	31
3.11	Results constant thickness hydrofoil study. . . . .	32
3.12	FFT original hydrofoil. . . . .	33
3.13	FFT hydrofoil <b>a</b> . . . . .	33
3.14	FFT hydrofoil <b>b</b> . . . . .	34
3.15	FFT hydrofoil <b>c</b> . . . . .	34
3.16	New mesh at trailing edge. . . . .	37
3.17	Results turbulence model test with fitting line. . . . .	38
3.18	Results time step dependence test. . . . .	39
3.19	FFT at varying time step. . . . .	39
3.20	Hydrofoil with chamfer and proposed TE. . . . .	40
3.21	Cavitation in the cascade test rig. . . . .	41
3.22	Cavitation grey scale intensity. . . . .	42
3.23	Geometrical model used in modal analysis. . . . .	44
4.1	Absolute pressure signal of original hydrofoil. . . . .	48

4.2	Intensity plot of FFT for original hydrofoil design. . . . .	48
4.3	Absolute pressure signal of chamfered hydrofoil with proposed trailing edge.	49
4.4	Intensity plot of FFT for chamfered hydrofoil with proposed trailing edge.	49
4.5	Hydrofoil with moved chamfer point and proposed trailing edge. . . . .	50
4.6	Absolute pressure signal of hydrofoil with moved chamfer point and proposed trailing edge. . . . .	50
4.7	Intensity plot of FFT for hydrofoil with moved chamfer and proposed trailing edge. . . . .	51
4.8	Dominant frequencies of final hydrofoil design. . . . .	52
4.9	Velocity contour. . . . .	53
4.10	$\lambda_2$ -criterion with velocity contour. . . . .	54
4.11	Absolute pressure contour. . . . .	56
4.12	Modal shapes original and new hydrofoil. . . . .	57
4.13	New lock-in flow velocity. . . . .	59
4.14	Absolute pressure signal of original hydrofoil at 14 m/s. . . . .	60
4.15	Intensity plot of FFT for original hydrofoil at 14 m/s. . . . .	60
4.16	Absolute pressure signal of original hydrofoil with cavitation model at 14 m/s. . . . .	61
4.17	Water vapour volume fraction contour. . . . .	62
4.18	Intensity plot of FFT for original hydrofoil with cavitation. . . . .	63
4.19	Total pressure contour cavitation. . . . .	64
4.20	Absolute pressure contour cavitation. . . . .	66
6.1	Pressure tank and piping system. . . . .	
6.2	Mesh used for the modal analysis of the new hydrofoil design. . . . .	A-2
6.3	Results from modal analysis mesh independence test. . . . .	A-3

# List of Tables

3.1	Aluminium alloy, material properties. . . . .	22
3.2	Numerical settings. . . . .	27
3.3	Mesh statistics and quality measures. . . . .	30
3.4	Average $y^+$ -value at the hydrofoil surface. . . . .	35
3.5	Mesh comparison after change of first spacing. . . . .	36
3.6	Mesh statistics and quality measures new mesh. . . . .	37
3.7	Final numerical settings. . . . .	40
3.8	Structural steel material properties. . . . .	44
4.1	Dominant frequencies for original hydrofoil. . . . .	49
4.2	Dominant frequencies of hydrofoil with moved chamfer and proposed trailing edge. . . . .	51
6.1	Input data pressure loss calculation. . . . .	A-1





# Abbreviations

BEP	Best Efficiency Point
CAD	Computer Aided Design
CFD	Computational Fluid Dynamics
FEM	Finite Element Method
FFT	Fast Fourier Transform
FSI	Fluid-Structure Interaction
LDV	Laser Doppler Vibrometri
LE	Leading Edge
LES	Large Eddy Simulation
NTNU	Norwegian University of Science and Technology
RANS	Reynolds-Averaged Navier-Stokes
SAS	Scale-Adaptive Simulation
SST	Shear Stress Transport
TE	Trailing Edge



# Nomenclature

$\delta'$	Virtual boundary layer thickness	m
$\mu$	Dynamic viscosity, for water $\mu = 1.002 \cdot 10^{-3}$ Pa $\cdot$ s at 20° C	Pa $\cdot$ s
$\mu_t$	Eddy viscosity	kg/(m $\cdot$ s)
$\nu$	Kinematic viscosity, for water $\nu = 1.004 \cdot 10^{-6}$ m <sup>2</sup> /s at 20° C	m <sup>2</sup> /s
$\Omega$	Specific speed	-
$\omega$	Turbulent frequency	1/s
$\rho$	Fluid density, for water $\rho = 1000$ kg/m <sup>3</sup>	kg/m <sup>3</sup>
$\sigma_B$	Surface tension of vapour bubble	kg/s
$\tau$	Shear stress	Pa
$\tau_w$	Wall shear stress	Pa
$\mathbf{V}$	Velocity vector composed of components $u$ , $v$ and $w$	m/s
$B$	Relative frequency based on geometrical trailing edge profile	-
$f_s$	Vortex shedding frequency	Hz
$f_{rotor}$	Frequency of pressure pulsations caused by rotor-stator interaction experienced by the rotor	Hz
$f_{stator}$	Frequency of pressure pulsations caused by rotor-stator interaction experienced by the stator	Hz
$g$	Gravitational acceleration, $g = 9.81$ m/s <sup>2</sup>	m/s <sup>2</sup>
$H$	Head	m
$k$	Turbulent kinetic energy	m <sup>2</sup> /s <sup>2</sup>
$L$	Characteristic length	m
$n$	Rotational speed	Hz
$p$	Pressure	Pa

$p_B$	Pressure within vapour bubble	Pa
$p_\infty$	External pressure infinitely far away	Pa
$p_{abs}$	Absolute pressure	Pa
$p_{atm}$	Atmospheric pressure, 101 325 Pa	Pa
$p_{vap}$	Vapour pressure	Pa
$Q$	Flow rate	m <sup>3</sup> /s
$R_B$	Radius of vapour bubble	m
$Re$	Reynolds number	-
$St$	Strouhal number	-
$T$	Temperature	°C
$t$	Time	s
$t_b$	Blade thickness	m
$U_\infty$	Free stream (inflow) velocity	m/s
$U_f$	Friction velocity	m/s
$V$	Velocity	m/s
$y^+$	Dimensionless wall distance	-
$Z_b$	Number of runner blades	-
$Z_{gv}$	Number of guide vanes	-

# 1 Introduction

Global climate change due to human activity is a major concern today. The transition from fossil fuels to renewable energy sources is part of the solution to this problem. As a consequence, an increasing share of the world's electricity production comes from an intermittent energy source, like solar, wind and tidal energy. This, in addition to the rapid introduction of new technology, leads to more instability in the electric grid. In Norway, a country where over 95 % of the electric power generation comes from hydro, hydropower plants contributes to the stabilisation of the electric grid because of its regulative benefits [1]. Hydropower plants must constantly adjust their power output to compensate for voltage and frequency instabilities in the electric grid. The need for stabilisation of the electric grid has forced hydropower plants to run at off-design conditions, outside the Best Efficiency Point (BEP), more frequently than before [2].

The secure and reliable operation of a hydropower plant highly depends on the flow conditions inside the hydraulic turbine runner. Outside the best efficiency point, periodic flow phenomena can be amplified, which again can cause damage to mechanical equipment. The interaction between the stationary and rotating part of the runner can induce high-amplitude pressure pulsations hitting the runner blades. These are susceptible to crack formation as the fatigue cycles exceed the threshold limit [3]. In High-Head Francis turbines the frequency of these pressure pulsations lies close to the natural frequency of the runner, which have resulted in catastrophic failures [4, 5].

The problems related to the off-design operation have been experienced for both old and newly installed turbines. As runner blades are made thinner to increase hydraulic efficiency and lower material cost, the interaction between fluid and structure is seen to cause increased vibration amplitudes and damage to the blades [6]. Numerical tools are used to optimise the runner design both on the efficiency and material cost. It is apparent that the credible estimation of the added mass of water, the hydrodynamic damping and the natural frequencies of runners subject to varying flow conditions is a challenge [7].

To better understand the above-mentioned flow and associated mechanical characteristics of the turbine blade, a hydrofoil test rig, the cascade test rig, has been developed at the Waterpower Laboratory at the Norwegian University of Science and Technology (NTNU). The test rig consists of a hydrofoil constrained at each end in a square pipe test section. Piezoelectric actuators provide forced excitation of the blade to imitate the vibration caused by i.e. RSI. The study of this hydrofoil, subject to varying flow conditions, is expected to increase the knowledge on how fluid and structure interacts in a hydraulic

turbine.

## 1.1 Problem Statement and Objectives

Measurements conducted on the cascade test rig revealed excessive vibrations during the lock-in condition. The lock-in condition was apparent at flow velocities around 11 m/s. This, in addition to the formation of water vapour, cavitation, at flow velocities above approximately 25 m/s, complicates the study of fluid-structure interaction (FSI) in the test rig. It is expected that by changing the geometry of the hydrofoil, both experienced problems may be avoided.

The objectives of this thesis is related to both the lock-in condition and the occurrence of cavitation in the cascade test rig. The following objectives are addressed:

- Investigate the vortex shedding frequency and find a new blade geometry for the cascade test rig where the lock-in frequency will occur outside the velocity range of the tests
- Investigate and identify where the cavitation occurs in the existing cascade test rig

The lock-in condition occurs at low flow velocities in High-Head Francis turbines [4]. The velocity range of the test rig lie between 0 and 40 m/s, and the intention is to move the lock-in point to a lower flow velocity. This is achieved by either increasing the vortex shedding frequency, lower the natural frequency or a combination of both.

A literature study on the relation between hydraulic turbine blade geometry and vortex shedding frequency will serve as a foundation for computational fluid dynamics (CFD) and numerical mechanical investigations to be conducted on the cascade test rig. Different trailing edge (TE) profiles will be tested to increase the vortex shedding frequency, and hence move the lock-in condition to a lower flow velocity.

The natural frequency of the cascade test rig will also be investigated. The design of the new hydrofoil may be changed in a way that lower this frequency. However, the length and thickness of the existing hydrofoil is not to be changed drastically. These dimensions are chosen such that conditions both the flow and structure is exposed to, are similar to what hydraulic turbine blades are subject to in High-Head Francis Turbines.

Cavitation is investigated by use of the Rayleigh-Plesset cavitation model, and the relationship between cavitation and vortex shedding frequency is considered in the numerical fluid flow studies.

## 1.2 Outline

Chapter 2 will present the relevant theoretical background together with a summary of previous work on the design of the trailing edge of hydraulic turbine blades. In chapter 3

the methods used to address the objectives of this thesis are presented. This chapter also includes some experimental results which support the methodology. Chapter 4 presents the results obtained from the numerical fluid flow and mechanical investigations and discusses these results. Conclusive remarks are presented in chapter 5, and further work in the studied topics is discussed in Chapter 6.

Additional information supporting the methods used are given in Appendix A, and B. Appendix C present the article submitted to the *International Symposium on Current Research in Hydraulic Turbines - 7<sup>th</sup> series* arranged at Kathmandu University in Nepal in April 2017. A risk assessment performed on the work presented in this master thesis is attached in Appendix D.





## 2 Theoretical Background and Summary of Previous Work

### 2.1 The Francis Turbine

The turbine is an important component of a hydropower plant. Hydraulic turbines are divided between impulse and reaction type turbines. The Pelton turbine, mainly in use at high heads, is the most common impulse type turbine. The Francis and Kaplan type turbine are both common reaction type turbines operating at medium and low heads respectively. Figure 2.1 show a cross-section of a Francis turbine.

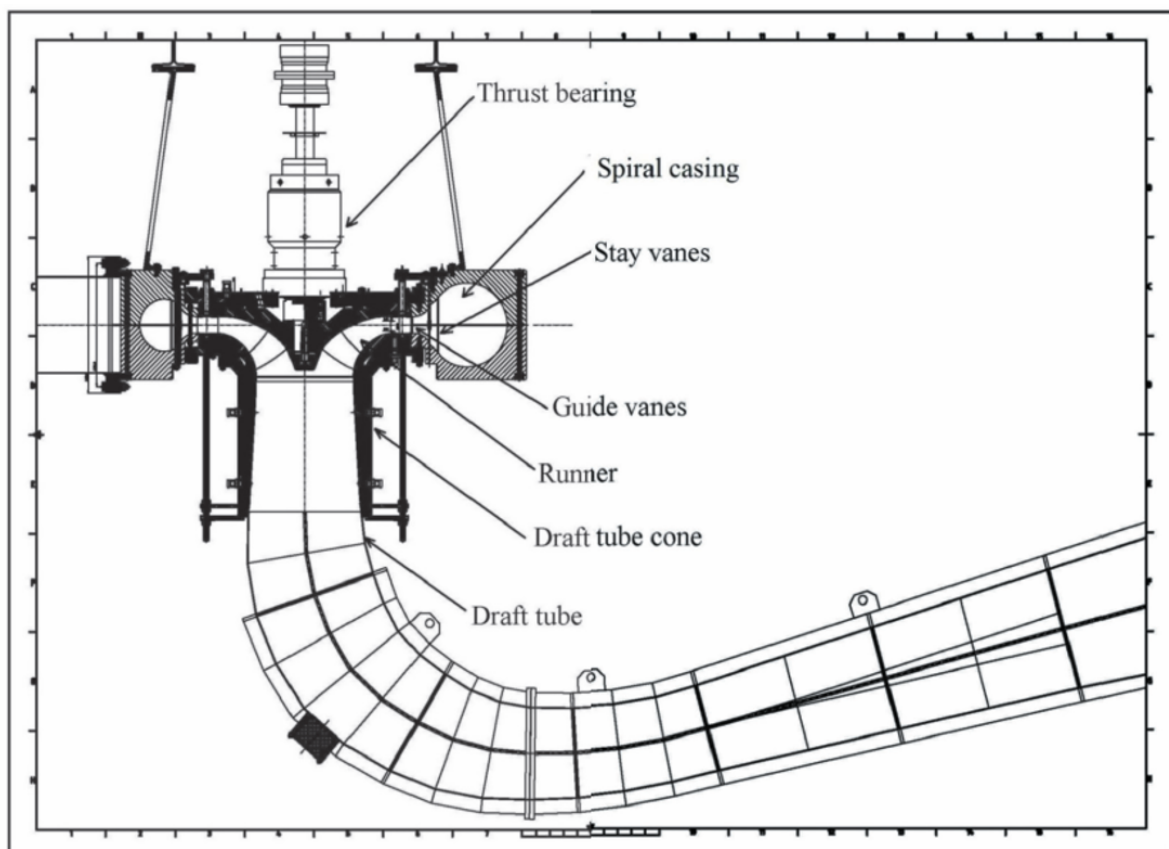


Figure 2.1: Francis turbine cross-section, adapted from [8]. Specific speed  $\Omega = 0.27$ .

The Francis turbine is a complex geometrical structure converting both kinetic and potential energy to axial torque [9]. The Francis turbine consists of different components. The spiral casing leads the water from the penstock to different radial positions around the turbine. The stay and guide vanes direct the water to the runner blades. The guide vanes are adjustable and control the flow. After the energy is extracted in the turbine runner, the flow goes into the outlet draft tube.

The shape of a Francis runner is dependent on both the head and flow. The specific speed of the turbine, presented in equation 2.1, is a characteristic number used to determine the geometrical design of the turbine runner.

$$\Omega = \frac{2\pi n \sqrt{Q}}{(2gH)^{\frac{3}{4}}} \quad (2.1)$$

Figure 2.2 show how the shape and choice of turbine depend on the specific speed. As Francis turbines are applicable for a wide range of specific speeds, they are divided among High-, Medium- and Low-Head. The division of the three is roughly as presented in the figure, whereas low specific speed yields high head.

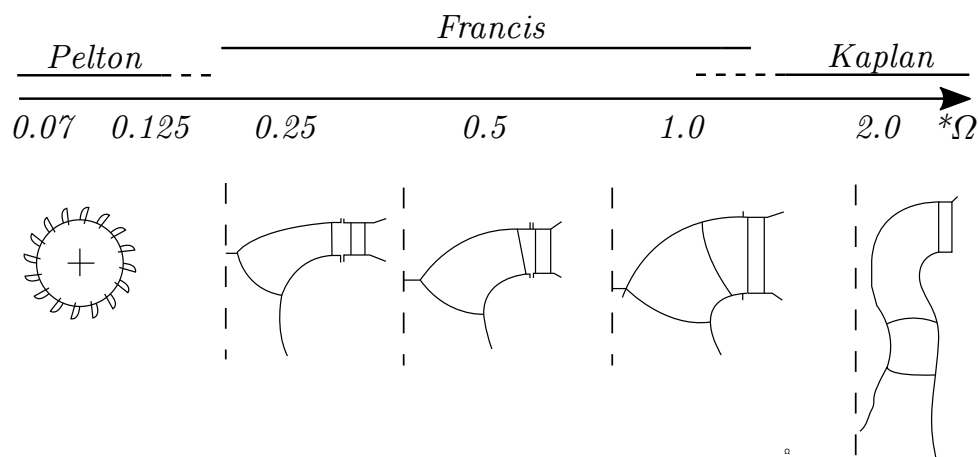


Figure 2.2: Classification of turbines based on specific speed, adapted from [10]. The superscript \* denotes the best efficiency point.

### 2.1.1 Flow-Induced Vibration in High-Head Francis Turbines

Hydraulic turbines experience flow-induced vibration from various flow phenomena [3]. Among the most important ones are:

- Draft tube vortex rope
- Von Karman vortices
- Turbulence
- Cavitation
- Rotor-Stator Interaction

The frequency of these phenomena varies greatly. From low-frequency draft tube vortex ropes to high-frequency Von Karman vortices. The frequency of the interaction between the stationary and rotating parts of a turbine is susceptible to coincide with the natural frequency of the runner. In High-Head Francis turbines the radial clearance gap between the guide vane and turbine runner is lower than for low-head turbines. The clearance gap affects the frequency of the pressure pulsations caused by RSI and is found to often lie close to the natural frequency for High-Head Francis turbines [4].

The clearance gap between guide vanes and runner blades are dependent on the operating condition. During part load, the gap is bigger, whereas during full load the gap is at its minimum. Figure 2.3 illustrates how the flow hits the runner blade at part load, BEP and at full load.

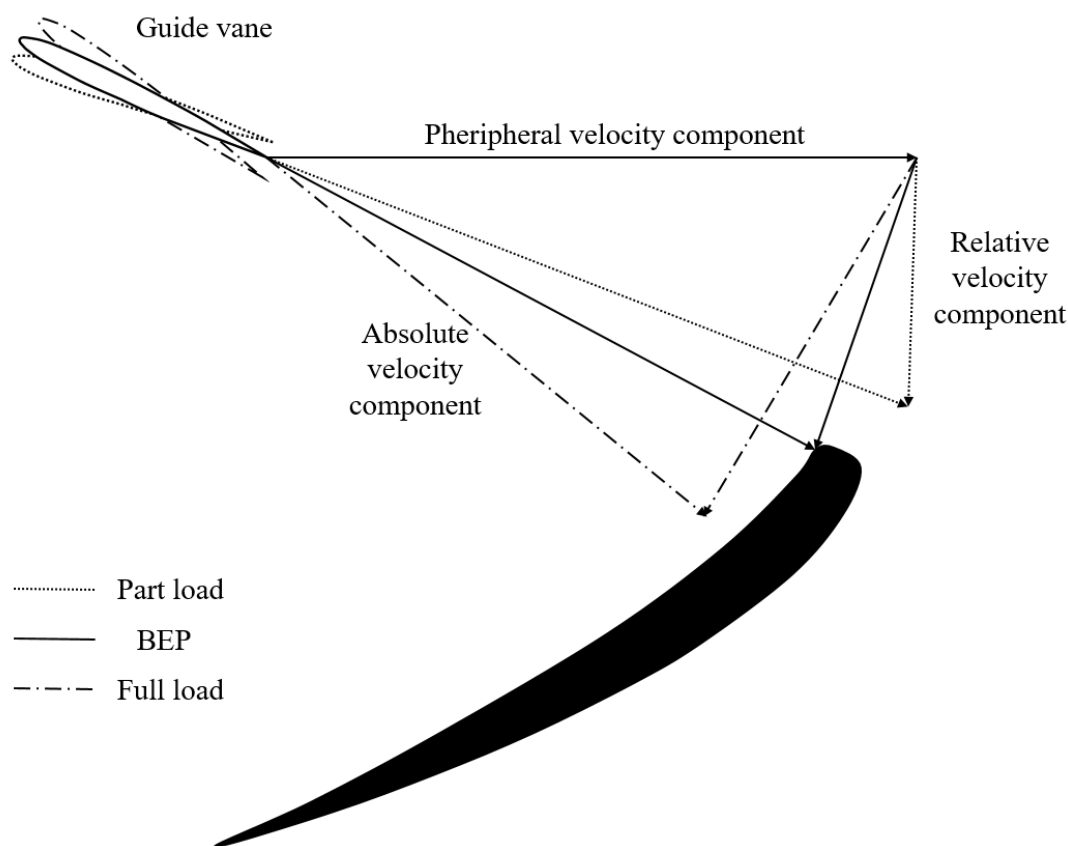


Figure 2.3: Guide vane position at different operating conditions.

When the angle of the guide vanes is adjusted during part or full load, the relative velocity component will hit the turbine blades at a less optimal angle which may lead to increased vibration. When the gap between the guide vane and the rotating turbine is decreased, at full load, the amplitude of the pressure oscillations produced by the rotor-stator interaction is increased [11].

The stationary guide vanes and rotating turbine blades are subject to pressure pulsations caused by RSI at different frequencies. The frequency experienced by the guide vanes

depends on the number of runner blades and Vice Versa as shown in equation 2.2 and 2.3 respectively.  $Z_b$  and  $Z_{gv}$  denotes the number of runner blades and guide vanes respectively.

$$f_{stator} = Z_b \cdot n \quad (2.2)$$

$$f_{rotor} = Z_{gv} \cdot n \quad (2.3)$$

## 2.2 Flow Past Bluff Bodies

Fluid flow instabilities develop in the region behind bluff bodies above certain Reynolds numbers. These instabilities lead to the formation of periodic shedding of vortices which may cause damage in hydraulic machines [12].

### 2.2.1 The Formation of Vortices

Separation of fluid flow at the surface of a body occurs due to adverse pressure gradients in the boundary layer close to the body surface. At the surface of the body, the equation governing fluid motion may be written as in equation 2.4. Backflow and fluid flow separation is experienced when  $\tau_w = 0$ .

$$\frac{1}{\rho} \frac{\partial \tau}{\partial y} \Big|_{wall} = \nu \frac{\partial^2 u}{\partial^2 y} \Big|_{wall} = \frac{1}{\rho} \frac{\partial p}{\partial x} \Big|_{wall} \quad (2.4)$$

As flow is separated at the surface of a body, shear layers develop from the separation points. These rolls up and forms vortices in the wake of the body [13]. These vortices continue to grow until flow instabilities force them to alternately travel downstream.

Gerrard (1966) describes the region behind bluff bodies and the formation of vortices in this region in full detail [14]. Figure 2.4 illustrates the interaction between two separated shear layers as a vortex is about to move downstream. This interaction is the key element in the formation of a von Karman vortex street. As a vortex become strong enough, it draws an opposing shear layer with it and starts to travel downstream. The figure illustrates the opposing shear layers movement. The opposing shear layer is entrained into the downstream travelling vortex (a), while some of it is entrained into the separated shear layer (b) and the remaining is drawn towards and feeds the remaining vortex (c).

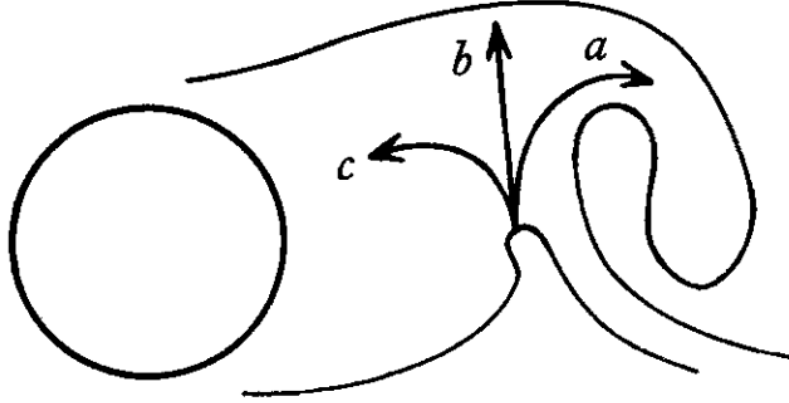


Figure 2.4: Filament lines illustrating the rolling-up of shear layers behind a bluff body, adapted from [14].

Roshko [15] showed that the frequency of the alternating shedding of vortices increase if the size of the formation region is reduced. When shear layers are brought closer together, the time between, in which their interaction leads to the downstream travelling of a vortex, is decreased.

Lienhard (1966) collected and summarised scattered information about the accurate prediction of lift, drag and vortex shedding frequency for circular cylinders [16]. Figure 2.5 presents different flow regimes in the wake of a circular cylinder. The Reynolds number identifying these regimes is presented in equation 2.5.

$$Re = \frac{VL}{\nu} \quad (2.5)$$

At  $Re < 5$  the flow regime may be represented by potential flow theory only. As the Reynolds number increase, the flow separates and forms an unsteady laminar vortex street. During transitional Reynolds numbers, the flow in the wake exhibits a chaotic behaviour with no clear vortex street pattern. As a fully turbulent flow is developed, a turbulent vortex street is apparent. Lienhard noted that fully turbulent vortex streets are diffuse and that there are many frequencies present in the flow. Compared to the laminar vortex street, the turbulent vortex street has a different character and physical meaning. The dominant frequency must be reported when speaking of a vortex street frequency for fully turbulent flows.

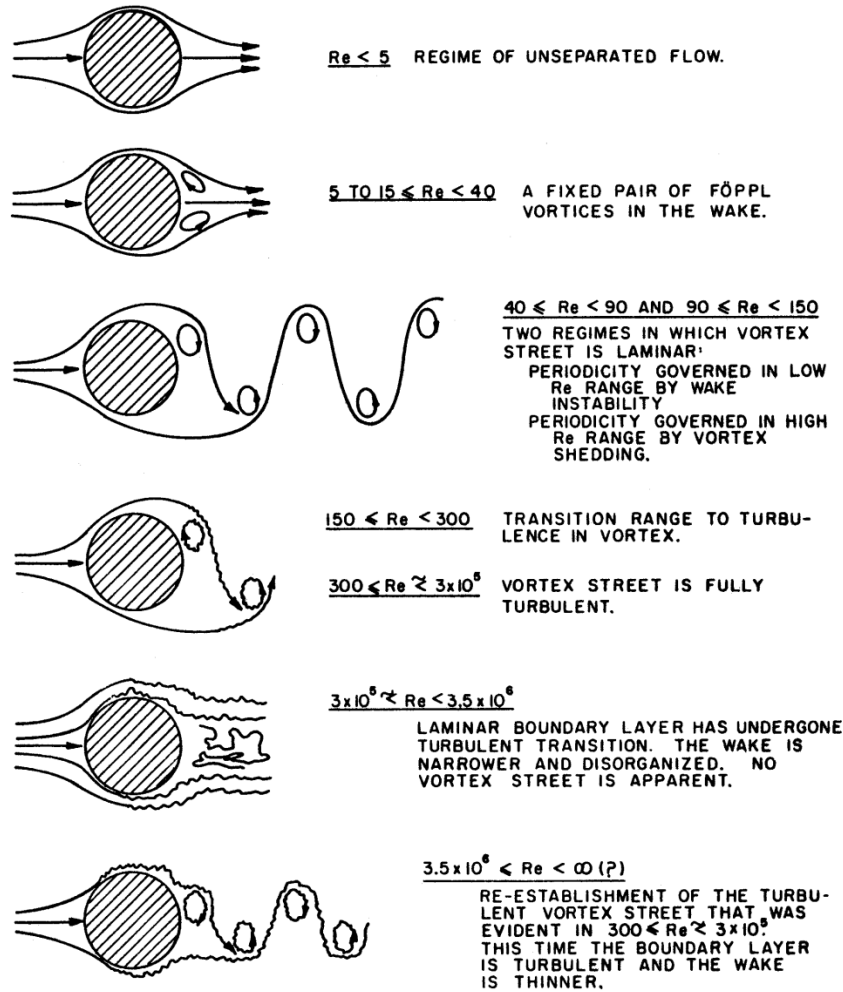


Figure 2.5: Flow regimes, adapted from [16].

A dimensionless number, the Strouhal number, represented in equation 2.6, is a relative parameter describing the vortex shedding frequency behind a bluff body relative to the free stream velocity.

$$St = \frac{f_s L}{U_\infty} \quad (2.6)$$

For cylinders, this number is found empirically to be 0.2 for a wide range of Reynolds numbers. In a Reynolds number range where the Strouhal number is constant, the vortex shedding frequency will be proportional to the free stream velocity.

## 2.2.2 Identification of a Vortex

A vortex is a highly visual fluid flow phenomena. Several mathematical definitions exist in the identification of a vortex, but none has been universally accepted. The main problem lies in defining the vortex at a finite structure with clear edges [17].

The most used identification methods are the methods based on the velocity gradient tensor. Among these are the:

- Q-criterion
- $\Delta$ -criterion
- $\lambda_2$ -criterion
- Swirling strength criterion

The velocity gradient tensor, presented in equation 2.7 in index notation, is a second order tensor which may be decomposed into a symmetric and skew-symmetric part,  $S_{ij}$  and  $Q_{ij}$ .

$$D_{ij} = \frac{\partial u_i}{\partial x_j} = S_{ij} + \Omega_{ij} = \frac{1}{2} \left( \frac{\partial u_i}{\partial x_j} + \frac{\partial u_j}{\partial x_i} \right) + \frac{1}{2} \left( \frac{\partial u_i}{\partial x_j} - \frac{\partial u_j}{\partial x_i} \right) \quad (2.7)$$

The characteristic equation for the velocity gradient is as presented in equation 2.8, where P, Q and R are velocity gradient tensor invariants.

$$\lambda^3 + P\lambda^2 + Q\lambda + R = 0 \quad (2.8)$$

The  $\lambda_2$ -criterion is one of the methods most used to identify a vortex. The method was developed by Jeong and is based on finding a pressure minimum [18]. Jeong computed the eigenvalues of the characteristic equation 2.8 and ordered these in the way presented in equation 2.9.

$$\lambda_1 \geq \lambda_2 \geq \lambda_3 \quad (2.9)$$

The  $\lambda_2$ -criterion states that a point in the velocity field whereas at least two of the eigenvalues are negative, is part of a vortex core. Based on the ordering of eigenvalues, this is equivalent to saying  $0 \geq \lambda_2$ , and hence the name the  $\lambda_2$ -criterion.

### 2.2.3 Trailing Edge Profiles of Hydro Turbine Blades

The foundation of the work done on the trailing edge profiles of hydro turbine blades was laid by Gongwer (1952), Donaldson (1956) and Heskestad and Olberts (1960) [19, 20, 21]. Through his article *A Study of Vanes Singing in the Water*, Gongwer presented a correction to the Strouhal number for flow past hydrofoils, equation 2.10. However, Gongwer found that the Strouhal number was constant, and equal to 0.19, for a wide range of Reynolds numbers which suggest that the vortex shedding frequency,  $f_s$ , is proportional to the free stream velocity,  $U_\infty$ , and inversely proportional to the trailing edge thickness,  $t_b$ .

$$St = \frac{f_s(t_b + \delta')}{U_\infty} \quad (2.10)$$

$\delta'$  is empirically determined as a fraction 0.643 of the turbulent boundary layer displacement thickness, and is defined as in equation 2.11.

$$\delta' = 0.643 \cdot \frac{1}{8} \cdot \frac{0.37L}{Re_L^{\frac{1}{5}}} \quad (2.11)$$

In the article *Hydraulic-Turbine Runner Vibration* Donaldson presents the results from his experimental investigations on hydrofoil trailing edge profiles, including his characteristic 'dovetail' trailing edge. He investigated the vortex shedding characteristics of several trailing edges. The results from his investigations are presented in Figure 2.6, where the 'dovetail' trailing edge is the one numbered 10. Donaldson did not find the trailing edge profile to affect the vortex shedding frequency significantly but found that the vortex shedding amplitude was highly dependent on the trailing edge profile.

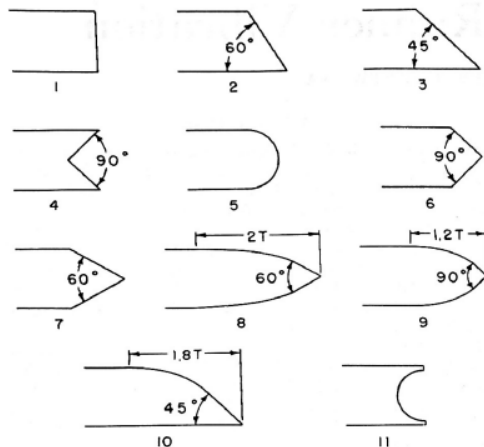


FIG. 1 TRAILING-EDGE SHAPES

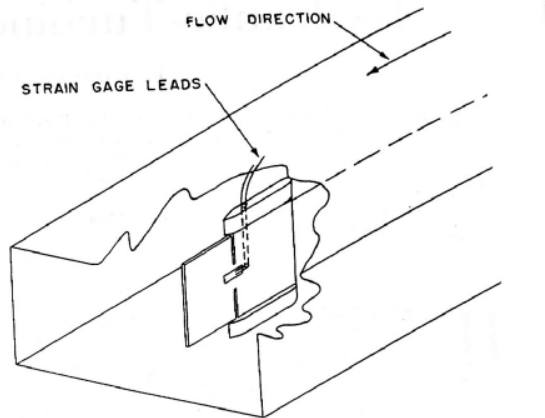


FIG. 2 SKETCH OF TEST PLATE IN WATER CHANNEL

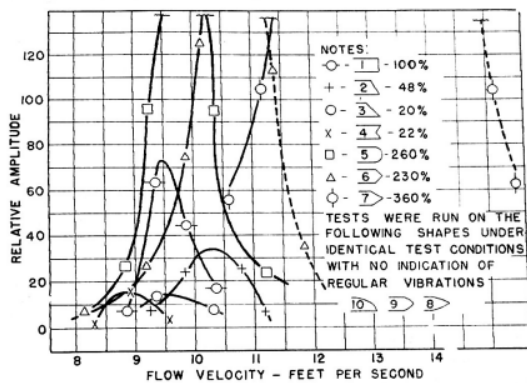


FIG. 3 VIBRATION AMPLITUDES OF VARIOUS TRAILING-EDGE SHAPES

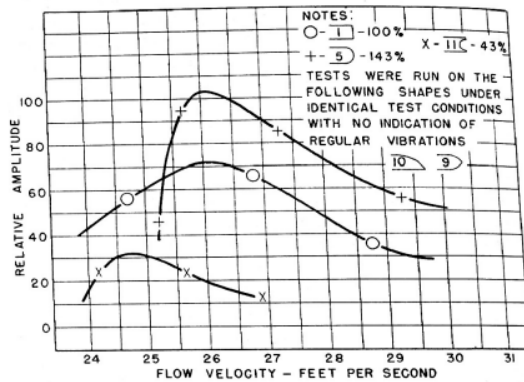


FIG. 4 VIBRATION AMPLITUDES OF TRAILING-EDGE SHAPES AT HIGHER FLOW VELOCITIES

Figure 2.6: Experimental setup and results from the experiments performed by Donaldson [20].

Heskestad and Olberts performed a more systematic investigation of the vortex shedding characteristics in their paper *Influence of Trailing-Edge Geometry on Hydraulic-Turbine-Blade Vibration Resulting From Vortex Excitation*. The trailing edges they tested and the results from their tests are shown in Figure 2.7. What is apparent is that Heskestad and Olbert's findings contradict the findings of Gongwer and Donaldson. The vortex shedding frequency seems to be dependent on the trailing edge profile.



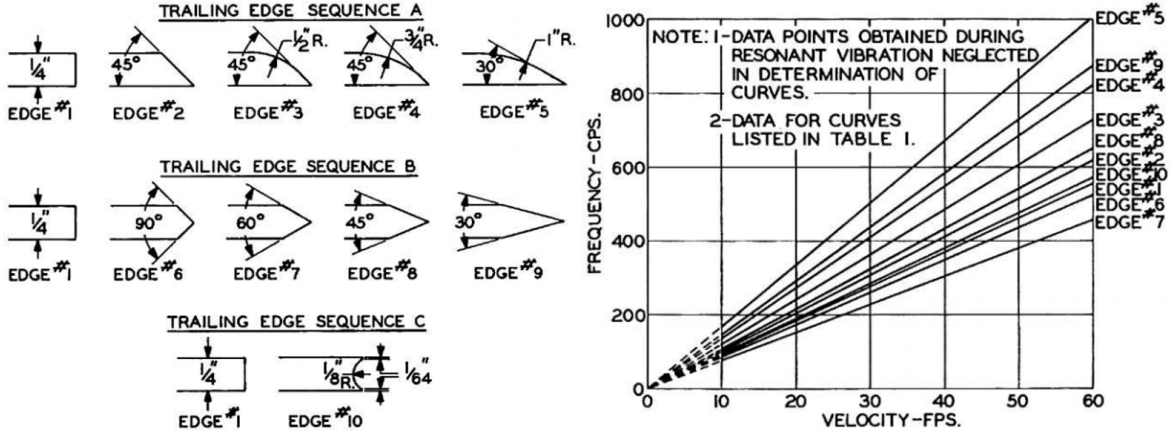


Figure 2.7: Trailing edge profiles investigated by Heskestad and Olberts together with resulting vortex shedding frequency versus velocity plot [21].

From the results obtained by Heskestad and Olberst, it is possible to define a new formulation of the Strouhal number based on the trailing edge profile. Together with the constants given in Figure 2.8, the equation 2.12 may be used to determine the Strouhal number of hydrofoils with different trailing edges [22].

$$St = \frac{100 f_s (t_b + \delta')}{B U_\infty} \quad (2.12)$$

Brekke [23] revised and simplified this formula where he assumed that the Strouhal number was constant, but that the vortex shedding frequency was dependent on the trailing edge profile as suggested by Heskestad and Olberts. The simplified formula by Brekke is presented in equation 2.13.

$$f = 190 \frac{B}{100} \frac{U_\infty}{(t_b + 0.56)} \quad (2.13)$$

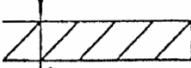
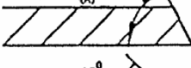
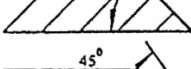
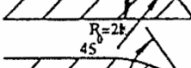
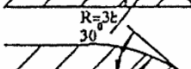
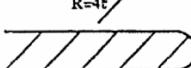
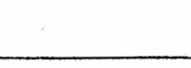
	A	B		A	B	
a	100 (100)	100		(0)		h
b	(48)			(0)		i
c	38 (20)	112		190 (230)	96	j
d	3 (0)	131		380 (360)	93	k
e	0	149		43	117	l
f	0	181		0	159	m
g	(260)			31 (43)	103	n

Figure 2.8: Trailing edge profiles used for the blades of hydraulic turbines [23]. Design a is a reference where the parameter A describes the relative amplitude of the vortex shedding behind the body, and parameter B describes the relative vortex shedding frequency.

Although the research presented in the previous paragraphs mainly originates from the 1950-1960's, the physics of the flow around a hydrofoil are still investigated and not yet fully understood. Many of these studies involve forced excitation by piezoelectric actuators which may imitate vibration caused by rotor-stator interactions [24, 25, 26].

Ausoni et. al. has published several articles on the formation of vortices at the trailing edge of hydrofoils [27, 28, 29]. Among his work is the investigation of the effect of an oblique trailing edge profile [30]. He found that by forcing the collision of vortices at the trailing edge, the flow induced vibration is significantly reduced. Ausoni also investigated the effect of fully developed cavitation on the vortex shedding frequency of a hydrofoil and found that the vortex shedding frequency may increase by as much as 15 % [31]. De La Torre et. al. also investigated the effect of cavitation on a hydrofoil and concluded that the added mass effect was significantly reduced under super cavitating conditions [32].

Wang et. al. [24] compared the hydrodynamic dampening effect of a Donaldson and a blunt trailing edge. Their findings showed that Donaldson trailing edge significantly increased the hydrodynamic dampening effect. Another important finding was that the dampening increased significantly for flow velocities above resonance between the natural frequency of the hydrofoil and the vortex shedding frequency.

Ducoin et. al. [33] and Münch et. al. [34] investigated the flow behaviour of oscillating hydrofoils. The latter research showed that models could be developed to predict fluid-structure coupling with high precision.

## 2.2.4 The Lock-in Effect

The alternating detachment of vortices from a body expose the body itself to a periodic reaction force. If the frequency of the periodic vortex shedding coincides with the natural frequency of the body producing it, the resonance phenomena might occur. This will lead to increased vibration amplitudes for the body and the vortex shedding [4].

If the body, i.e. a hydraulic turbine blade, is sufficiently flexible, the vortex shedding frequency may be locked-in during resonance. The lock-in phenomena occurs when flow-induced vibration of a structure feeds back on the flow. The interaction between fluid and structure impose a self-reinforcing process which forces the vortex shedding frequency to be constant for a range of velocities. Figure 2.9 illustrates the lock-in phenomena for two differently shaped bodies. The dashed line would illustrate the behaviour of the vortex shedding frequency if the body were infinitely stiff.

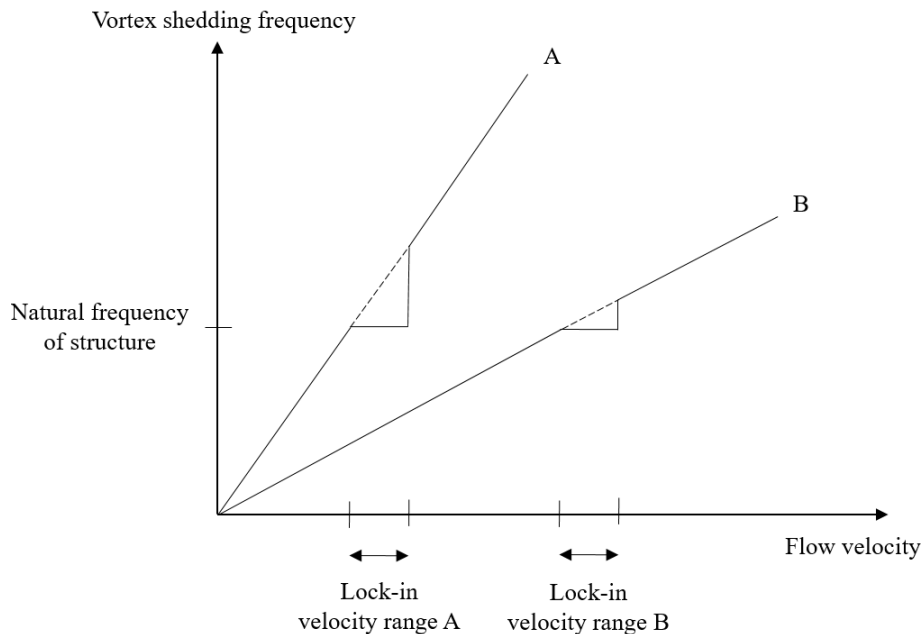


Figure 2.9: The lock-in condition for two different bodies. Body A produces vortices which are shed of at a higher frequency than body B.

A change in the natural frequency of the structure will move the lock-in velocity range. The slope of the linear curve representing the vortex shedding frequency is also determining at what velocities lock-in occur. A change of for example the TE profile of a turbine blade will lead to a new slope of the linear curve. The result is that if the slope of the vortex shedding frequency is increased, the lock-in flow velocity range is moved to higher velocities and Vice Versa, given that the natural frequency is the same. This is what is illustrated in Figure 2.9.

The lock-in flow velocity range is found to be dependent on the vortex shedding amplitude by Bearman [35]. The lock-in velocity range increases with the amplitude of the vortex shedding. The amplitude of the body's vibration is also increasing with an increase in vortex shedding amplitude during the lock-in condition.

## 2.3 Turbulent Boundary Layers

Turbulent boundary layers exert a different behaviour than laminar boundary layers. The shear stress in a turbulent flow is composed of both the viscous stresses and the Reynolds stresses as presented in equation 2.14. The Reynolds stresses are presented more extensively in the next subsection.

$$\tau = \mu \frac{\partial u}{\partial y} + (-\rho \overline{u'v'}) \quad (2.14)$$

To identify the different characteristics of a turbulent boundary layer, the dimensionless wall distance  $y^+$  is used. This parameter depends on the friction velocity, the distance from the wall and the viscosity of the fluid, as presented in equation 2.15.

$$y^+ = \frac{U_f \cdot y}{\nu} \quad (2.15)$$

The friction velocity is defined as a function of the wall shear stress as in equation 2.16.

$$U_f = \sqrt{\frac{\tau_w}{\rho}} = \sqrt{\frac{\mu}{\rho} \cdot \left. \frac{\partial u}{\partial y} \right|_{y=0}} \quad (2.16)$$

The dimensionless wall distance  $y^+$  is used to determine where each of the two terms of the turbulent shear stress dominates. A turbulent boundary layer is divided in a viscous sublayer where the viscous stresses dominate, a buffer layer and at last a logarithmic layer where the Reynolds stresses dominate. The characteristics of the different regions of a turbulent boundary layer will not be further elaborated here but are presented in full detail in the book by Schlichting [13].

### 2.3.1 Turbulence Modelling

A great challenge in the accurate numerical prediction of turbulent flows is how to resolve the formation and nature of the turbulent structures of the flow. To obtain time-accurate solutions for flows experiencing adverse pressure gradients and separation, care has to be taken in the choice of numerical methods.

Numerically, turbulence may be solved down to the smallest turbulent structures of the flow. In this case, the Navier-Stokes equations are solved without any modelling, an approach called Direct Numerical Simulation. This is extremely expensive regarding computational cost, and seldom applicable due to limited time. The usual approach is to model turbulence. The modelling approach is chosen based on the desired accuracy and

the flow behaviour of interest.

One group of turbulence models is the Reynolds-Averaged Navier-Stokes (RANS) models. These models are based on the time-averaged Navier-Stokes equations derived by decomposing the velocity in a time-averaged and a fluctuating part  $u_i = \bar{u}_i + u'_i$ . To further describe these models, the Navier-Stokes and the time-averaged (Reynolds Averaged) Navier-Stokes equations will be presented at first. The Navier-Stokes equation in index notation is presented in equation 2.17 [36].

$$\frac{\partial u_i}{\partial t} + u_j \frac{\partial u_i}{\partial x_j} = g_i + \frac{1}{\rho} \frac{\partial \sigma_{ij}}{\partial x_j} \quad (2.17)$$

where,

$$\sigma_{ij} = -p\delta_{ij} + \mu\left(\frac{\partial u_i}{\partial x_j} + \frac{\partial u_j}{\partial x_i}\right), \quad (2.18)$$

and  $\delta_{ij}$  is the Kronecker delta function.

Now, by applying the continuity equation, the Navier-Stokes equations may be expressed as in equation 2.19.

$$\rho \frac{\partial u_i}{\partial t} + \frac{\partial}{\partial x_j}(\rho u_i u_j) = \rho g_i + \frac{\partial \sigma_{ij}}{\partial x_j} \quad (2.19)$$

To obtain the RANS equation, the quantities are time-averaged, equation 2.21.

$$\rho \frac{\partial \bar{u}_i}{\partial t} + \frac{\partial}{\partial x_j}(\rho \bar{u}_i \bar{u}_j) = \rho \bar{g}_i + \frac{\partial \bar{\sigma}_{ij}}{\partial x_j} \quad (2.20)$$

The second term on the right-hand side may be rewritten,

$$\frac{\partial}{\partial x_j}(\rho \bar{u}_i \bar{u}_j) = \rho \bar{u}_j \frac{\partial \bar{u}_i}{\partial x_j} + \frac{\partial}{\partial x_j}(\rho \overline{u'_i u'_j}), \quad (2.21)$$

and then the Reynolds Averaged Navier-Stokes equation, as presented in equation 2.22, is obtained.

$$\rho \left( \frac{\partial \bar{u}_i}{\partial t} + \bar{u}_j \frac{\partial \bar{u}_i}{\partial x_j} \right) = \rho \bar{g}_i + \frac{\partial}{\partial x_j} (\bar{\sigma}_{ij} - \rho \overline{u'_i u'_j}) \quad (2.22)$$

The term  $-\rho \overline{u'_i u'_j}$  is called the Reynolds stresses and represents a symmetrical second order tensor consisting of six unknown stresses. These stresses in addition to three unknown components of velocity and the unknown pressure make the total number of unknowns ten. There are only four equations for the time-averaged flow, meaning that the equation system is not closed. This is known as the *closure problem of turbulence*. Additional equations are required to solve the problem; this is done through modelling.

## Menters $k - \omega$ Shear Stress Transport model

One group of RANS turbulence models is the two-equation eddy viscosity models which assume that the Reynolds stresses may be represented by the relation presented in equation 2.23 [8].

$$-\overline{\rho u'_i u'_j} = \mu_t \left( \frac{\partial u_i}{\partial x_j} + \frac{\partial u_j}{\partial x_i} \right) - \frac{2}{3} \delta_{ij} (\rho k + \mu_t \frac{\partial u_k}{\partial x_k}) \quad (2.23)$$

The Wilcox  $k - \omega$  model assumes that the eddy viscosity may be represented as in equation 2.24 [37].

$$\mu_t = \rho \frac{k}{\omega} \quad (2.24)$$

The turbulent kinetic energy,  $k$ , and the turbulent frequency,  $\omega$ , is solved for by two transport equations, equation 2.25 and 2.26 respectively.

$$\frac{\partial(\rho k)}{\partial t} + \frac{\partial}{\partial x_j} (\rho u_j k) = \frac{\partial}{\partial x_j} \left( \left( \mu + \frac{\mu_t}{\sigma_k} \right) \frac{\partial k}{\partial x_j} \right) + P_k - \beta' \rho k \omega + P_{kb} \quad (2.25)$$

$$\frac{\partial(\rho \omega)}{\partial t} + \frac{\partial}{\partial x_j} (\rho u_j \omega) = \frac{\partial}{\partial x_j} \left( \left( \mu + \frac{\mu_t}{\sigma_\omega} \right) \frac{\partial \omega}{\partial x_j} \right) + \alpha \frac{\omega}{k} P_k - \beta \rho k \omega^2 + P_{\omega b} \quad (2.26)$$

$\beta'$ ,  $\alpha$ ,  $\beta$ ,  $\sigma_k$  and  $\sigma_\omega$  are all constants, and  $P_{kb}$  and  $P_{\omega b}$  are functions representing the influence of buoyancy forces. The term  $P_k$  is a function representing the turbulence production due to viscous forces.

The original  $k - \omega$  model is highly sensitive to free stream conditions due to the sensitivity of the specified value of  $\omega$  at the inlet [38]. Menter (1994) developed the  $k - \omega$  Shear Stress Transport (SST) model which combines the advantages of the  $k - \omega$  model and another two-equation eddy viscosity model, the  $k - \epsilon$  model [39]. The combination of the  $k - \omega$  and the  $k - \epsilon$  model is done through blending functions. Through the use of the  $k - \epsilon$  model, the model is no longer experiencing the problem of the  $k - \omega$  model in the free stream. The  $k - \omega$  SST model is known for accounting for the transport of turbulent shear stress and provides highly accurate predictions of the onset and amount of flow separation for flow subject to adverse pressure gradients [40].

The mesh is an important factor when it comes to the accuracy of the turbulence models. The theoretically required grid resolution close to walls for the  $k - \omega$  SST model is a  $y^+$ -value of 1. This is recommended to provide an accurate prediction of the flow within the viscous sublayer. However, this wall distance is seldom chosen as it is considered computationally expensive, and it is a complicated operation to design a mesh whereas  $y^+$  is one at all locations on a wall or body. Menter (2009) investigated the accuracy of the  $k - \omega$  SST model by considering Couette flow with  $y^+$  ranging from 0.2 to 100 and found that the computed wall shear stress varied by less than 5 % in this range of  $y^+$  [41].

The  $k - \omega$  SST model will hereafter only be referred to as the SST model.

## Scale-Adaptive Simulation

In transient numerical flow problems, the time-averaged velocities are computed by averaging the velocity over a period of time. This period is for all practical situations set higher than the period in which the smallest structures of the flow forms and breaks down.

The Scale-Adaptive Simulation (SAS) concept is a hybrid between RANS turbulence models and the behaviour of Large Eddy Simulation (LES). The SAS concept is based on the von Karman length scale, which is used to dynamically adjust the model to the resolved structures of the flow. In practice, this means that where the flow is unsteady, the SAS model detects the grid resolved structures, whereas in the steady regions of the flow the RANS model is used.

The SST-SAS model is one of these models. It is based on the SST model, but an additional term is added to the transport equation for the turbulence frequency.

## 2.4 Cavitation

When the pressure of liquids falls below its vapour pressure, the liquid will undergo a sudden phase change [42]. In hydraulic machines, this phenomenon might occur when water flows past bodies with excessive curvature, such as the leading edge (LE) of stay vanes and turbine blades, which force flow separation and the creation of low-pressure zones.

In a fluid flow, the vapour bubbles formed in low-pressure regions may travel to regions of higher pressure. The vapour bubbles will then implode. If this happens at for example a hydraulic turbine blade, it might cause severe damage to the structure. Figure 2.10 shows the erosive effect of cavitation on a turbine blade.

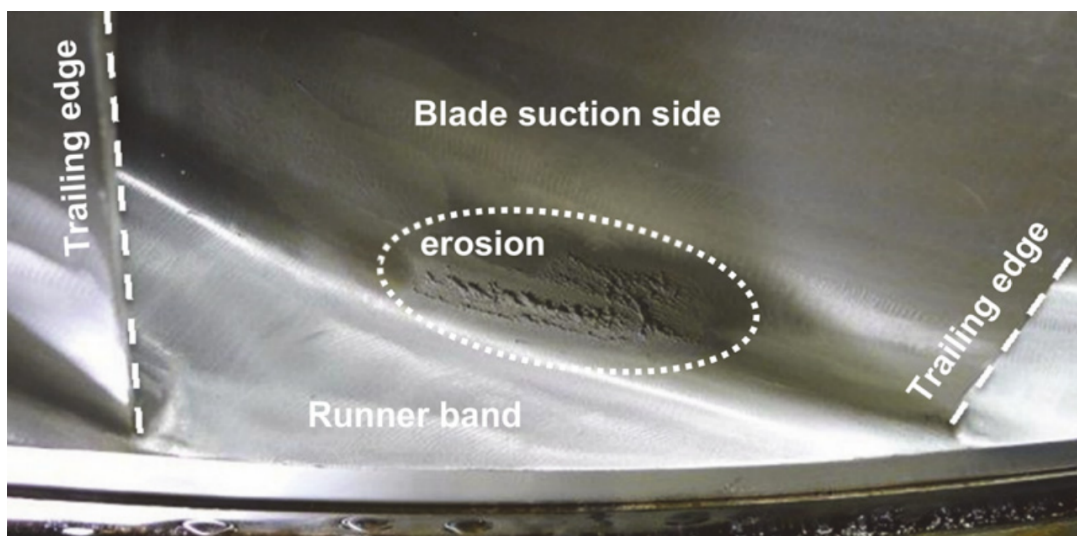


Figure 2.10: Cavitation erosion in a Francis turbine, adapted from [43].

### 2.4.1 Bubble Dynamics

Extensive research has been performed in order to accurately describe and identify the size and dynamics of vapour bubbles formed during cavitation. Rayleigh [44] showed through the momentum equation that the radius of a vapour bubble,  $R_B = R_B(t)$ , may be described by the Rayleigh equation 2.27.

$$R_B \ddot{R}_B + \frac{3}{2}(\dot{R}_B)^2 = \frac{p_B(t) - p_\infty}{\rho} \quad (2.27)$$

However, Rayleigh disregarded the surface tension and viscosity and kept  $p_\infty$  constant. Plesset and Prosperetti [45], developed the Rayleigh equation further to include these effects, the Rayleigh-Plesset equation 2.28.

$$R_B \ddot{R}_B + \frac{3}{2}(\dot{R}_B)^2 = \frac{p_B(t) - p_\infty(t)}{\rho} - \frac{4\nu}{R_B} \dot{R}_B - \frac{2\sigma_B}{\rho R_B} \quad (2.28)$$

In the CFD code Ansys CFX, the Rayleigh-Plesset equation may be used to predict the formation of vapour bubble dynamics. One simplification is made in CFX, which is that the viscous term in equation 2.28 is neglected due to the small magnitude of this term. Bakir [46] found the model used in CFX to show good agreement with experimentally obtained results.



## 3 Methodology

This chapter presents the methodology used to address the objectives of this thesis. At first, the current experimental setup of the cascade test rig will be presented. This is followed by a description of the numerical methods used to design a new hydrofoil where the lock-in condition is present at a lower velocity. At last, the numerical cavitation model used to investigate cavitation in the existing test rig will be described.

### 3.1 The Cascade Test Rig

The cascade test rig, as presented in Figure 3.1, consists of a circular inlet converging into a square test section where the hydrofoil is placed. The outlet section diverges into a circular pipe similar to the one at the inlet. The square test section has inner and outer dimensions 150 mm and 200 mm respectively. The operational range of mean velocities in the square test section is from 0 to 40 m/s, which is based on the available pump at the Waterpower Laboratory. These velocities are computed by the use of continuity and are based on the flow rate and the cross-sectional area of the test section. In the test section, there are several pressure transducers at the walls and two plexiglass windows. The plexiglass windows are present to be able to measure the displacement of the hydrofoil trailing edge by a Laser Doppler Vibrometri (LDV).

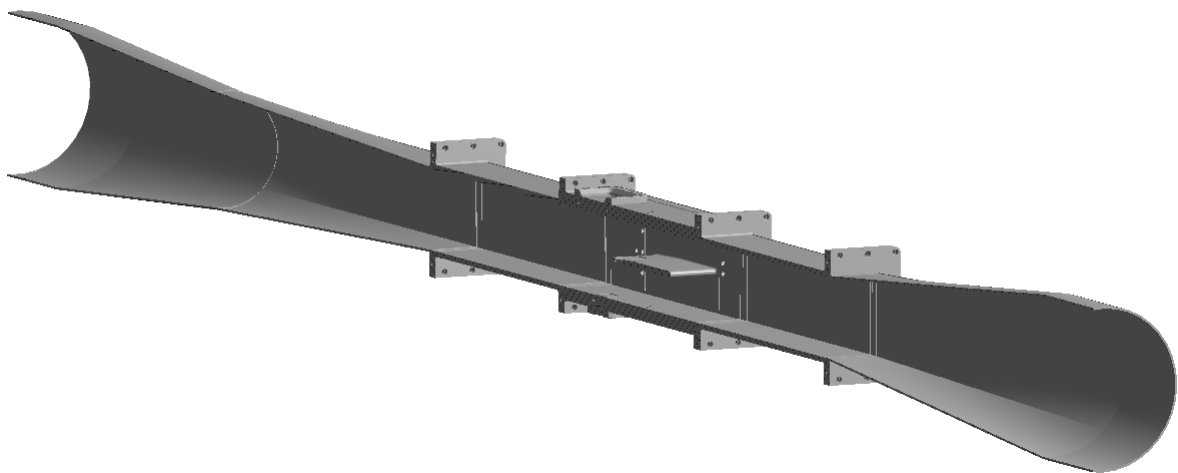


Figure 3.1: Cross-section of the cascade test rig.

The length from LE to TE of the hydrofoil is 250 mm, and it has a thickness of 12 mm at

the thickest section. A chamfer point is located 150 mm from the leading edge, making the thickness at the trailing edge 4.5 mm. The hydrofoil geometry is visualised in Figure 3.2.

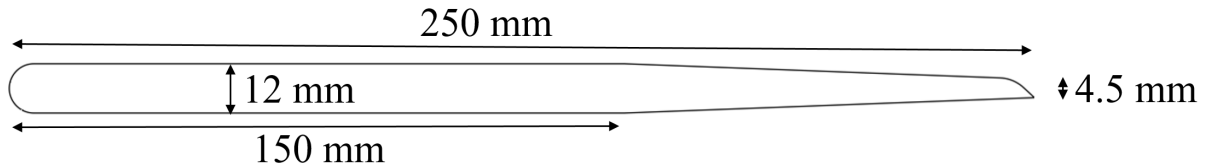


Figure 3.2: The hydrofoil design in the cascade test rig with measures.

The hydrofoil has been milled out of a single aluminium block and consist of two plates connected to the hydrofoil. The transition from hydrofoil to the plates include a fillet. The hydrofoil part is presented in Figure 3.3. At the TE of the hydrofoil, there are depressions for piezoelectric actuators may be seen. There are two actuators, one at the top and one directly beneath the upper one at the bottom of the hydrofoil. These provide forced excitation of the hydrofoil to imitate vibration caused by for example RSI. The actuators may apply forced excitation in a wide range of frequencies, and they also measure receptance. Receptance is the ratio of displacement to the excited force in a vibration [47]. As earlier mentioned, the LDV also measures the displacement.

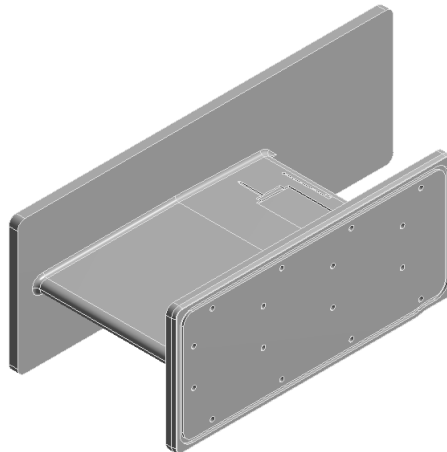


Figure 3.3: The hydrofoil part.

Some material properties of the hydrofoil part are presented in Table 3.1.

Property	Value	Unit
Density	2810	kg/m <sup>3</sup>
Young's modulus	$7.17 \cdot 10^{10}$	Pa
Poisson ratio	0.33	-

Table 3.1: Aluminium alloy, material properties.

During testing the autumn of 2016, the lock-in condition was present at a velocity of around 11 m/s and a frequency of 623 Hz. Figure 3.4 presents the vibration of the hy-

drofoil as a function of velocity measured by the piezoelectric actuators. These results were obtained without forced excitation from the actuators. The experimental results are based on the work by Ting [48].

The pressure sensors located at the wall several places in the cascade test rig did not capture the vortex shedding, unfortunately. The lock-in condition velocity and frequency are therefore the only references for the numerical investigations on the vortex shedding frequency.

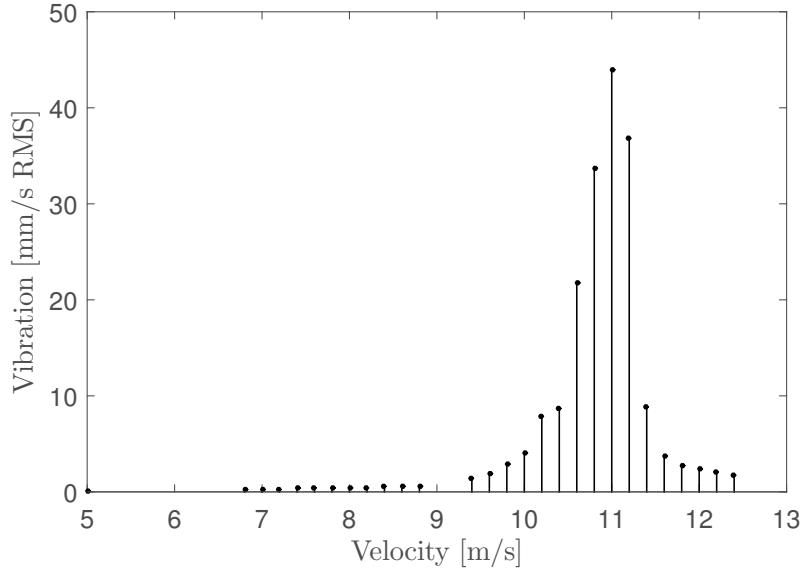


Figure 3.4: Vibration amplitude of hydrofoil as function of velocity for the cascade test rig, adapted from [48].

## 3.2 Numerical Fluid Flow Investigations

The numerical fluid dynamics tool Ansys CFX is used for all fluid flow investigations in this thesis. Ansys CFX is based on a finite volume formulation of the Navier-Stokes equations. CFX is chosen due to great in-house knowledge at the Waterpower Laboratory.

The goal of the numerical fluid flow investigations is to design a new hydrofoil whereas vortices are shed off at a higher frequency than for the original hydrofoil and to identify and investigate cavitation in the current test rig. The former will be addressed at first.

### 3.2.1 Design Strategy

Credible numerical prediction of vortex shedding frequencies may be expensive regarding computational cost. The design strategy is therefore carefully considered in the design of a new hydrofoil.

As described in chapter 2.2.3, the vortex shedding frequency is dependent on the TE profile. Different TE profiles are therefore tested and compared to the original design. In order to reduce the computational cost of the TE investigations, the design process is divided into two steps:

1. Isolated trailing edge profile investigations with initial numerical model
2. Final design investigations on proposed trailing edge with validated numerical model

The first step consists of testing constant thickness hydrofoils with different TEs. Constant thickness is chosen in order to isolate the effect of the TE. The thickness and length are set to 12 mm and 250 mm respectively. The length is the same as for the original hydrofoil, and the thickness is the same as at the thickest point of the original hydrofoil. The original TE and two other designs will be compared. These are visualised in Figure 3.5, and are similar to the TE designs d (**a**), f (**b**) and h (**c**) presented in Figure 2.8. The TE in the existing cascade test rig is the same as design d in Figure 2.8 and **a** in Figure 3.5. The TEs of hydrofoil **a** and **b** are rounded off by 2 and 4 times the thickness respectively. The TE of hydrofoil **c** is rounded off such that the thickness of 12 mm is achieved at a distance 1.2 times the thickness from the TE.



Figure 3.5: Trailing edge designs with constant thickness hydrofoils.

Design **a** is chosen to act as a reference for design **b** and **c**. Design **b** is the preferred design in terms of increasing the vortex shedding frequency, based on the work by Heststad and Olberts [21]. Regarding the symmetrical design **c**, this is chosen because Brekke [23] did not present the relative vortex shedding frequency of this TE, and it is not found investigated with this rounding in any other studies either. The symmetrical trailing edge **m** presented in Figure 2.8, with a 30-degree angle is assumed to produce a higher vortex shedding frequency than design **c**, but as the sharp edge is hard to achieve during manufacturing, this TE is not considered in these studies.

Several CFD simulations will be required to propose a final design for the hydrofoil. In order to achieve a verified and converged numerical model with respect to the number of nodal points, time step and turbulence model, a 2D numerical mesh is chosen over a 3D mesh. A 3D converged mesh is expected to increase the number of nodal points and

thereby the simulation time significantly.

The 2D mesh used to test the constant thickness hydrofoils will be based on an independent mesh developed for the original hydrofoil design. As a converged mesh is developed, the hydrofoils will be tested at flow velocities ranging from 0 to 40 m/s with intervals of 5 m/s. The tests will be performed in the following order:

1. Original hydrofoil design
2. Hydrofoil **a**
3. Hydrofoil **b**
4. Hydrofoil **c**

If the results from the constant hydrofoil tests reveal that the shedding frequency will be lower than any of the other constant hydrofoil designs, the tests will not be run in the entire flow velocity range. The results from the constant thickness hydrofoil simulations is presented later in this chapter.

Based on the results obtained from the constant hydrofoil tests, the best alternative, i.e. the TE providing the highest vortex shedding frequency, will be further investigated and compared to the original design. However, before any further numerical simulations are done, a  $y_{avg}^+$  and time step sensitivity analysis will be performed in order to reveal possible weaknesses in the initial numerical setup. The effect of using the SST-SAS turbulence model will also be investigated.

As an adequate numerical model is established the first consideration is to investigate the vortex shedding frequency of a hydrofoil with the proposed TE and similar chamfer as the original hydrofoil. Other possible design changes, for example, reducing the natural frequency by moving the chamfer point, may also be investigated based on the results and the expected lock-in range of the new design.

The whole design process is illustrated in the flow chart shown in Figure 3.6.

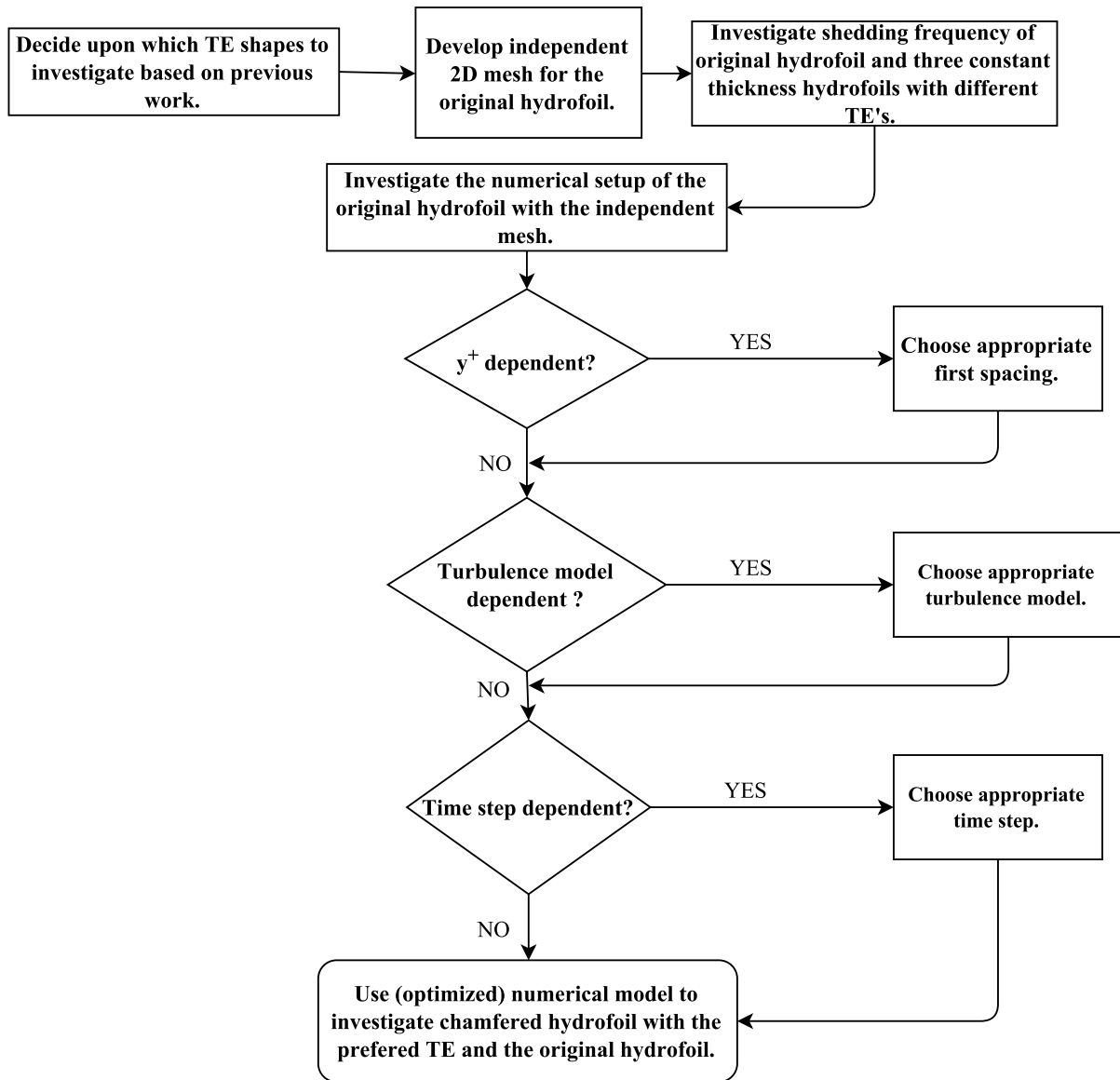


Figure 3.6: Work flow design strategy.

### 3.2.2 Computational Domain

The 2D computational domain of the cascade test rig is extended, compared to Figure 3.1, upstream and downstream of the hydrofoil to ensure proper boundary layer development. The upstream and downstream section will be extended by 5 meters each. The result is a computational domain being 26.81 hydrofoil lengths upstream the LE of the hydrofoil and 29.69 hydrofoil lengths downstream the TE of the hydrofoil. A similar setup and velocity range has proved this to be sufficient [49].

All parts of a 2D cross section of the cascade test rig in contact with water, and filled with water, will be part of the computational domain. One simplification is made in the domain, which is that the fillets connecting the hydrofoil to the plates on each side of the aluminium hydrofoil part are removed. This is due to the chosen 2D numerical domain.

The effect of this simplification is that it will increase the cross-sectional area on top and bottom of the hydrofoil, which will lead to a small decrease in the flow velocity in this area of the domain.

The Computer Aided Design (CAD) software SpaceClaim is used to design the constant thickness hydrofoils with varying trailing edges. The full geometrical model of the existing cascade test rig has already been made by PhD Candidate Carl Werdelin Bergan at the Waterpower Laboratory.

### 3.2.3 Numerical Setup

All fluid flow analyses, including the mesh independence study, are transient. For the convergence study and the constant hydrofoil tests, the time step and total time are set to  $2.5 \cdot 10^{-4}$  and 2 seconds respectively. The time step corresponds to a frequency of 4000 Hz. Based on the experimental observations, that the lock-in condition was present at a velocity of 11 m/s and a frequency of 623 Hz, the time step is expected to be sufficient. The turbulence model is set to SST with first order numerics. The SST model is chosen as it provides high accuracy of the investigated flow phenomena at a relatively low computational cost. These and other important parameters for these studies are presented in Table 3.2. As described earlier, the time step and the turbulence model may be changed before final tests are run with the proposed TE.

<b>Property</b>	<b>Setting</b>
Analysis type	Transient & Incompressible
Double precision	Yes
Total time	2 s
Time step	$2.5 \cdot 10^{-4}$ s
Turbulence model	SST
Turbulence numerics	First order
Advection scheme	High resolution
Transient scheme	Second Order Backward Euler
Convergence criteria	1e-5 RMS
Maximum number of Coefficient Loops	5
Minimum number of Coefficient Loops	1

Table 3.2: Numerical settings for the mesh independence test and constant thickness hydrofoil investigations.

The boundary conditions used at the inlet and outlet is a mass flow rate and an average static pressure respectively. The left and right sides of the 2D domain are given the symmetry boundary condition. The upper and lower wall are given the no-slip wall condition. The inlet mass flow is varied from 0 to 900 kg/s for the constant hydrofoil tests. This corresponds to velocities ranging from 0 to 40 m/s in the square test section with inner dimension 150 mm. The simulations are performed at intervals of 5 m/s. The average static pressure at the outlet is set to 0 Pa, and the reference pressure is set to 1 atm. The latter will lead to negative pressure in some parts of the domain due to the

incompressible solver setting. The negative pressure level is not affecting the solution in any other way than that it will compute a negative pressure some places in the domain. Later on, when cavitation is investigated the pressure levels will be adjusted such that the formation of water vapour is correctly identified.

### 3.2.4 Mesh Quality and Convergence

The software ICEM CFD is used to generate the fluid mesh. This software allows the user to create a mesh which only consists of hexahedral elements. This is beneficial in terms of reducing the number of nodal points and achieving good orthogonal angles [50].

As mentioned previously, the mesh used in the first design step is developed by investigating the original hydrofoil design. The independence test will be performed at the maximum flow velocity of 40 m/s, an average  $y^+$ -value of about 20 at the hydrofoil surface and with the SST turbulence model. This will not provide sufficiently low  $y_{avg}^+$ -values for the higher flow velocities, but as it will be expensive to run a "perfect" mesh for all velocities, this is not done in the initial design stage. The maximum velocity is chosen as this is the velocity where the most chaotic turbulent flow is expected to occur.

The mesh independence study is performed by increasing the number of nodal points at every edge of the fluid domain until satisfactory convergence is reached. Convergence is investigated by considering the absolute pressure at four different points close to the hydrofoil surface; one at the leading edge (P26), one at the thickest point (P19), one at the trailing edge (P28) and one point located one hydrofoil length downstream the trailing edge (P323). These monitoring points and several other monitor points are visualised in Figure 3.7. The reason for using this amount of monitor points is that the solution in the whole fluid domain is not saved for all time steps. That would quickly fill up the hard drive of the computer. Instead of saving the solution in the whole domain at all time steps, the solution is only saved at certain monitor points.

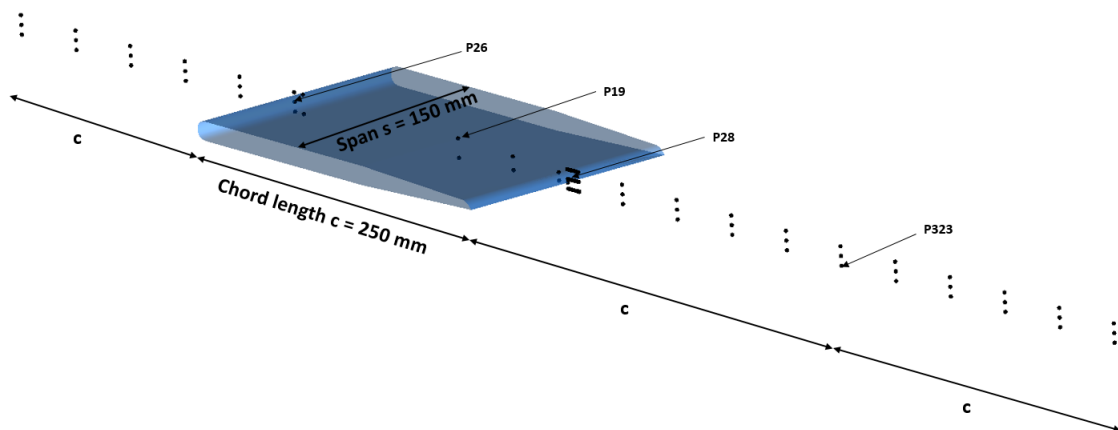


Figure 3.7: Monitor points in the fluid domain.



The first mesh size to be investigated in the mesh independence study is 136 180 nodal points. The first spacing at the hydrofoil surface is  $1.45 \cdot 10^{-5}$  m and  $y_{avg}^+ = 17$  at a velocity of 40 m/s. The mesh sizes used in the mesh independence study is 555 024, 2 240 824, 4 654 008 and 9 004 872 nodal points. Figure 3.8 shows the blocking strategy together with the mesh with 2 240 824 nodal points, which, based on the results from the mesh independence study, is used for further studies.

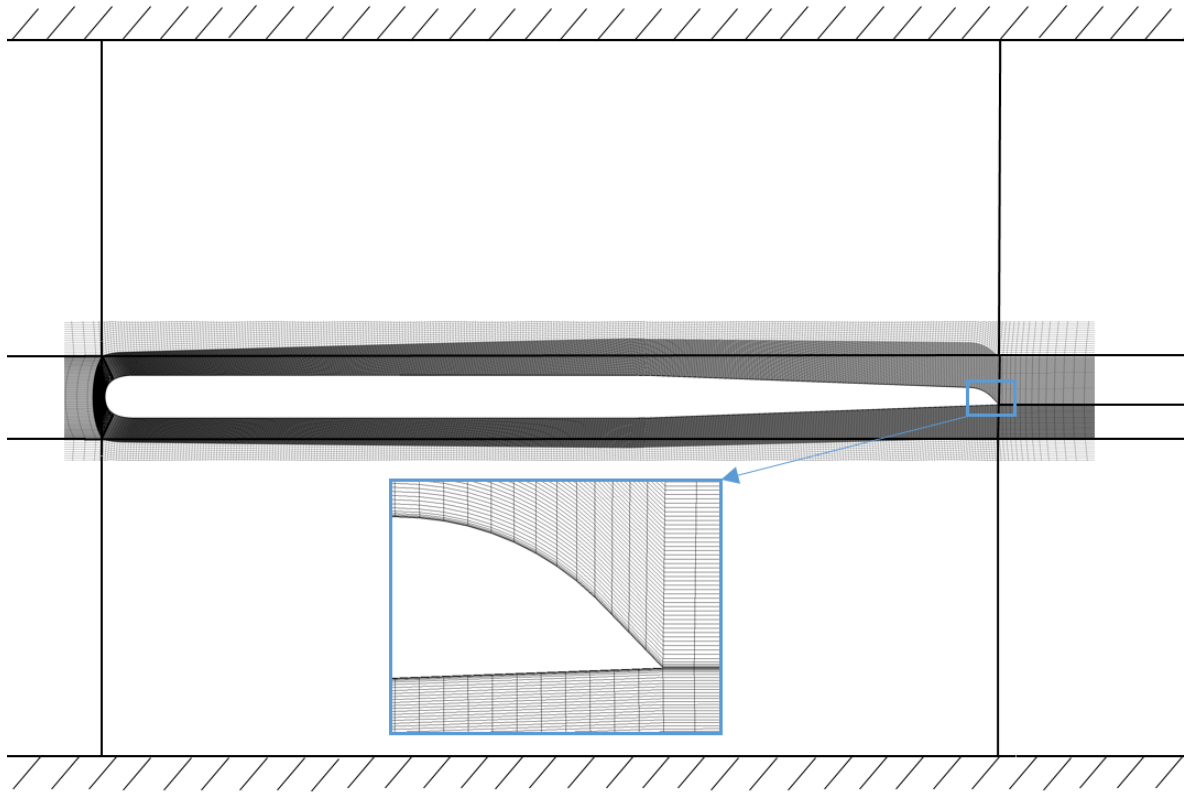


Figure 3.8: Final 2D mesh and blocking.

Figure 3.9 presents the result from the mesh independence study. All parameters are not fully converged with a mesh size of 2.2 million cells. However, this mesh is chosen for further studies in order to reduce computational cost. What is apparent is that all pressures are converging towards a certain level. The mesh size sensitivity is seen to be higher at the LE and TE than at the thickest point and downstream the hydrofoil. Another observation is that the pressure level at all points except at the LE is negative. As the solver is set to incompressible, this is not affecting the numerical solution, but it is noted for further studies where cavitation is investigated.

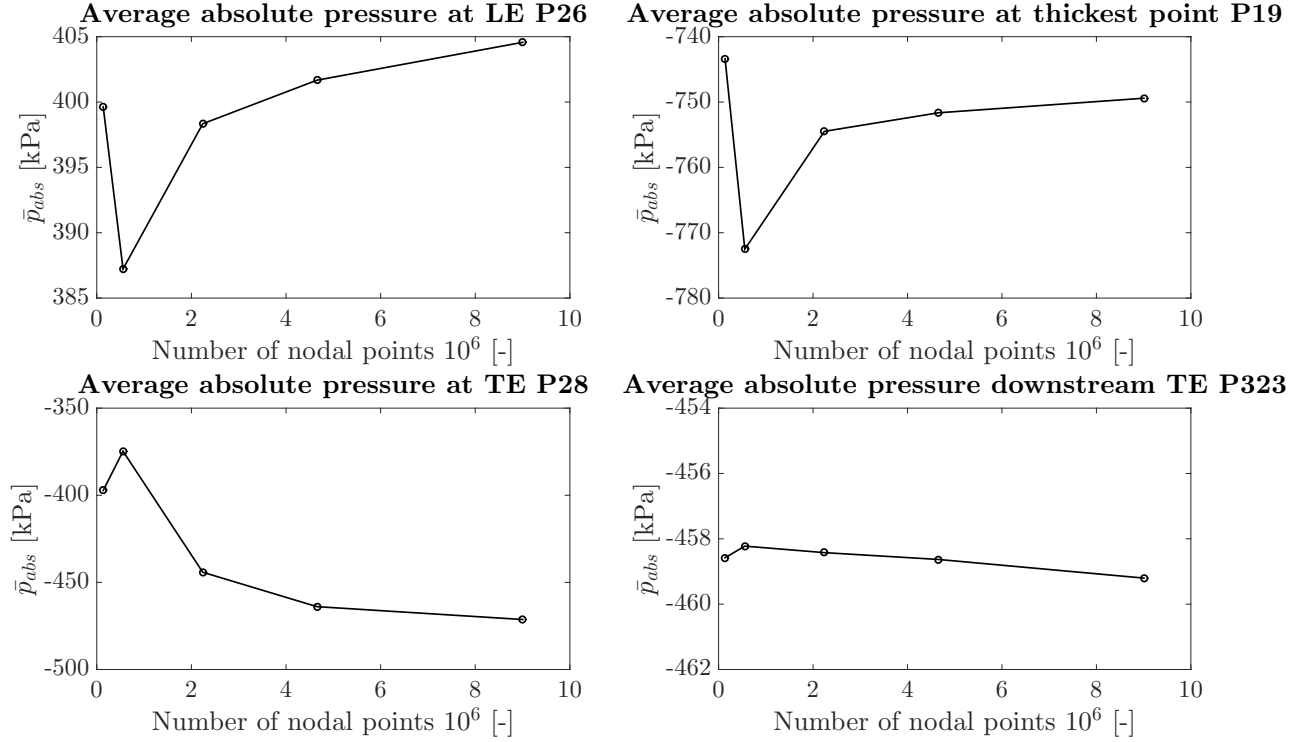


Figure 3.9: Results mesh convergence study.

Table 3.3 presents the mesh statistics and quality measures of the mesh chosen for further studies. The acceptable range of the aspect ratio, expansion factor and orthogonal angle are given in parentheses and comes from the Ansys CFX help manual [51]. The acceptable range must be regarded as a recommended range, as the CFX solver accepts that the quality parameters are outside this range. The cells with large aspect ratios are not considered to affect the mesh badly as they are elongated in the streamwise direction. A description of the mesh quality parameters is given in [52].

Statistics and quality parameter	Value	Within acceptable range [%]
Million nodes	2.24	
First node [m]	$1.45 \cdot 10^{-5}$	
Element increment ratio	1.5	
$y_{avg}^+$ at 40 m/s	17	
Minimum quality	0.697	
Minimum equiangle skewness	0.491	
Aspect ratio (<1000*)	105 - $3.91 \cdot 10^4$	51.51
Mesh expansion factor (<20)	1 - 114	99.99
Minimum orthogonal angle (> 20)	44.19	100

Table 3.3: Mesh statistics and quality measures.

\*Acceptable range when running double precision.

The mesh developed for the original hydrofoil, is used for all hydrofoils despite the geometrical changes. This is done to reduce the time consumption and is achieved by

changing how the edges of the blocks are associated with the geometry. The edges of the blocks are associated to the curves of the geometry. As the geometry is changed, the associations are changed to be connected to the curves of the new geometry (other hydrofoils).

### 3.2.5 Data Analysis

To analyse the results obtained in the CFD analyses, both CFX post and Matlab is used. CFX-post gives the opportunity to visualise the pressure and velocity contours of the flow around the hydrofoil, and to identify vortices through the  $\lambda_2$ -criterion.

Matlab's Fast Fourier Transform (FFT) function *fft* is used to identify the vortex shedding frequency [53]. The analysed signal is the absolute pressure signal subtracted its average and normalised with respect to the maximum amplitude. The results from the FFT analyses is visualised by black-white color intensity plots which provide easy comparison of several results at the same time. Note that when speaking of the absolute pressure signal in the label of the color bars in the FFT intensity plots (*Normalized absolute pressure signal at P210 [-]*), this refers to the absolute pressure signal subtracted its average.

The point P210 is the chosen monitor point to analyse the vortex shedding frequency at. The flow at this point experiences large velocity gradients and is placed close to the wake of the hydrofoil TE. Figure 3.10 shows the velocity contour of the original hydrofoil at a velocity of 10 m/s obtained with the initial numerical setup. The transparent figure laid on top is a visualisation of the monitor points close to the TE.

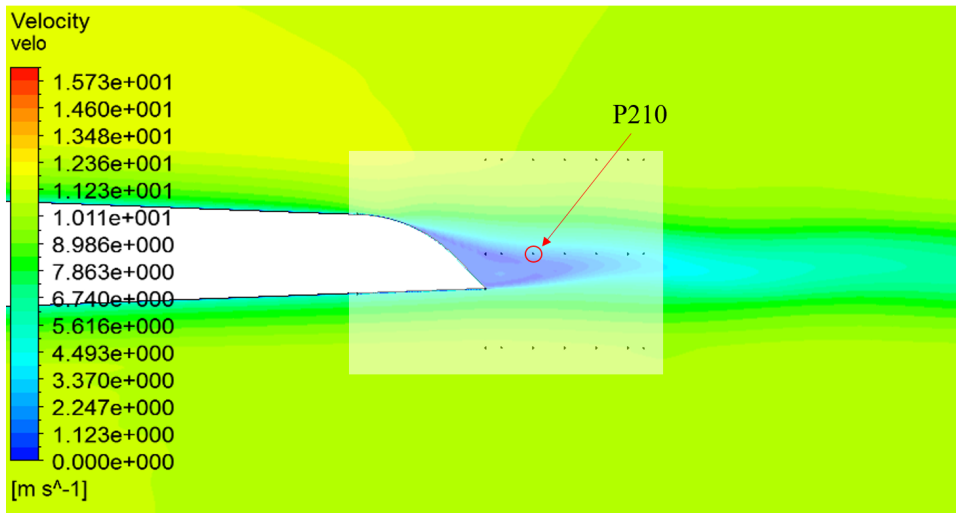


Figure 3.10: Velocity contour of original hydrofoil at 10 m/s together with chosen monitor point for analysis of vortex shedding frequency.

The size of the wake is different for the constant thickness hydrofoils and at other flow velocities. However, the point P210 is in a region where the flow is expected to be

unstable due to periodic detachment of vortices for all hydrofoil designs. The point P210 is therefore used for all vortex shedding frequency analyses.

### 3.2.6 Results Design Step 1

The results from the constant thickness hydrofoil study are presented here as they influenced the final numerical setup. Figure 3.11 presents the vortex shedding frequencies obtained from investigation of the different constant thickness hydrofoils and the original hydrofoil. The results are compared to equation 2.12 presented in the previous chapter. The Strouhal number is set to 0.19 as suggested by Gongwer, and the geometrical factor B for hydrofoil c is adapted from Antonsen [22] and set equal to 96.

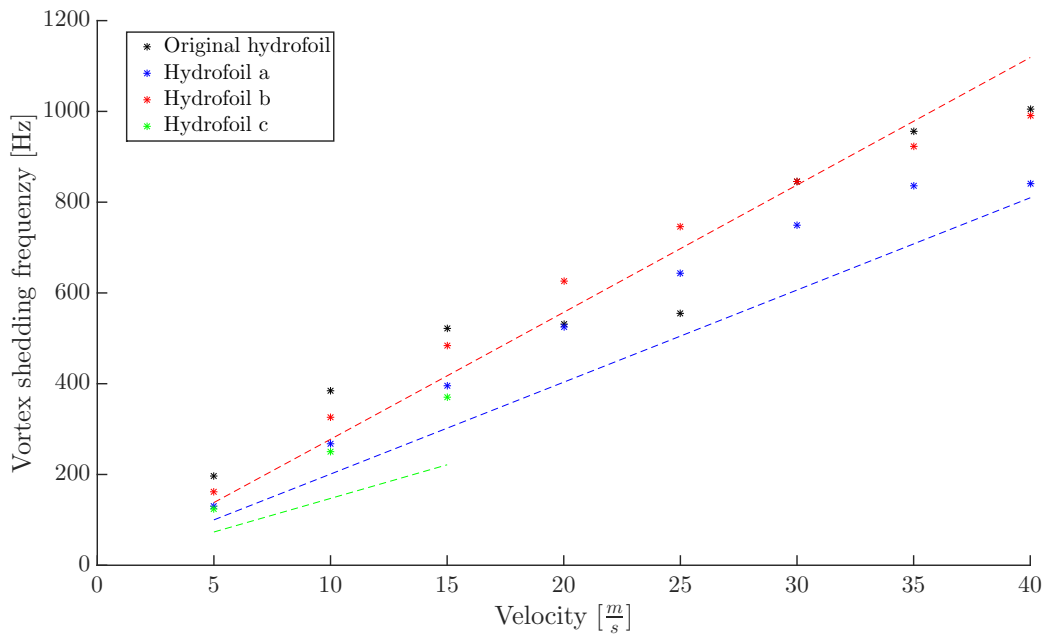


Figure 3.11: Results constant thickness hydrofoil study with comparison to equation 2.12 with a Strouhal number of 0.19. Dashed line represents the result from the empirical formula 2.12.

The results presented in Figure 3.11 are based on the FFT intensity plots shown in Figures 3.12, 3.13, 3.14 and 3.15. The figures represent the FFT of all investigated flow velocities and hydrofoils. In Figure 3.11, the dominant frequencies in these FFT plots are used. Where the dominant frequency is not the expected, based on a linear relation between vortex shedding frequency and velocity, the expected real frequency is represented in the figure.

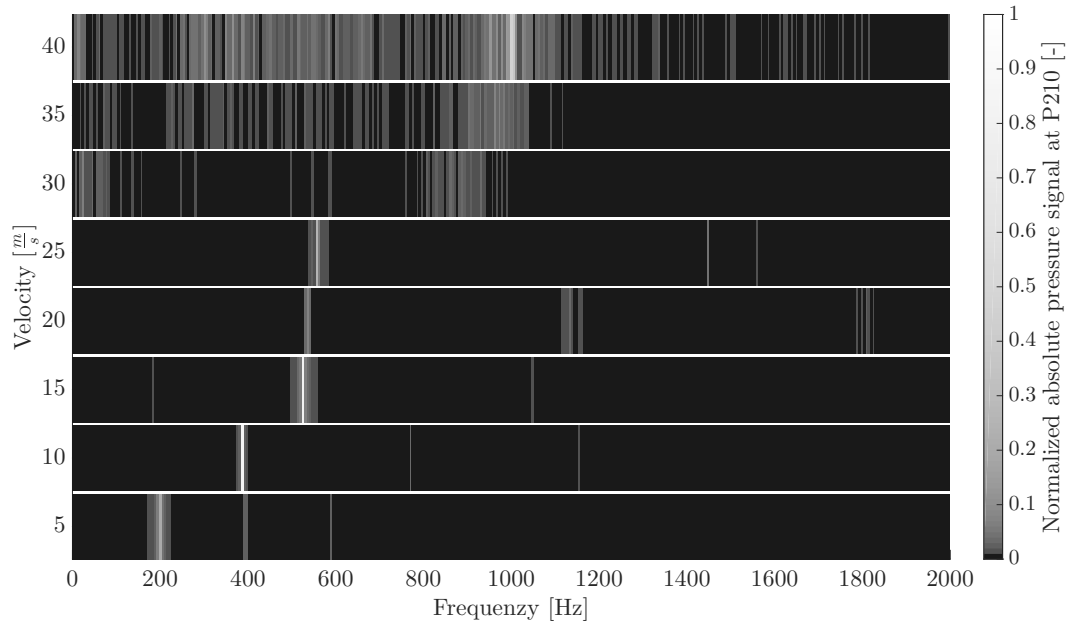


Figure 3.12: Intensity plot of FFT for original hydrofoil at velocities ranging from 0 to 40 m/s.

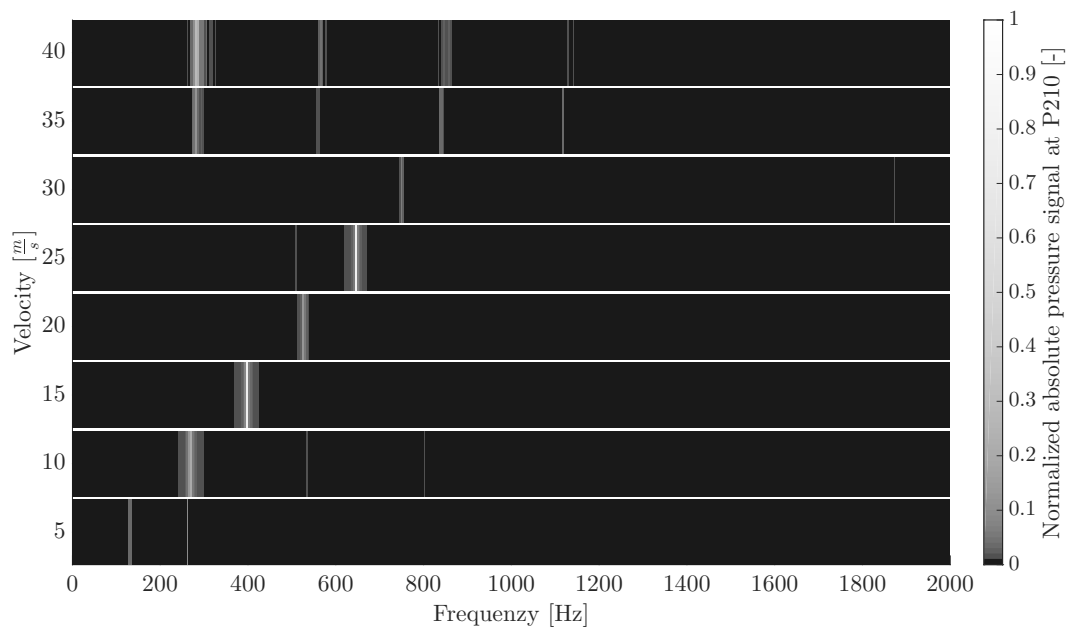


Figure 3.13: Intensity plot of FFT for hydrofoil **a** at velocities ranging from 0 to 40 m/s.

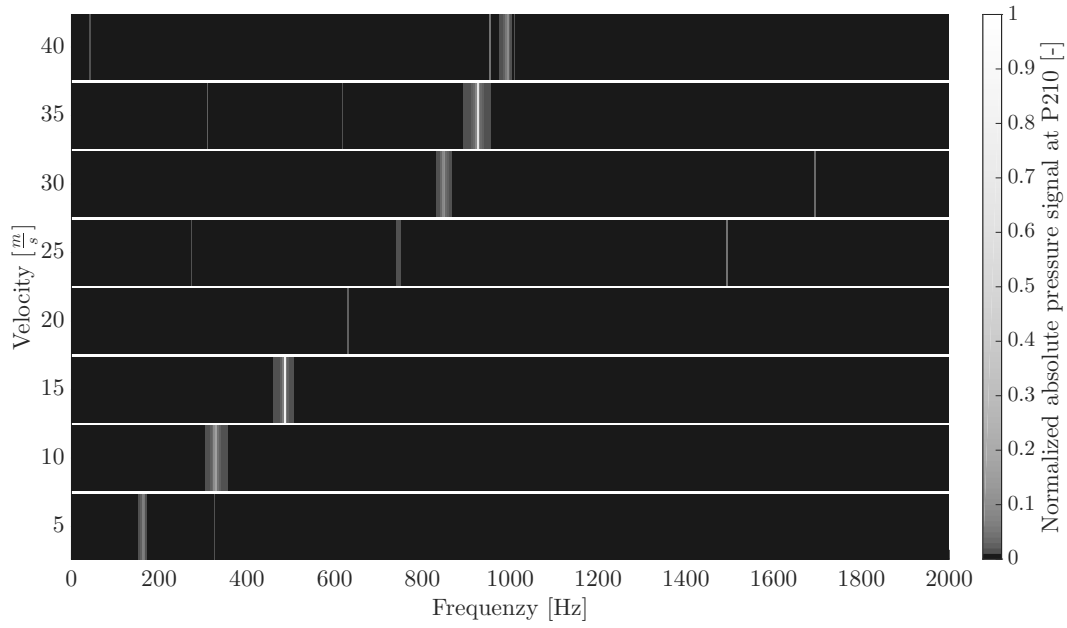


Figure 3.14: Intensity plot of FFT for hydrofoil **b** at velocities ranging from 0 to 40 m/s.

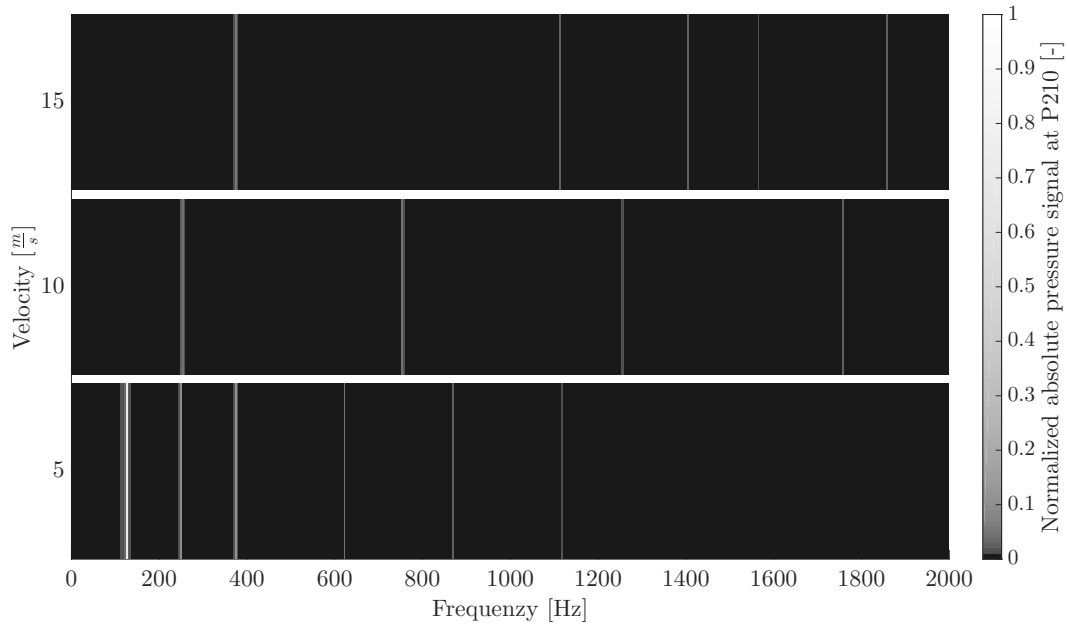


Figure 3.15: Intensity plot of FFT for hydrofoil **c** at velocities ranging from 0 to 40 m/s

All tested hydrofoils have vortex shedding frequencies higher than suggested by equation 2.12 for nearly all flow velocities. However, the vortex shedding frequency does not follow a fully linear pattern, and as mentioned previously, some of the FFT plots reveal that the dominant frequency is lower than expected. The following results are not expected based on empirical and theoretical relations presented in the previous chapter:

- The original hydrofoil has a nearly constant vortex shedding frequency in the range 15-25 m/s
- The FFT plot of hydrofoil **a** shows frequencies that are lower than the expected at 25, 35 and 40 m/s
- The FFT plot of hydrofoil **b** shows frequencies that are lower than the expected at 25, 35 and 40 m/s
- The slope of all frequency vs. velocity curves are decreasing as the velocity is increasing.

The average  $y^+$ -value at the hydrofoil surface is increasing for an increasing flow velocity, which is believed to affect the results. The average  $y^+$ -value at the hydrofoil surface for all flow velocities for the original hydrofoil are presented in Table 3.4.

Velocity [ $\frac{m}{s}$ ]	$y_{avg}^+$ [-]
5	2.50
10	4.68
15	6.79
20	8.84
25	10.85
30	12.82
35	14.76
40	16.90

Table 3.4: Average  $y^+$ -value at the hydrofoil surface for original hydrofoil with initial numerical setup.

### 3.2.7 Final Numerical Model

Based on the results presented in Figure 3.11, the trailing edge design of hydrofoil **b** is used for further studies.

However, before any more design considerations are made, the mesh is adjusted, and the turbulence model and time step are changed. The changes are made in that order, and the following subsections justify these changes.

#### Mesh adjustment

The mesh is adjusted in a way that ensures that the  $y_{avg}^+ \approx 1$  for flow rates up to 20 m/s. This was achieved by changing the first spacing at the hydrofoil surface from  $1.45 \cdot 10^{-5}$  m to  $1.8 \cdot 10^{-6}$  m.

As the mesh is slightly changed, the mesh independence test is in practice no longer valid. Hence, the new mesh is compared to the old at the same monitor points as investigated in the mesh independence study with the original hydrofoil design. The comparison is done at flow velocities 10, 15 and 20 m/s. Table 3.5 summarises the comparison of the

solutions obtained with the two different meshes. The vortex shedding frequency and the average  $y^+$ -value at the hydrofoil surface is also included for the six different cases.

The deviation from the converged and the new mesh seem to increase with increasing difference in  $y^+$ . The points P19 and P28, being at the thickest point and at the hydrofoil TE, show the largest deviation. These points are placed where the flow is heavily influenced by boundary layer effects. By increasing the resolution of the mesh (decreasing  $y^+$ ), the boundary layer is better resolved, which may explain the reason that the biggest deviation is found here.

$V \left[\frac{m}{s}\right]$	Point	Old mesh			New mesh			Comparison
		$\bar{p}_{abs \ old}$ [kPa]	$f_s$ [Hz]	$y_{avg}^+$	$\bar{p}_{abs \ new}$ [kPa]	$f_s$ [Hz]	$y_{avg}^+$	$1 - \frac{\bar{p}_{abs \ new}}{\bar{p}_{abs \ old}}$ [%]
10	P26	122.019	383.7	4.68	122.077	388.2	0.58	-0.048
	P19	50.924			51.065			-0.28
	P28	64.102			63.413			1.07
	P323	66.866			66.772			0.14
15	P26	146.469	522.3	6.79	146.632	540.9	0.84	-0.11
	P19	-14.083			-13.287			5.65
	P28	19.363			17.145			11.45
	P323	23.405			23.183			0.95
20	P26	179.773	531.6	8.84	180.262	639.4	1.08	-0.27
	P19	-106.563			-104.320			2.10
	P28	-41.572			-47.149			-13.41
	P323	-37.644			-38.069			-1.13

Table 3.5: Mesh comparison after change of first spacing.

The FFT representing the vortex shedding frequencies presented in the table are not included here, but what is seen is that the vortex shedding frequency is significantly higher for the new mesh at 20 m/s than for the old mesh. From this, one can conclude that  $y^+$  heavily influence the vortex shedding frequency. The new mesh does no longer exert the constant behaviour for flow velocities in the range 15 to 25 m/s. The new mesh is therefore used for all the following studies, despite slight deviation in the average absolute pressure some places in the domain.

Table 3.6 presents the mesh statistics and quality measures of the new mesh with the acceptable ranges in parentheses for the aspect ratio, expansion factor and the orthogonal angle. The new mesh at regions close to the TE is presented in Figure 3.16.



Statistics and quality parameter	Value	Within acceptable range [%]
Million nodes	2.24	
First node [m]	$1.8 \cdot 10^{-6}$	
Element increment ratio	1.5	
$y_{avg}^+$ at 20 m/s	1.08	
Minimum quality	0.697	
Minimum equiangle skewness	0.491	
Aspect ratio (<1000*)	$35.5 - 3.16 \cdot 10^5$	32.88
Mesh expansion factor (<20)	1 - 167	99.99
Minimum orthogonal angle (> 20)	44.19	100

Table 3.6: Mesh statistics and quality measures new mesh.

\*Acceptable range when running double precision.

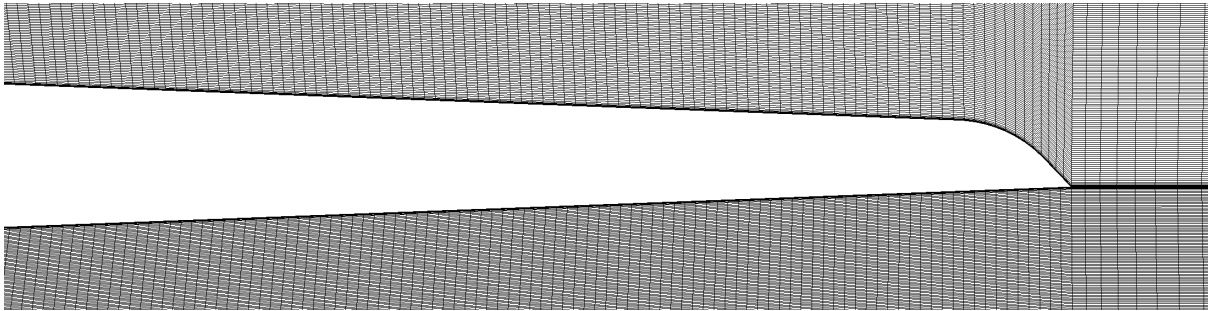


Figure 3.16: New mesh at trailing edge.

### Turbulence model dependence

The results from the turbulence model test with SST and SST-SAS is presented in Figure 3.17. The comparison was done with the new mesh at velocities 10, 15 and 20 m/s. The linear fitting line of the results is also included.

What is evident is that using the SST-SAS model does not significantly affect the vortex shedding frequency. However, the linear fitting line of the SST-SAS turbulence model exerts behaviour that is closer to the physically expected. First of all, so far the shedding frequency of the original hydrofoil has been lower than expected, as the experimental results showed that the lock-in condition was present at 623 Hz. The SST-SAS turbulence model has a slightly greater slope than the SST model which is more in accordance with the experimental results. The cross-over point at the y-axis, which should have been zero at zero velocity, is also closer to zero for the SST-SAS model.

The simulation time of the SST-SAS model is not significantly higher than for the SST model, and it is therefore used for all future studies despite the small and less significant change of physical behaviour.

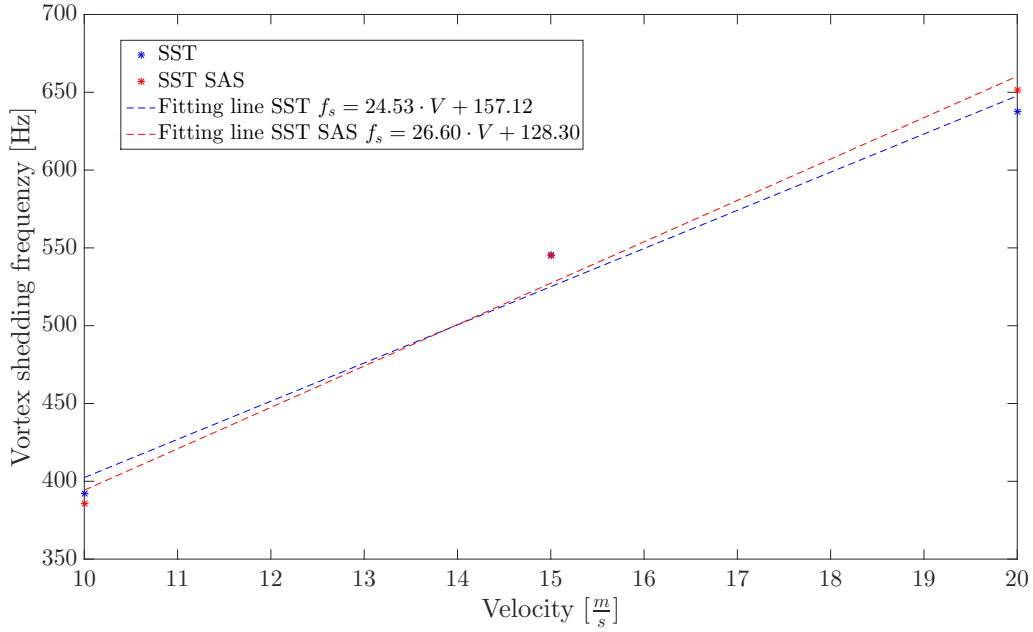


Figure 3.17: Results turbulence model test with fitting line.

### Time step dependence test

With the new mesh and the SST-SAS turbulence model, a time step dependency analysis is performed on the original hydrofoil at 10 m/s. An analysis with respect to vortex shedding frequency and amplitude is carried out to investigate the convergence of these parameters with respect to time step. Figure 3.18 shows the result from this test. As can be seen, both the vortex shedding frequency and the amplitude is converging with decreasing time step.

The chosen time step for further studies is the time step which is a quarter of the original time step. Accordingly, the new time step is  $6.25 \cdot 10^{-5}$ . Even though the frequency nor the amplitude is fully converged at this time step, the computational cost of decreasing the time step further is considered too expensive.

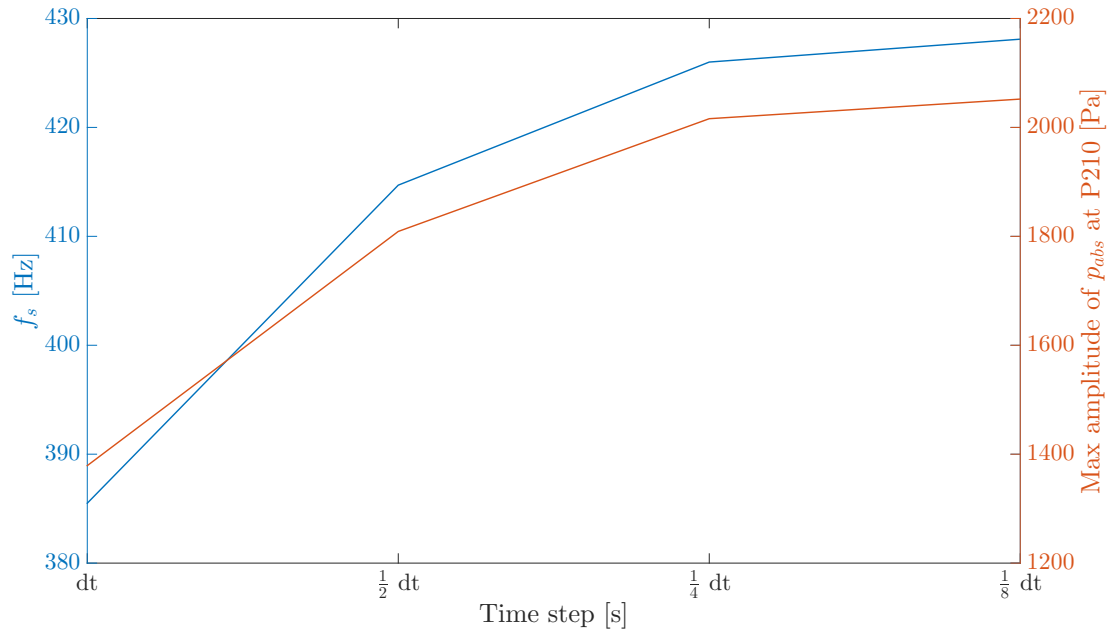


Figure 3.18: Results time step dependence test.

Figure 3.19 presents the Fast Fourier Transform intensity plot used to determine the dominant frequency of the absolute pressure signals.

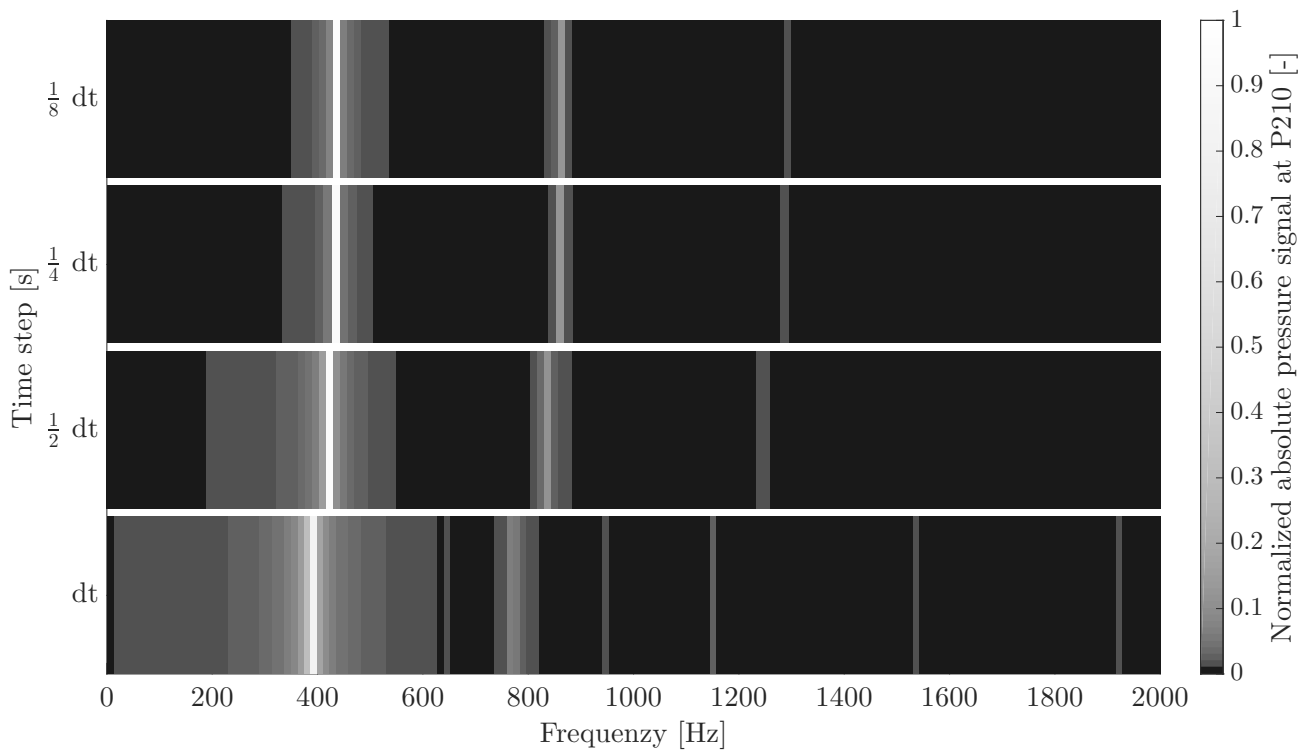


Figure 3.19: FFT of absolute pressure at monitor point P210 for original hydrofoil at 10 m/s with varying time steps.

## Final numerical setup

Table 3.7 presents the final numerical settings used for all further studies. The original hydrofoil and a chamfered hydrofoil with the new proposed trailing edge with a 30-degree angle will be tested at 5, 10 and 15 m/s with these numerical settings. The hydrofoil is visualised in Figure 3.20. Further adjustments to the hydrofoil may be done, based on the results obtained in the analyses.

Property	Setting
Analysis type	Transient & Incompressible
Double precision	Yes
Total time	2 s
Time step	$6.25 \cdot 10^{-5}$ s
Turbulence model	SST-SAS
Turbulence numerics	First order
Advection scheme	High resolution
Transient scheme	Second Order Backward Euler
Convergence criteria	1e-5 RMS
Maximum number of Coefficient Loops	5
Minimum number of Coefficient Loops	1

Table 3.7: Final numerical settings.



Figure 3.20: Hydrofoil with chamfer and proposed TE.

### 3.2.8 Cavitation Modelling

In the cascade test rig, the maximum gage pressure in the pressure tank which pressurises the system is 10 bar. Cavitation was experienced at a flow velocity of approximately 27 m/s in the test rig. At this flow velocity, the maximum pressure was reached, and an increased pressure would be needed to avoid cavitation at this flow velocity.

To further investigate the formation of water vapour bubbles in the test rig, a test was performed at lower flow velocities, 13-14 m/s, with a gage pressure of 1 bar only in the pressure tank. The low pressure forced the flow to cavitate at a much lower flow velocity. Cavitation was filmed with a high-speed camera by PostDoc Bjørn Winther Solemslie at the Waterpower Laboratory. Figure 3.21 show the cavitation close to the hydrofoil trailing edge at the flow velocities 13.0, 13.5 and 14.0 m/s. These pictures are taken from the video produced by the high-speed camera. The video was taken through the small plexiglass window on top of the hydrofoil test section, which can be seen in Figure 3.1. At 13.0 m/s small clouds of cavitation is seen, which indicates that the onset of cavitation lies around this flow velocity and pressure. At 13.5 m/s, a small vapour cloud is seen at the upper side of the hydrofoil. As the plexiglass window does not show more than what

is visualised in the figure, the area where the cavitation originates is not visible. At 14.0 m/s the film has turned into a water vapour cloud with a chaotic behaviour.

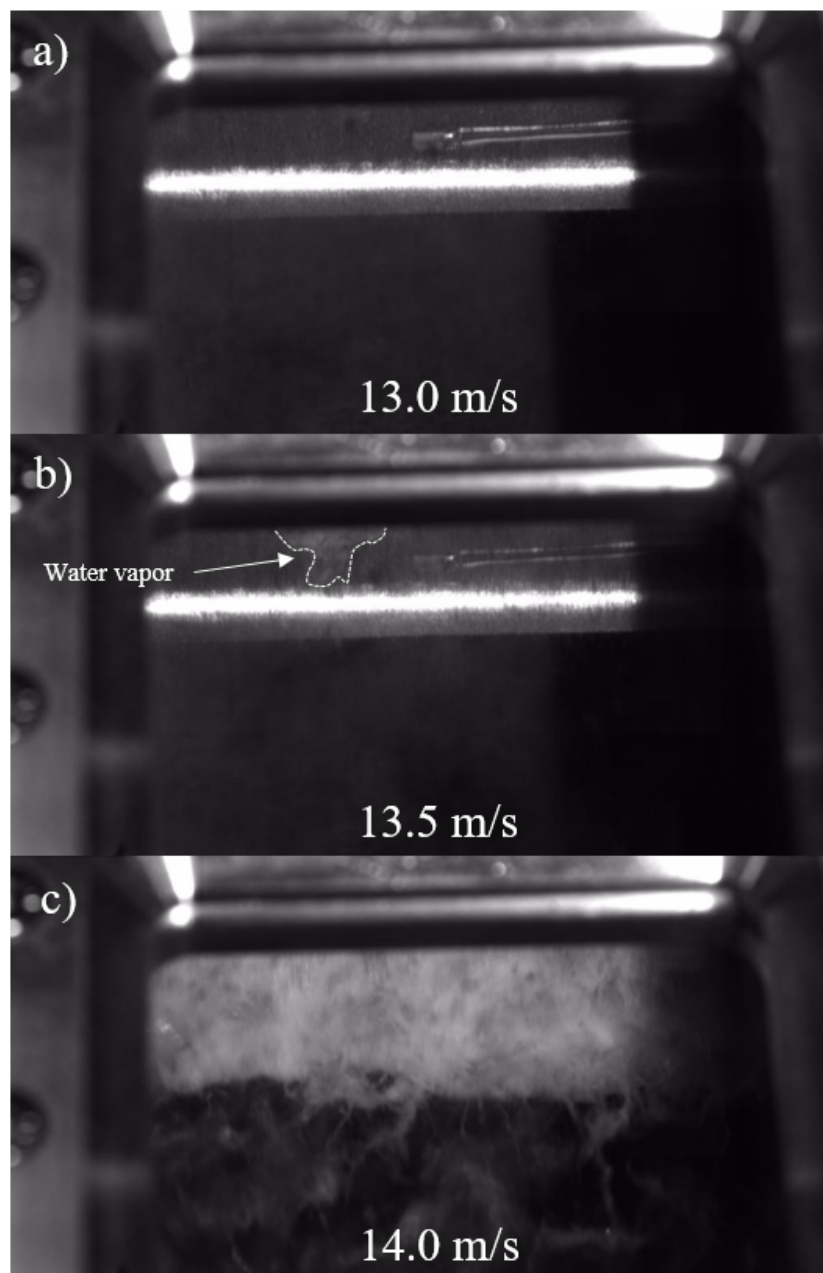


Figure 3.21: Cavitation in the cascade test rig. Photo: Bjørn Winther Solemslie.

The video of cavitation at the three flow velocities was further investigated by Solemslie. By analysing the difference in grey scale intensity of the video in an area close to the trailing edge, the patterns visualised in Figure 3.22 was obtained. The figure shows the difference in grey scale intensity at the hydrofoil trailing edge as a function of time. These plots are picked from the unpublished Memo *WP1.1 Revised geometry of hydrofoil in Blade Cascade for iteration 2* for the HiFrancis research project at NTNU. The Memo

is written by Solemslie the 3th of April 2017.

By investigating the difference in grey scale intensity at 13.5 m/s between 0.8 and 1 second, approximately 6 periods of the periodic signal is observed. This corresponds to a frequency of 30 Hz.

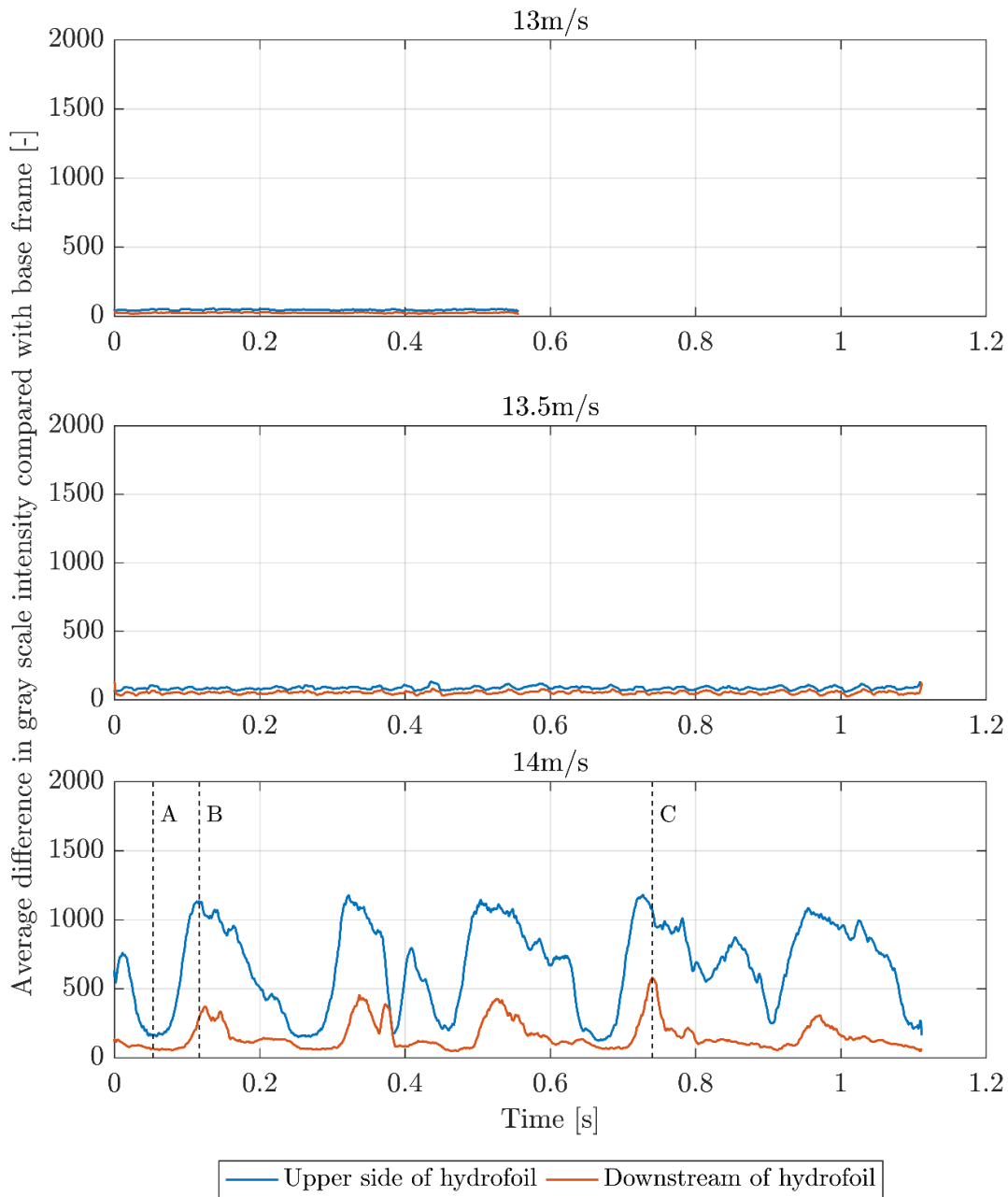


Figure 3.22: Cavitation grey scale intensity at 13.0, 13.5 and 14.0 m/s.

One of the objectives of this thesis is to further investigate the formation of water vapour in the cascade test rig. The main objective is to identify where the low-pressure zones

at the hydrofoil surface are located. The behaviour of the water vapour and the effect of cavitation versus vortex shedding frequency is also investigated.

To address these objectives, there will be performed both single-phase and two-phase CFD simulations. The identification of low-pressure zones may be done through a single-phase simulation. The setup will then be identical to the final numerical model used to design a new hydrofoil. Regarding the two-phase simulations with water vapour, a cavitation model is needed. As the formation of water vapour is strictly dependent on the pressure levels in the system, extra care has to be taken regarding the boundary conditions.

The Rayleigh-Plesset model described in section 2.4.1 is used to include the possible formation of vapour bubbles in the cascade rig. The mean bubble diameter is set to  $2 \cdot 10^{-6}$  m. As previously mentioned the Rayleigh-Plesset model used in Ansys CFX disregards the viscous term of the Rayleigh-Plesset equation 2.28. The vapour pressure of water is determined from the temperature of the water. The temperature of the water in the cascade test rig during the cavitation tests were approximately 15°C. By using Bucks equation [54] as presented in equation 3.1, the vapour pressure is found to be approximately 1705 Pa at this temperature.

$$p_{vap} = 611.21 \cdot \exp \left( \left( 18.678 - \frac{T}{234.5} \right) \left( \frac{T}{257.14 + T} \right) \right) \quad (3.1)$$

The inlet boundary condition is set to a bulk mass flow rate equivalent to a velocity of 14 m/s to imitate the chaotic behaviour seen during the experimental observations. The reference pressure is set to 1 atm. Regarding the outlet static pressure, this was not measured for the experimental observations. The total pressure 5 m in front of the cascade test section, where the computational domain starts, therefore need to be estimated based on the gage pressure in the pressure tank and the losses in the piping system. The pressure loss over the computational domain from the inlet to outlet may be calculated from a steady state CFD simulation at 14 m/s. The estimation of pressure losses from the pressure tank to the outlet of the numerical domain is presented in Appendix A. Based on this, the outlet static pressure is set to 65 007 Pa.

### 3.3 Natural Frequencies

The lock-in condition velocity range is equally dependent on both the vortex shedding frequency and the natural frequency of the system. Ansys 17.2 Mechanical with a modal analysis is used to predict the natural frequencies of the cascade test rig. A modal analysis utilise the Finite Element Method (FEM) to find the modes of the system. The system investigated is a small part of the square test section as presented in Figure 3.23.

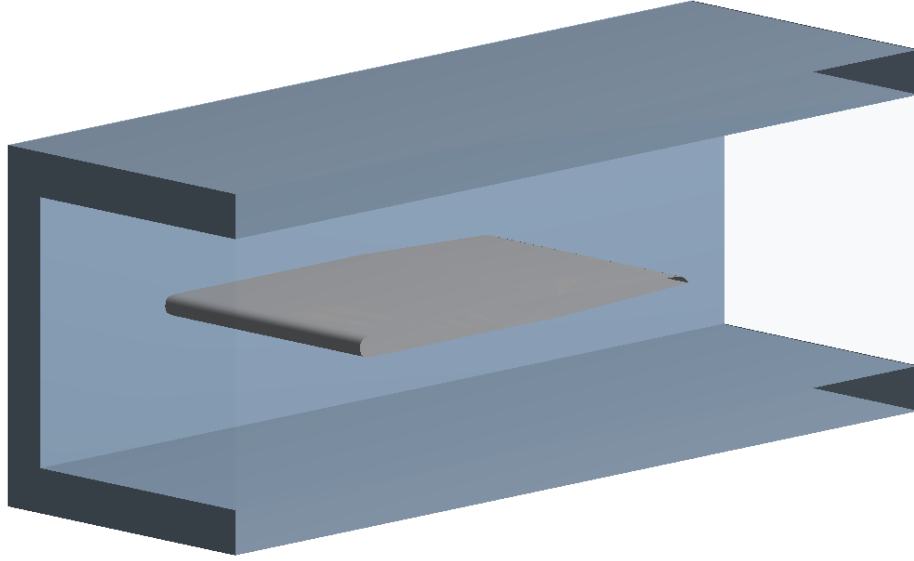


Figure 3.23: Section view of geometrical model for original hydrofoil used in modal analysis. The water is represented by the transparent body surrounding the hydrofoil.

Water is included in the model, such that the added mass of the viscous fluid is accounted for in the prediction of the natural frequency. The added mass of the water is included by using the Ansys extension Acoustics 17.2. This extension to Ansys Mechanical allows the user to model a body as an acoustic body. In order to do this, the density and speed of sound of the acoustic body must be specified. The density and speed of sound of the water is set to  $1000 \text{ kg/m}^3$  and  $1500 \text{ m/s}$  respectively.

The hydrofoil only is made out of aluminium, and the walls of the test section are made out of structural steel. The relevant material properties of the aluminium are presented previously in Table 3.1 and the material properties of structural steel are presented in Table 3.8. Compared to the original cascade test rig, the geometrical model is slightly simplified in the way that the hydrofoil part made out of aluminium in reality also consist of two plates on each side. Other simplifications are that the plexiglass windows and bolts are removed, in addition to that only a small part of the square test section is included.

<b>Property</b>	<b>Value</b>	<b>Unit</b>
Density	7850	$\text{kg/m}^3$
Young's modulus	$2.00 \cdot 10^{11}$	Pa
Poisson ratio	0.30	-

Table 3.8: Structural steel material properties.

At the front and back of the square test section, the fixed support boundary conditions are applied. No pres-stress will be applied, which means that the predicted natural frequency corresponds to a situation where the water is still. When including water in the model, the fluid-structure interaction is accounted for. The matrix system used to describe the



FSI at the interface is unsymmetric, and hence the unsymmetric solver setting is used [55].

Based on the results from the CFD analyses, there may be a need to lower the natural frequency of the system in order to fulfil the objectives of moving the lock-in condition to a low enough velocity range. The natural frequency of the cascade test rig will be lowered if the thickness of the hydrofoil is decreased. One strategy that may be considered, which is likely to not affect the vortex shedding frequency but decrease the thickness of the hydrofoil, is to move the chamfer point that is located 100 mm from the trailing edge of the original hydrofoil design closer to the leading edge.



## 4 Results and Discussion

This chapter presents the results obtained from the numerical investigations performed to address the objectives of this thesis. The results are selected based on their relevance to the objectives, and are discussed in light of theoretical background, previous work, experimental observations and the numerical setup.

The first section will describe the design of a new hydrofoil geometry where the lock-in condition is moved to a lower flow velocity. This is followed by the results obtained from the investigation of cavitation in the existing cascade test rig. The last section presents a general discussion on the numerical setup and strategy.

### 4.1 Design of a New Hydrofoil Geometry

This section first presents the results obtained from the fluid flow investigations on a new hydrofoil design and compare these to results obtained for the original design. The final numerical setup presented in the previous chapter is used for all fluid flow investigations. A modal analysis supports the findings from these investigations. The expected new lock-in range for the final hydrofoil design is presented at last.

#### 4.1.1 Final Hydrofoil Design

Based on the results presented in the previous chapter, the non-symmetric trailing edge with a 30-degree angle was the chosen trailing edge profile used for further studies. The trailing edge showed an increase in shedding frequency which is beneficial concerning moving the lock-in condition to a lower flow velocity.

The original hydrofoil was investigated at flow velocities 5, 10 and 15 m/s to act as a reference for the final design. Figure 4.1 shows the absolute pressure signal subtracted its average at the point P210. Figure 4.2 presents the FFT of the normalised signal over a longer time span.

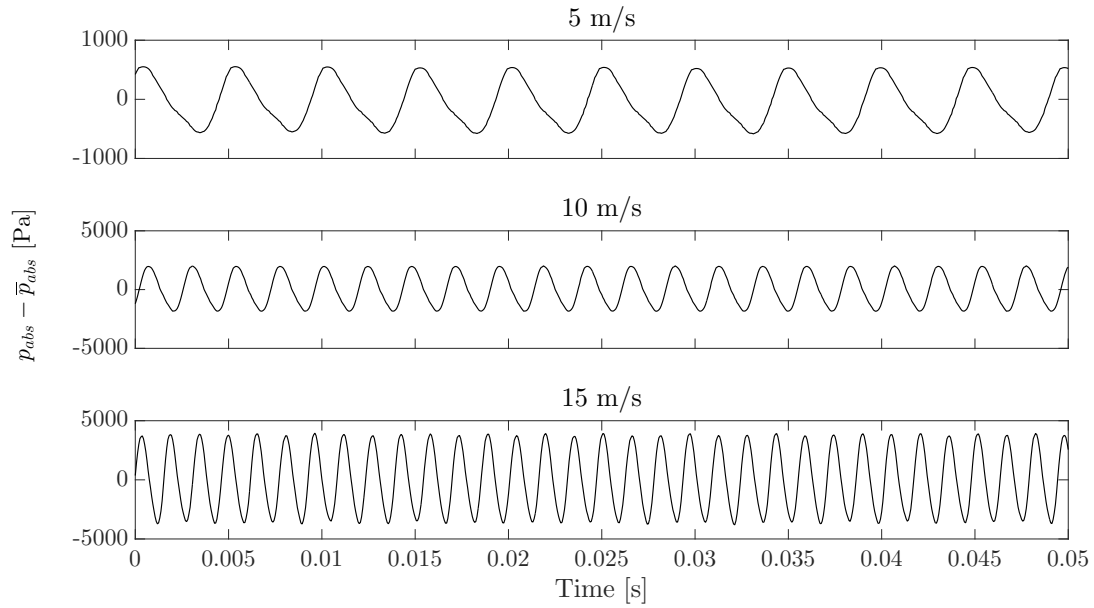


Figure 4.1: Absolute pressure signals subtracted its average at point P210 for original hydrofoil at 5, 10 and 15 m/s.

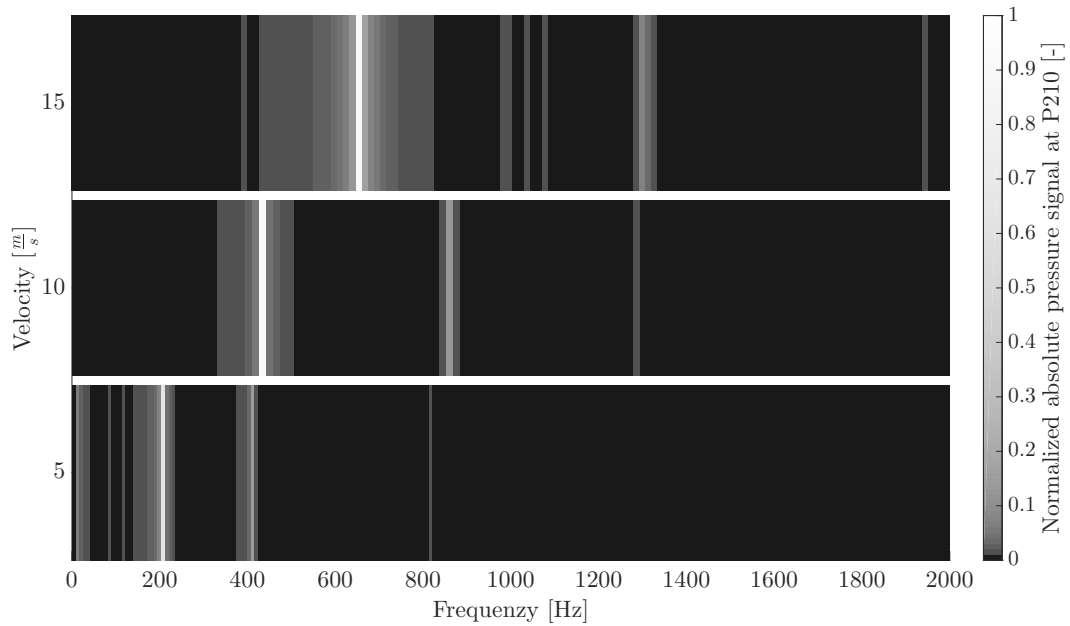


Figure 4.2: Intensity plot of FFT for original hydrofoil at 5, 10 and 15 m/s.

Table 4.1 presents the dominant frequencies seen in the FFT intensity plot. Except for these frequencies, the second harmonic is seen at 5 m/s and the second and third harmonic is seen at 10 and 15 m/s.

Velocity [ $\frac{m}{s}$ ]	$f_s$ [Hz]
5	203.3
10	426.0
15	644.9

Table 4.1: Dominant frequencies at velocities 5, 10 and 15 m/s observed in FFT intensity plot for original hydrofoil.

The new hydrofoil with the proposed trailing edge and chamfering as presented in Figure 3.20 in the previous chapter was run at 10 m/s. Similar plots as presented for the original hydrofoil are shown in Figures 4.3 and 4.4. It is observed that the amplitude of the absolute pressure signal is approximately a tenth of the amplitude of the original hydrofoil at the same flow velocity. The FFT intensity plot reveals a dominant frequency of 444.44 Hz which is an increase of 18.44 Hz, being less than could be expected based on the results of the constant thickness hydrofoil tests.

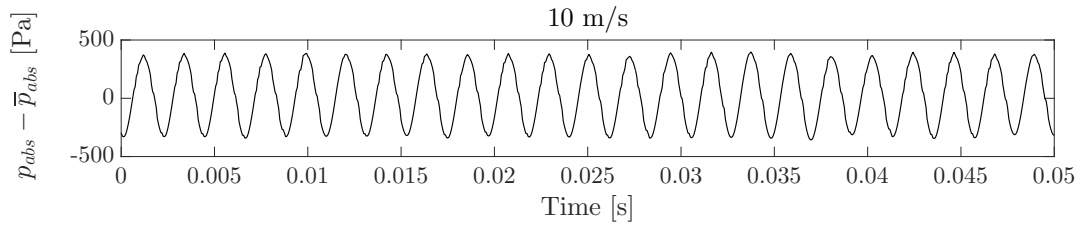


Figure 4.3: Absolute pressure signals subtracted its average at point P210 for chamfered hydrofoil with proposed trailing edge at 10 m/s.

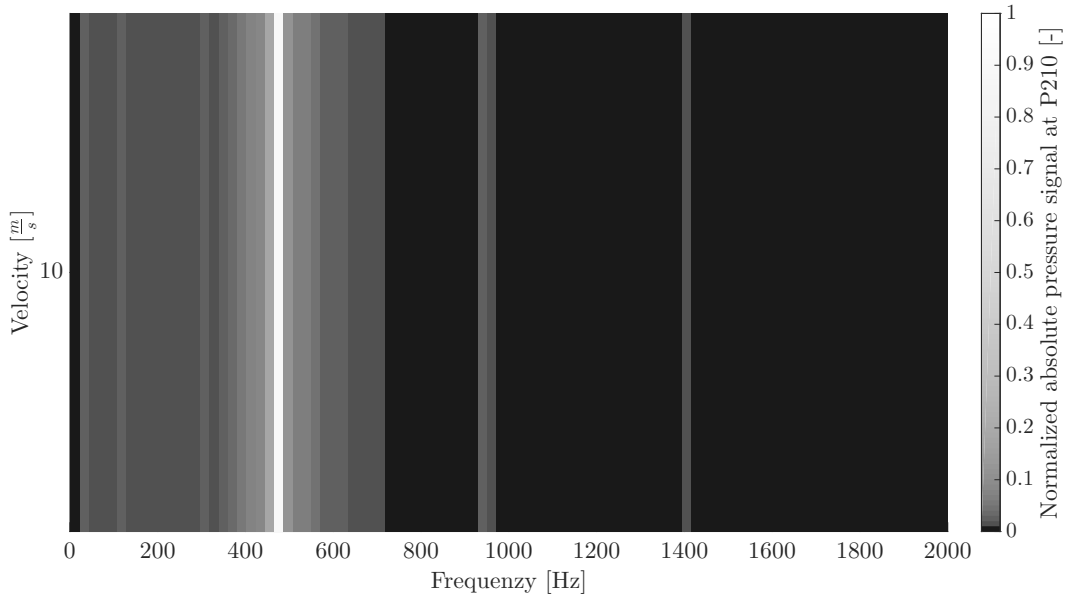


Figure 4.4: Intensity plot of FFT for chamfered hydrofoil with proposed trailing edge at 10 m/s.

As the increase in vortex shedding frequency was lower than expected, a hydrofoil with the new proposed trailing edge with a moved chamfer point was investigated. The intention was to lower the natural frequency by reducing the thickness of the hydrofoil. The chamfer point was moved 100 mm closer to the leading edge. This hydrofoil is visualised in Figure 4.5. The results of the investigations on this hydrofoil at 5, 10 and 15 m/s are shown in Figures 4.6 and 4.7.



Figure 4.5: Hydrofoil with moved chamfer point and proposed trailing edge.

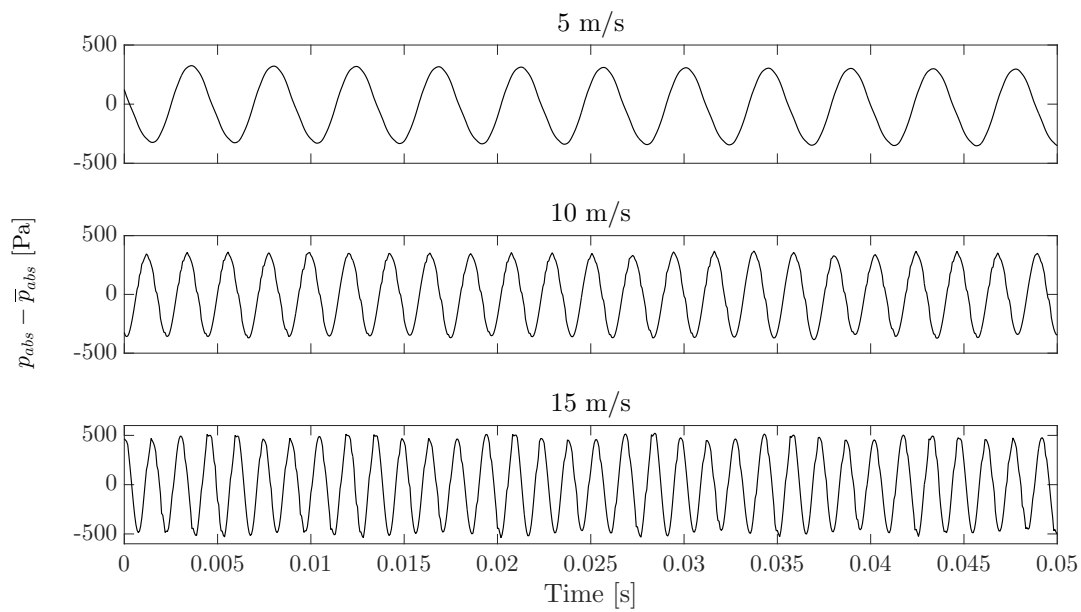


Figure 4.6: Absolute pressure signals subtracted its average at point P210 for hydrofoil with moved chamfer and proposed trailing edge at 5, 10 and 15 m/s.

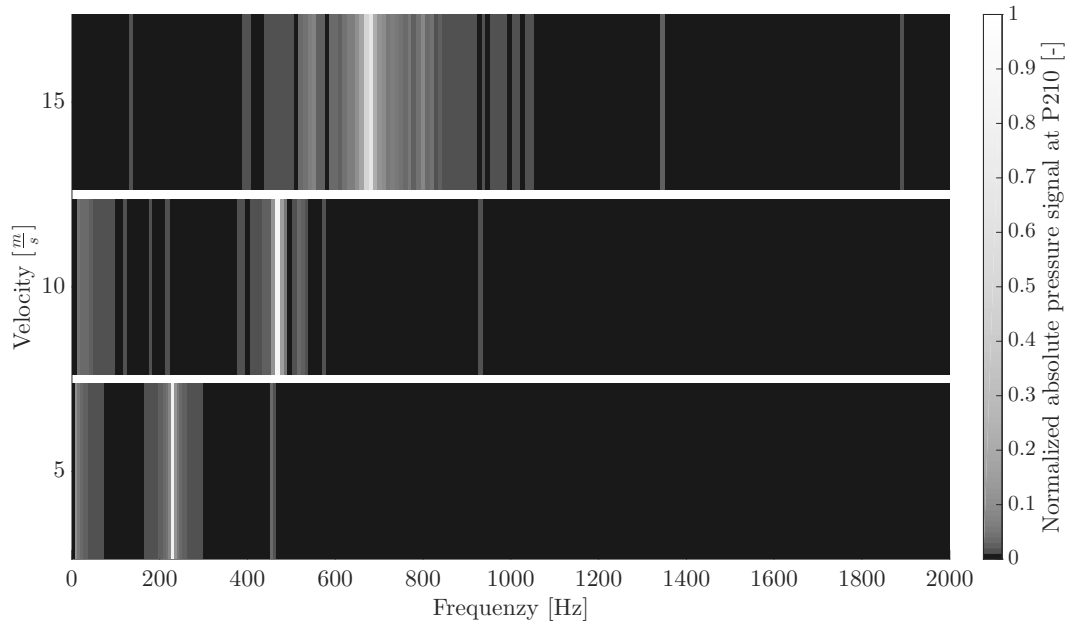


Figure 4.7: Intensity plot of FFT for hydrofoil with moved chamfer and proposed trailing edge at 5, 10 and 15 m/s.

Table 4.2 presents the dominant frequencies seen in the FFT intensity plot in Figure 4.7. Except for these frequencies, the second harmonic is seen at 5 and 10 m/s and the second and third harmonic is seen at 15 m/s.

Velocity [ $\frac{m}{s}$ ]	$f_s$ [Hz]
5	225.8
10	462.7
15	674.9

Table 4.2: Dominant frequencies at velocities 5, 10 and 15 m/s observed in FFT intensity plot for hydrofoil with moved chamfer and proposed trailing edge.

The hydrofoil with moved chamfer and the proposed trailing edge exerts a higher vortex shedding frequency than the one where the chamfer point is not moved. The increase at 10 m/s, compared to the original design, is 36.7 Hz, which is approximately the double of the increase with the non-moved chamfer point hydrofoil. The amplitude was still found to be approximately a tenth of the original design. The hydrofoil with moved chamfer and the proposed trailing edge was therefore chosen as the final design.

Figure 4.8 presents a direct comparison of the vortex shedding frequency of the original hydrofoil and the new proposed design. What is seen is that the two lines have approximately the same slope. The line representing the new design is only shifted to higher frequencies. Based on the results and formulas presented by Heskestad and Olberts [21] and Brekke [23], this is not what is expected.

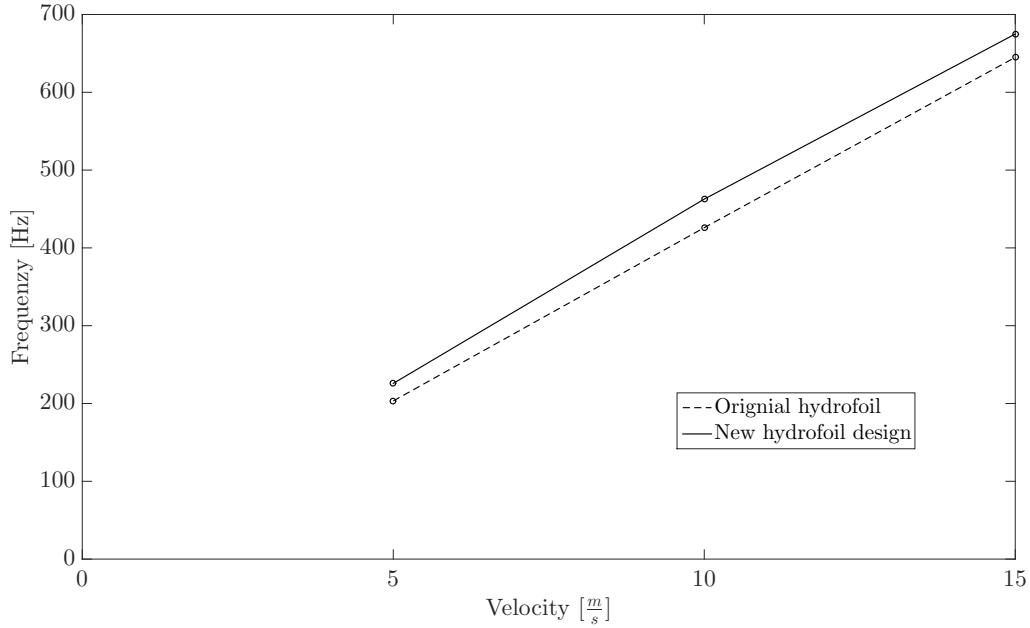


Figure 4.8: Dominant frequencies at velocities 5, 10 and 15 m/s observed in FFT intensity plot for final hydrofoil design.

To further investigate both the low increase in frequency and small change in slope of the new hydrofoil design, the velocity contour for all three above mentioned hydrofoils at 10 m/s is presented in Figure 4.9.

Roshko [15] claimed that as separated shear layers are brought closer together, the vortex shedding frequency increases. By investigating the velocity contour of the three hydrofoils, the wake regions are seen to be pretty similar in both size and shape. The distance between the two separated shear layers are believed to be much alike and thereby exerting similar vortex shedding frequencies. However, the wakes of the hydrofoils with the proposed TE are seen to be slightly narrower and elongated.

The lock-in condition occurred at about 11 m/s and 623 Hz in the experiment, which means that the vortex shedding frequency was 623 Hz at this flow velocity. The vortex shedding frequency was not investigated numerically at 11 m/s for the original design, but based on the numerical results at 10 and 15 m/s, the vortex shedding frequency is presumably about 200 Hz less than that obtained in the experiments at 11 m/s. This indicates that the distance between the two separated shear layers for the original design is likely to be predicted to be too large by the numerical model.

Another reason affecting the vortex shedding frequency seen in the experiment is that that during manufacturing, the trailing edge cannot be made infinitely sharp as in the numerical investigations. The trailing edge is rounded off by a tiny radius which might affect the vortex shedding frequency.

By examining the velocity contour of the original hydrofoil, it is seen that the velocity



field is significantly more influenced by the vortex shedding than for the other hydrofoils. This ought to explain the high amplitudes of the original design. The original trailing edge seems to oppose a greater disturbance to the flow.

The highest velocities are seen on top and bottom of the leading edge where the geometry has its largest curvature, leading to an acceleration of the flow. It is observed that the highest velocity in the domain is higher for the two designs with the new TE compared to the original design. The proposed design, the hydrofoil with moved chamfer, has the highest velocity. The difference is small, but somewhat unexpected as the cross-sectional area in the test section is increased as the hydrofoil volume is decreased, which should lead to a decreased flow velocity. As the difference is small, the variation might be due to that the velocity contours are taken at different time instances of the vortex shedding phenomena. The periodic detachment of vortices at the TE is the consequence of instabilities between the pressure and suction side. Hence, the flow instabilities seen at the trailing edge are likely to be present at the leading edge as well.

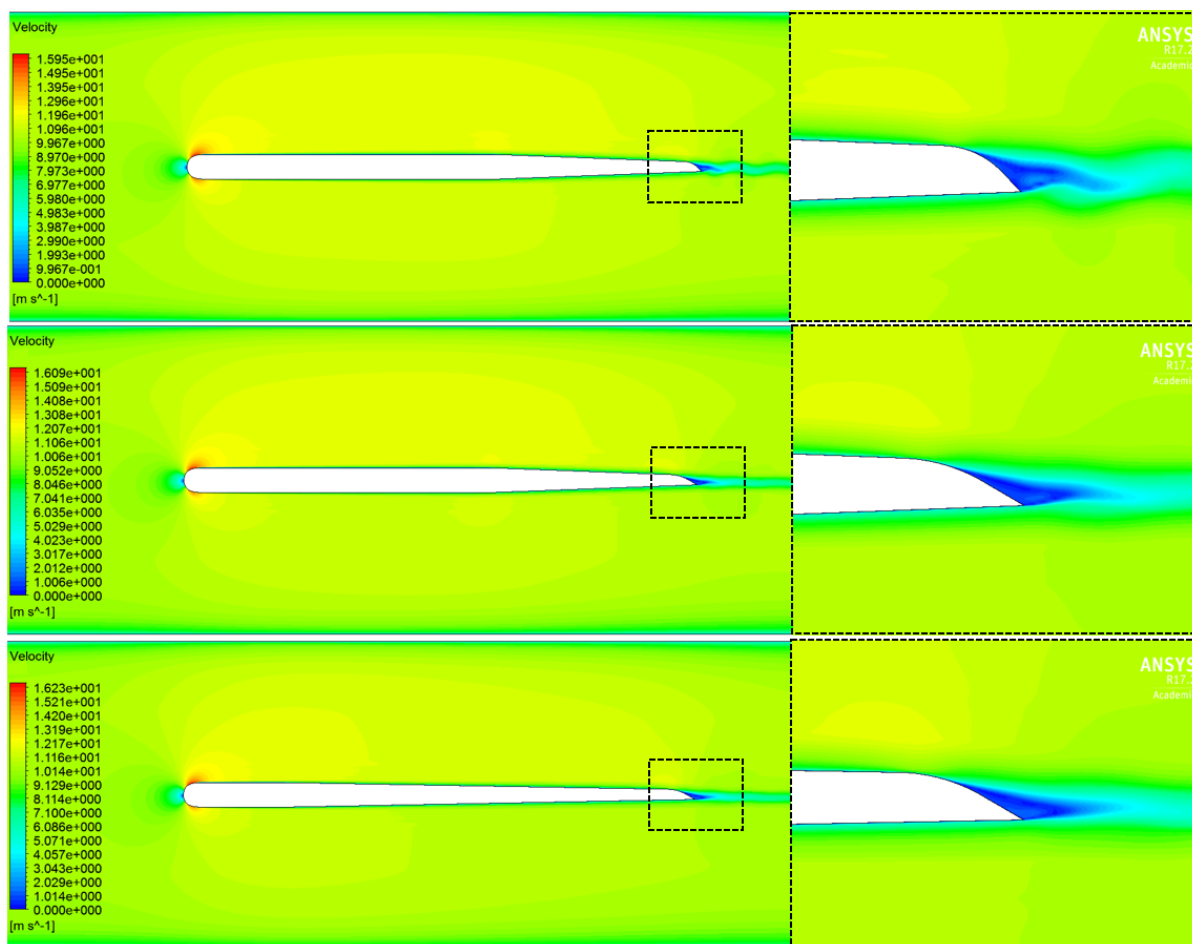


Figure 4.9: Velocity contour of, from top to bottom, original hydrofoil design, hydrofoil with proposed TE and final hydrofoil design at 10 m/s.

Figure 4.10 shows the  $\lambda_2$ -criterion with velocity contour at a flow velocity of 10 m/s for all the three hydrofoils. The periodic detachment of vortices at the trailing edge is indeed

present. At a level of 0.001, the  $\lambda_2$ -criterion detects vortices about half the length of the hydrofoil downstream the TE.

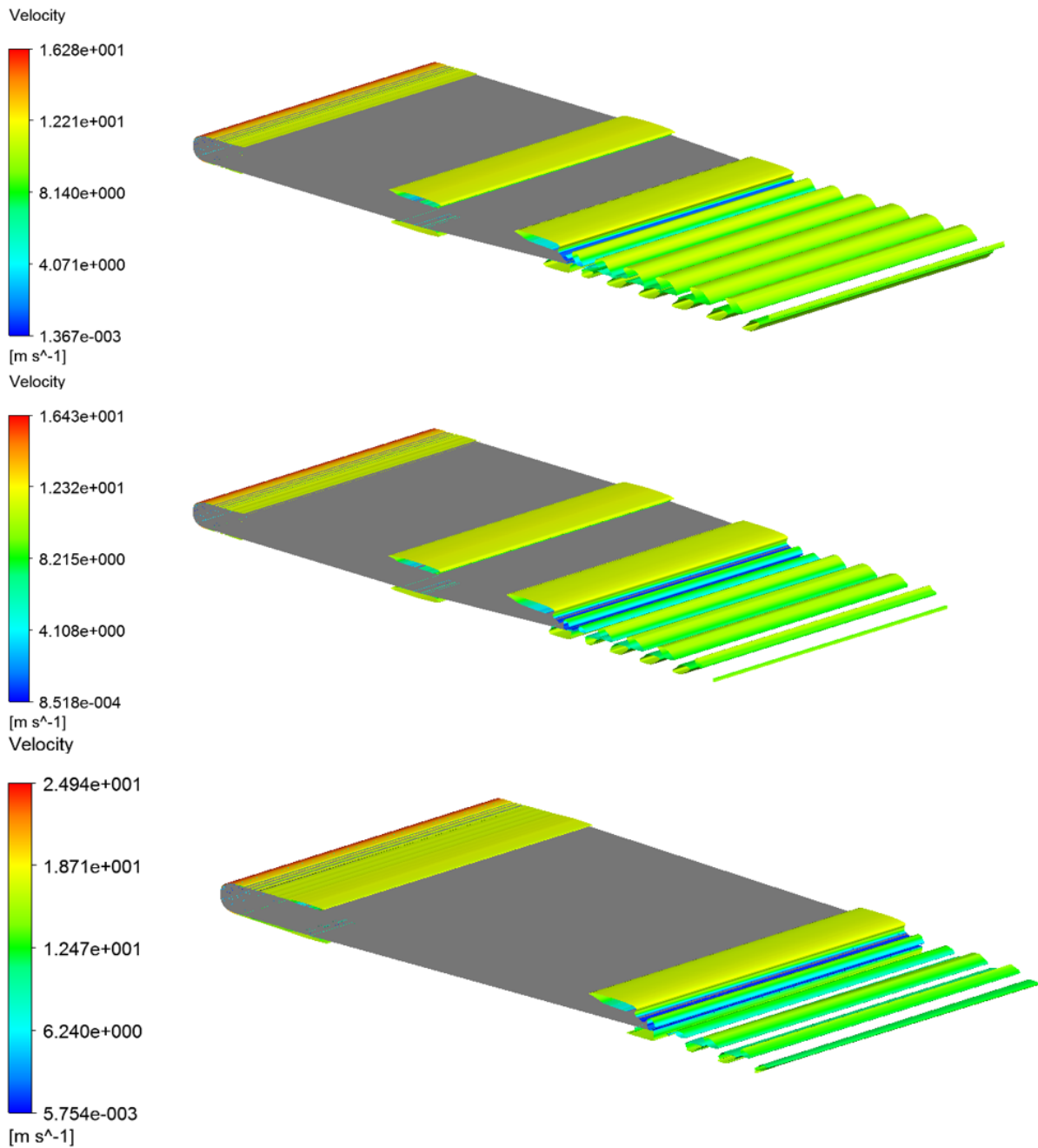


Figure 4.10:  $\lambda_2$ -criterion at a level of 0.001 with velocity contour for, from top to bottom, original hydrofoil design, hydrofoil with proposed TE and and final hydrofoil design at 10 m/s.

The vortices of the hydrofoils with the new trailing edge are smaller than the original design, which may explain the smaller absolute pressure amplitudes presented previously in this chapter. The distance between the vortex structures is not seen to be significantly

different for the three hydrofoils.

For the hydrofoil with moved chamfer, the large vortex structure seen at the chamfer point for the other hydrofoils no longer exists. A smaller structure is seen where the new chamfer point is located. This vortex structure may be smaller because of influence from the high-velocity flow at the leading edge.

The zoomed in velocity contour presented in Figure 4.9 show that the flow velocity is higher at the surface where the hydrofoil starts to curve at the trailing edge for all hydrofoils. This is represented by a "bump" in the velocity contour in this area. The  $\lambda_2$ -criterion may explain this phenomenon. The point where the velocity is higher seems to be straight behind where the large vortex structure located close to the TE is. If the flow in this vortex is rotating clockwise, the flow is pushed down towards the hydrofoil surface.

The absolute pressure contour for all hydrofoils at 10 m/s is presented in Figure 4.11. The highest pressure is seen at the leading edge where a stagnation point seem to be located. Low-pressure zones are located on top and bottom of the leading edge. These low-pressure zones are indicating flow separation, which is supported by the  $\lambda_2$ -criterion indicating a vortex structure with the form of a "film" in this region. Low-pressure zones are also seen at the chamfer point.

The flow within the low-pressure zones at the LE are prone to cavitate as can be seen from the pressure level. The reference and outlet static pressure were set to 1 and 0 atm respectively, which means that where the pressure is below zero is where the flow would cavitate if no external pressure were applied in the experiment. However, as a 10 bar gage pressure is possible in the cascade test rig, cavitation may be avoided for the flow conditions at 10 m/s. Still, it is important to note that the new proposed hydrofoil design is more prone to cavitate as this hydrofoil has the lowest absolute pressure level on top of the leading edge of the three.

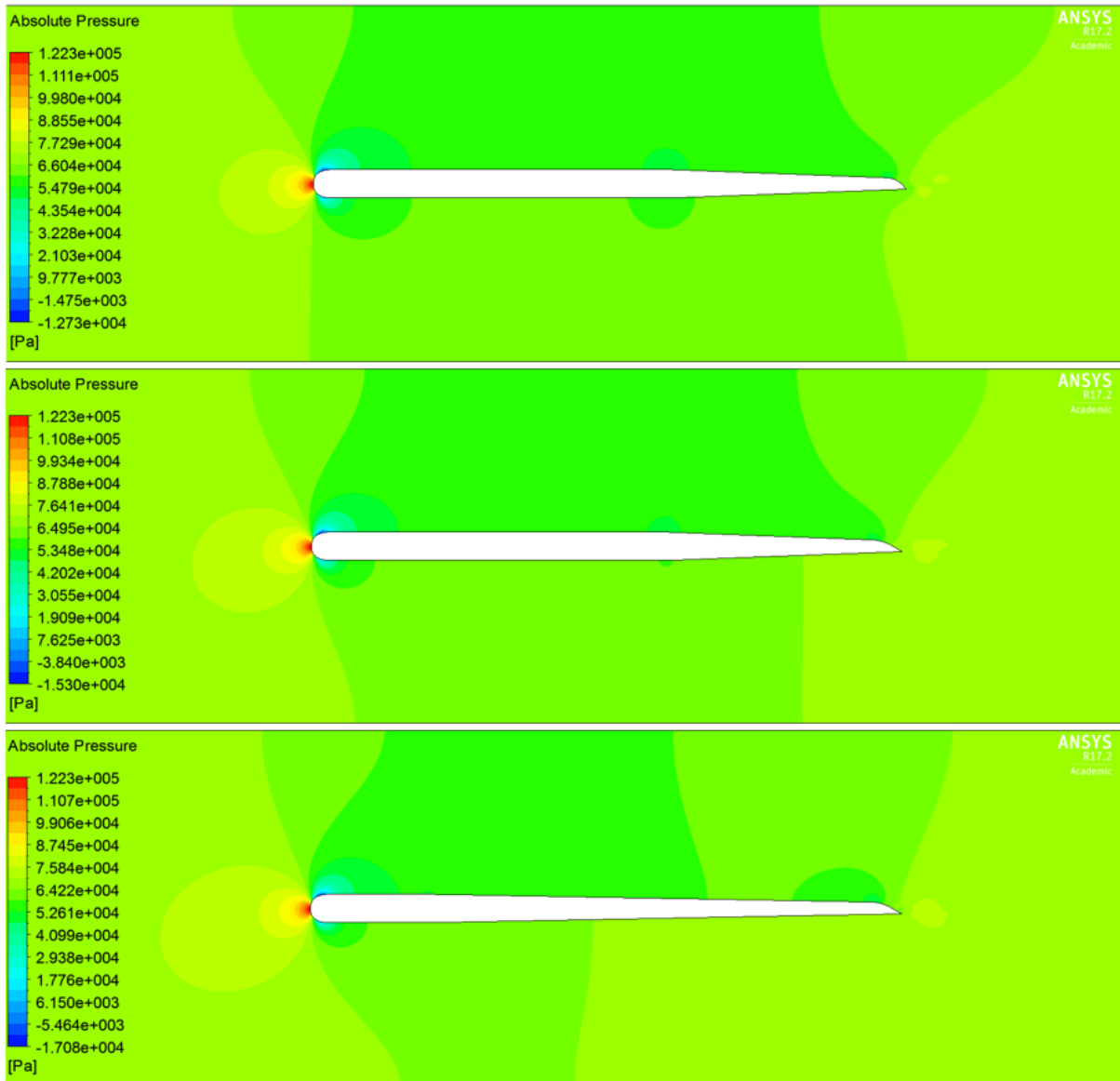


Figure 4.11: Absolute pressure contour of, from top to bottom, original hydrofoil design, hydrofoil with proposed TE and final hydrofoil design at 10 m/s.

### 4.1.2 Change of Natural Frequency

By moving the chamfer point, the intention was to lower the natural frequency of the hydrofoil. Figure 4.12 presents the first mode, the natural frequency, of the original hydrofoil and the new proposed design obtained in a modal analysis. The first mode has the shape of one wave in the transverse direction and one quarter of a wave in the lengthwise direction for both designs. As can be seen, the new design leads to a natural frequency being 151.81 Hz less than for the original design.

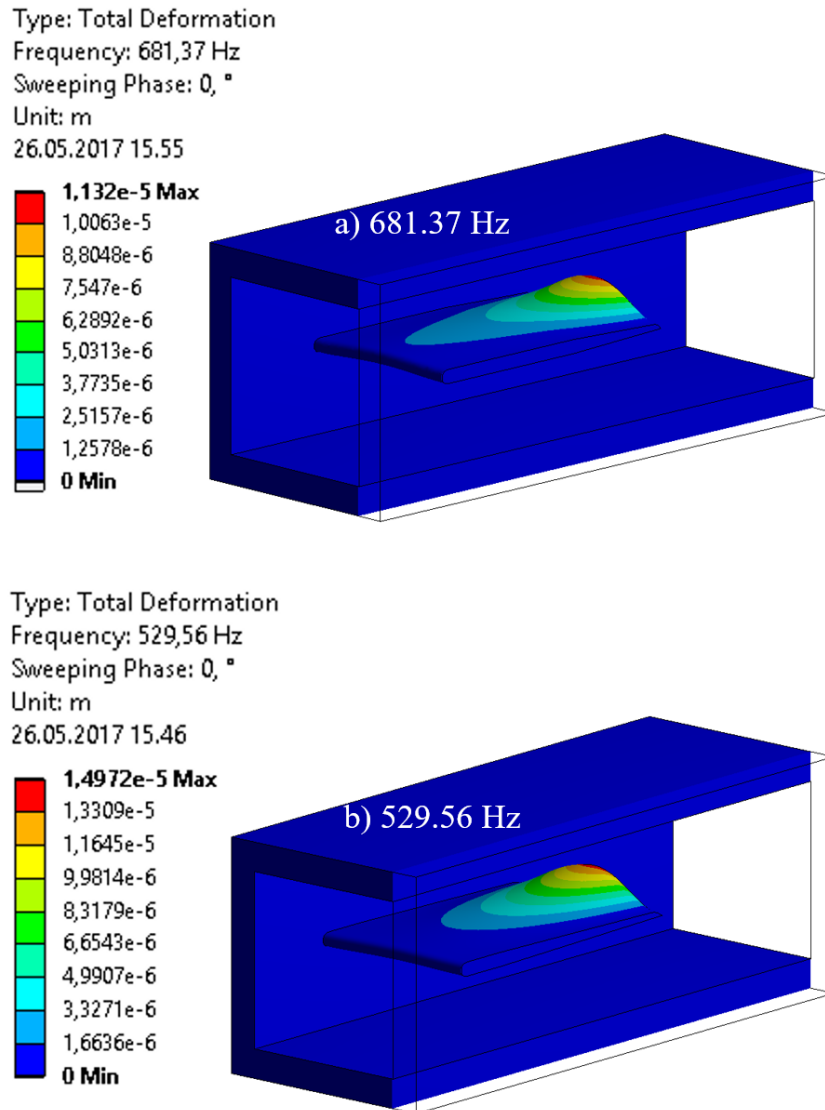


Figure 4.12: a) first modal shape and resulting natural frequency for original hydrofoil design, b) first modal shape and resulting natural frequency for the new hydrofoil design

Appendix B presents a mesh independence study for both modal analyses and the final mesh used for the modal analysis of the new hydrofoil design.

The lock-in condition occurred at a frequency of 623 Hz, indicating that the natural frequency of the original design is overestimated in the modal analysis. The model used in the modal analysis is simplified compared to the experimental setup. The whole cascade test rig hangs loose in the air and is a lot longer than the model used in the modal analysis. It is assumed that the short part of the test section used for the modal analysis is too stiff, leading to a higher natural frequency.

Another simplification made in the model that may increase the stiffness of the setup, is that only the hydrofoil itself is given the material properties of aluminium. Aluminium has a lower Young's Modulus than structural steel and is thus more flexible. The bolts

constraining the hydrofoil part was not included in the model either. In addition to all other constraints of the setup, this may make the experimental setup more flexible.

The total deformation in Figure 4.12 shows that the total displacement of the new hydrofoil is larger. The new hydrofoil may be prone to exert larger vibration amplitudes. However, the amplitude of the vortex shedding is decreased by approximately a factor of ten, which is a larger reduction than the observed increase of total deformation.

### 4.1.3 New Lock-In Condition

By combining the effect from the increased vortex shedding frequency and the decreased natural frequency of the new proposed design, the new lock-in velocity may be estimated. As neither the vortex shedding frequency or the natural frequency of the original hydrofoil did hit 623 Hz at 11 m/s, the relative differences are used to estimate the new lock-in condition.

The natural frequency was decreased by 151.81 Hz. By subtracting this from the correct natural frequency of the cascade test rig, 623 Hz, a natural frequency of 472.19 Hz is obtained.

Regarding the vortex shedding frequency of the new design, the slope of the curve representing the vortex shedding frequency at 5, 10 and 15 m/s was similar to the slope of the original curve. The slope was therefore not chosen as a measure to estimate the new lock-in condition. Instead, the difference at 10 m/s, being 36.7 Hz, is used to estimate the difference in vortex shedding frequency at a velocity of 11 m/s. This leads to an estimated vortex shedding frequency of 659.7 Hz at 11 m/s.

Figure 4.13 shows the original lock-in point and the expected new lock-in point based on the estimates for the natural frequency and vortex shedding frequency. The new lock-in condition is estimated to be present at a velocity of 7.87 m/s.

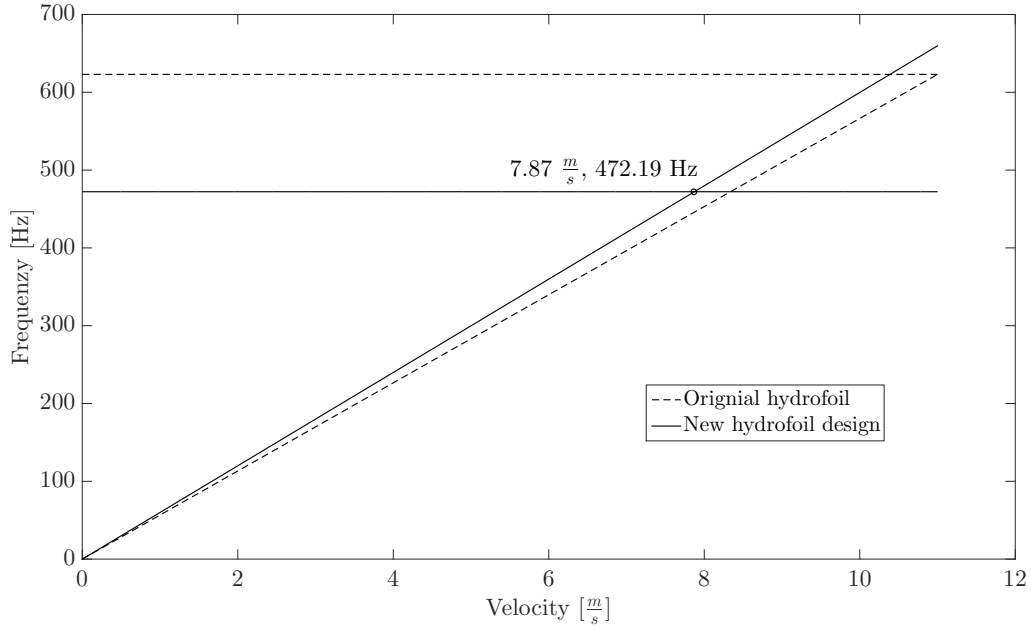


Figure 4.13: New lock-in flow velocity.

As the amplitude of the vortex shedding of the new hydrofoil design is approximately a tenth of the original design. The range of velocities in which the lock-in condition occurs is expected to be decreased based on the work by Bearman [35]. The decreased amplitude is also assumed to decrease the vibration amplitude during the lock-in. As the lock-in condition velocity is not decreased by more than 28.45 %, the reduction in amplitude is an important contribution to decreasing the unwanted vibration experienced during the lock-in condition.

## 4.2 Cavitation

This section presents the results obtained by investigating cavitation in the fluid domain of the original cascade test rig. A single-phase simulation, with a similar numerical setup as for the ones presented in the previous section, at a flow velocity of 14 m/s was performed and used as a reference case. The absolute pressure signal subtracted its average at the point P210 and the FFT intensity plot of the normalised signal for the reference case is shown in Figures 4.14 and 4.15. The dominant frequency of the absolute pressure signal is found to be 599.1 Hz. This corresponds well with the vortex shedding frequencies obtained at 5, 10 and 15 m/s, presented in the previous section.

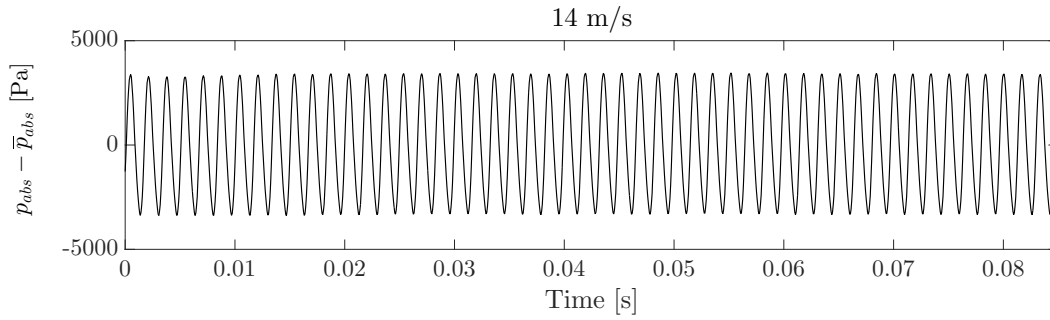


Figure 4.14: Absolute pressure signals subtracted its average at point P210 for original hydrofoil at 14 m/s.

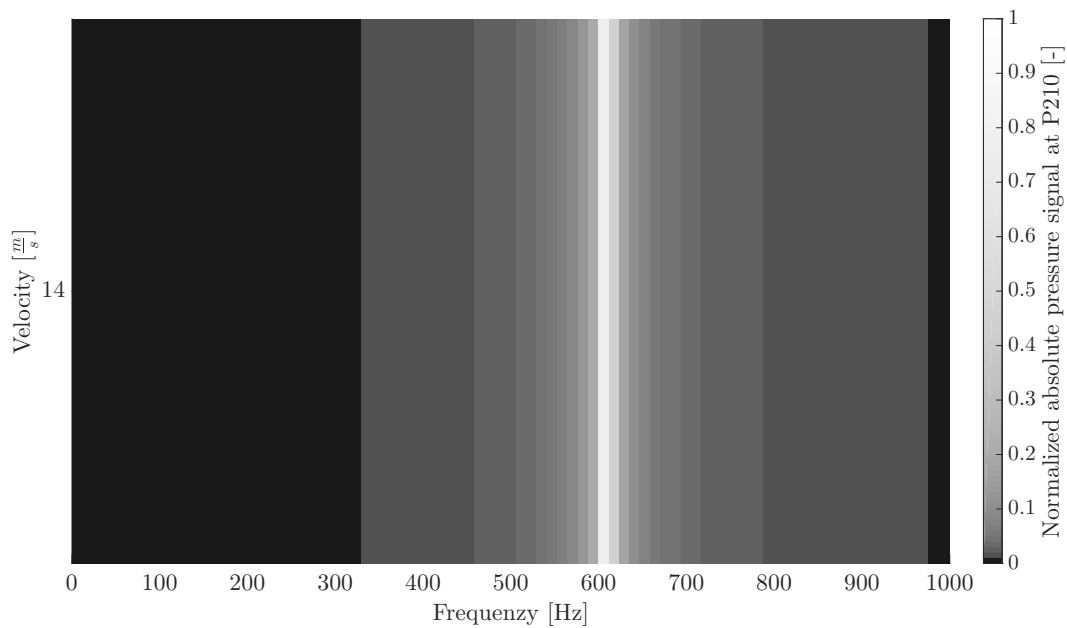


Figure 4.15: Intensity plot of FFT for original hydrofoil at 14 m/s.

With an established reference case, the two-phase model with water and water vapour was investigated with the Rayleigh-Plesset cavitation model. Note that the outlet static pressure was set to 65 007 Pa, based on the pressure losses calculated in Appendix A, not 0 Pa as for the reference case presented above. The absolute pressure signal subtracted its average at the point P210 is presented in Figure 4.16. The signal is significantly different from the reference case. The signal is seen to have two clear dominant frequencies, a low and high frequent part. The high frequent part has a frequency similar to the reference case and is believed to be due to the vortex shedding. The low-frequent and high-amplitude part of the signal is believed to be due to cavitation.



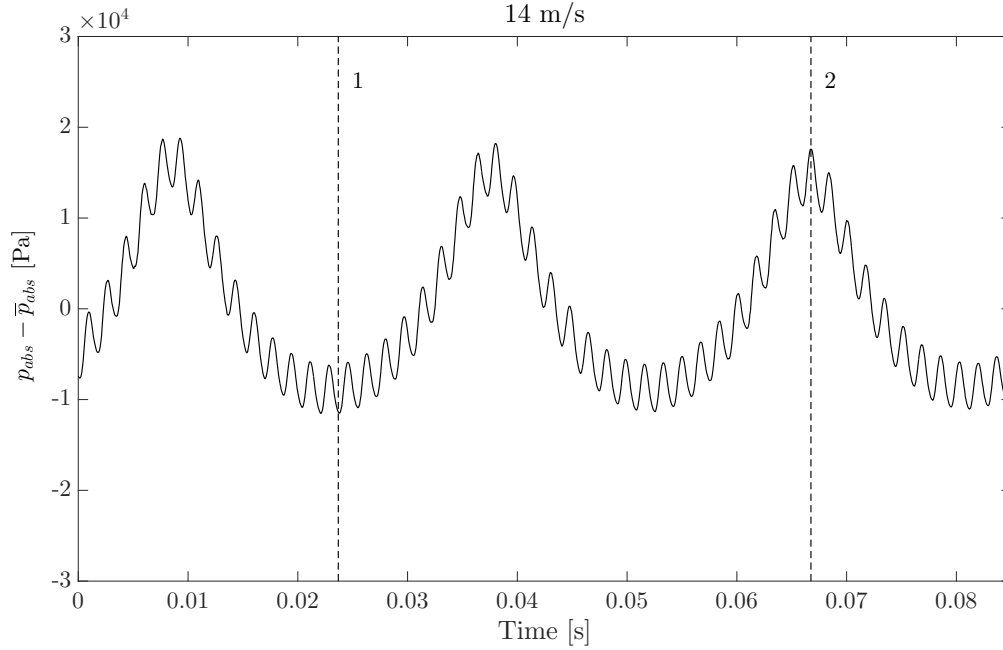


Figure 4.16: Absolute pressure signals subtracted its average at point P210 for original hydrofoil with cavitation model at 14 m/s.

The simulation was paused at the instances marked 1 and 2 in Figure 4.16 to create a result file. This was done such that the whole fluid domain could be investigated, not only the monitor points. Figure 4.17 presents the volume fraction of water vapour in the fluid domain at the point 1 and 2. At point 1, the pressure is at its lowest, and the amount of water vapour is seen to be significantly higher than at point 2 where the pressure is high. At point 1, water vapour is observed at both the top and bottom of the leading edge. At point 2, only a small water vapour film is seen on top of the leading edge. The strongest water vapour concentration is observed closest to the hydrofoil surface for both cases. Water vapour is not seen at any other locations than at the top and bottom of the leading edge in the fluid domain at any time instances.

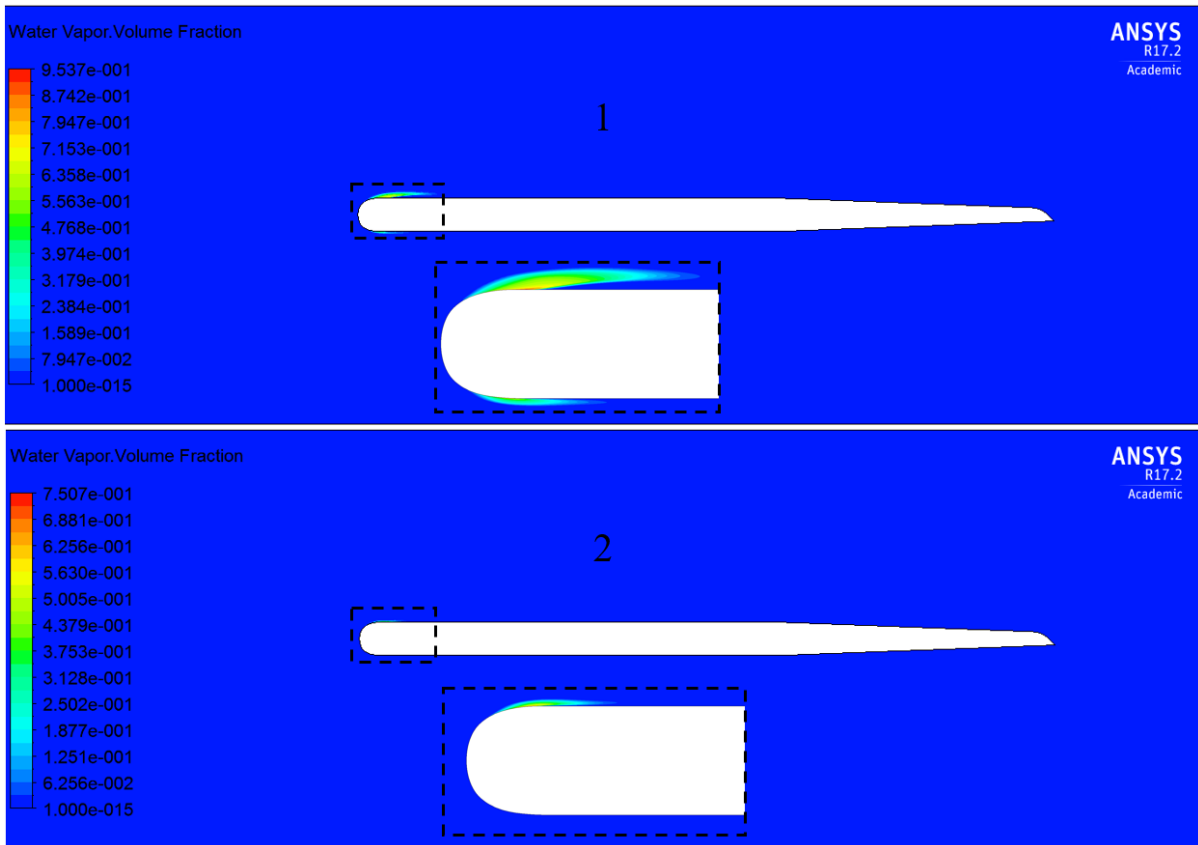


Figure 4.17: Water vapour volume fraction contour at time instances 1 and 2.

By analysing a longer part of the time series presented in Figure 4.16, the FFT intensity plot presented in Figure 4.18 is obtained. The low frequent part of the signal is seen to have a frequency of 35.13 Hz with the second, third, fourth and fifth harmonic frequency present in the FFT intensity plot. This frequency correspond well with the experimental observations at 13.5 m/s presented in Figure 3.22 in section 3.2.8. The frequency of the difference in grey scale at a flow velocity of 13.5 m/s was approximately 30 Hz, close to what obtained in these numerical investigations. As the behaviour is similar to the flow at 13.5 m/s, not 14 m/s, it is believed that the set outlet static pressure is higher than it was in the experimental observations at a flow velocity of 14 m/s. The estimated pressure loss in the piping system is believed to be too low. Regarding the amplitude of the low frequent part of the signal, this is not comparable to the experimental grey scale investigations.

Although close correspondence with the low-frequent part of the signal presented in Figure 4.16 and the experimental observations, water vapour was not seen at the location where cavitation was investigated in the experiment. It still seems that the pressure level at the point P210 is heavily influenced by the periodic water vapour content. The reason why water vapour is not observed close to the TE for the numerical investigations may be that the pressure in the experimental observations at 13.5 m/s was lower, allowing water vapour bubbles to travel downstream without imploding. Another explanation is that transient flow conditions in the piping system allows the water vapour to maintain

its state.

The temperature is also affecting the pressure conditions. The temperature was not stable during the experimental observations. The temperature increases due to fluid friction in the piping system, and as time goes the temperature of the water increases. By using Bucks equation, the vapour pressure is 1 7052 Pa at 15 °C and 2 338 Pa at 20 °C. If the temperature, in reality, was 5 degrees higher than assumed, the flow would be more susceptible to cavitate. This might also explain that the behaviour of the cavitating conditions was close to what observed at 13.5 m/s than at 14 m/s.

The vortex shedding frequency is observed at 590.8 Hz. This is lower than for the reference case, which contradicts what was observed by Ausoni [31]. However, the percentage decrease during cavitating conditions is only 1.39 % which is a lot less than the increase of 15 % observed by Ausoni. The hydrofoil investigated by Ausoni was significantly different than the one investigated in this thesis, being symmetrical and with an oblique trailing edge. The vortex shedding frequency may exert different behaviour during cavitating conditions for different hydrofoil designs.

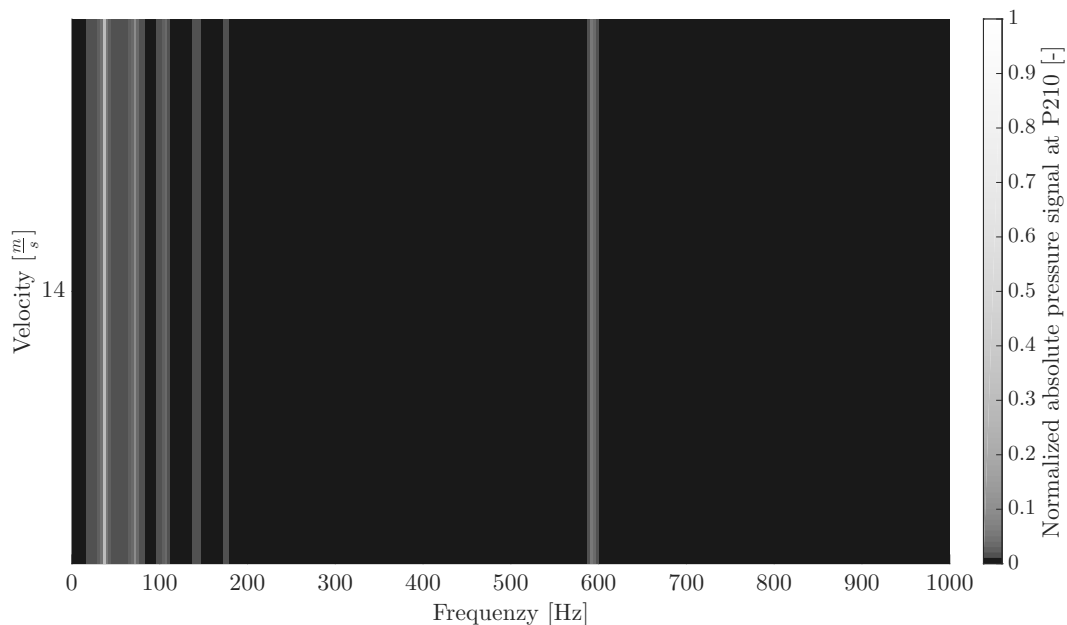


Figure 4.18: Intensity plot of FFT for original hydrofoil with cavitation 14 m/s.

To further investigate the lowered vortex shedding frequency and the periodic change of the water vapour concentration in the fluid domain, the total and absolute pressure contour are investigated. The total pressure contour is investigated instead of the velocity contour, as the velocity contour cannot be obtained for two-phase flows in CFX-post. The total pressure includes both the static and dynamic pressure and hence provides a comparison of velocity fields.

The total pressure contour of the reference case and the cavitating case at time instance 1

and 2 are presented in Figure 4.19. The total pressure does not include the atmospheric reference pressure of 1 atm. Thus the pressure level is negative in some places of the domain. As mentioned earlier, the outlet static pressure of the reference case is set to 0 Pa, which is the reason for the lower pressure levels for that case.

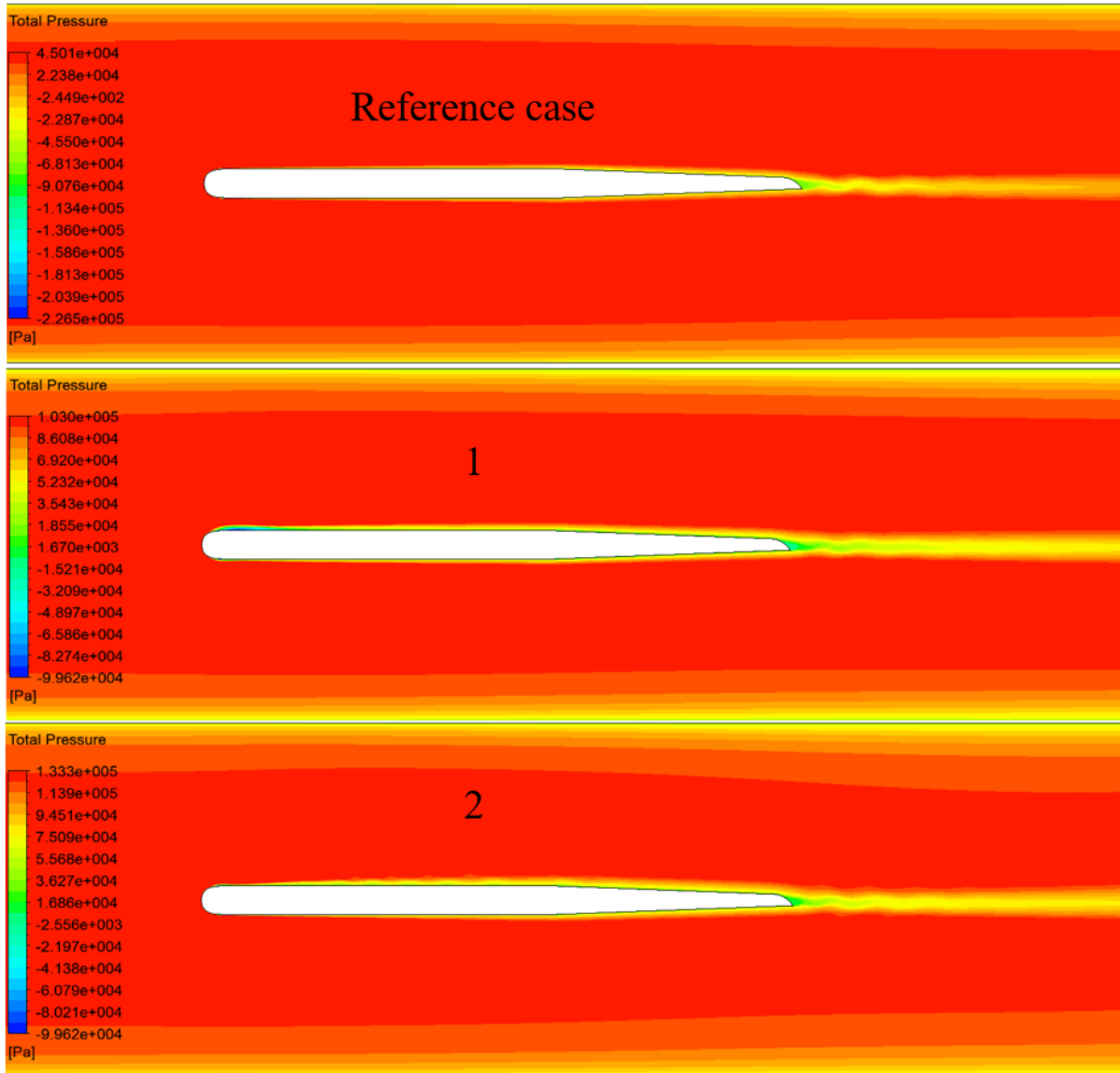


Figure 4.19: Total pressure contour, from top to bottom, without cavitation model, with cavitation model at time instance 1, with cavitation model at time instance 2. All at a velocity of 14 m/s.

The total pressure contours reveal that the wake size is slightly bigger for the cases with the cavitation model. This might explain the lower vortex shedding frequency at cavitating conditions as the distance between the separated shear layers is larger. The total pressure contour is significantly different for the two time instances 1 and 2. For time instance 1, there are large regions of low total pressure on top and bottom of the leading edge. For time instance 2 these regions are smaller, and a wavy pattern is observed on

top of the hydrofoil. Compared to the water vapour volume fraction contours, the wavy pattern of the total pressure at time instance 2 may be due to the breakdown of the water vapour region at the leading edge. The breakdown of the water vapour seem to cause disturbances to the flow on top of the hydrofoil.

The absolute pressure contour is presented for all cases in Figure 4.20. One of the objectives of this thesis was to identify the low-pressure zones in the existing cascade test rig. The absolute pressure contour of the reference case reveals these zones, which are seen to be located at the top and bottom of the leading edge, and at the chamfer point. The excessive curvature at these points, which accelerate the flow, ought to be the reason for these low pressures. If the hydrofoil curvature at the leading edge was reduced, for example by creating an oval shaped leading edge, cavitation might be avoided.

By comparing the absolute pressure contours at the time instances 1 and 2, the low-pressure zone where cavitation originates is seen to be significantly different in size. At point 1, where the amount of water vapour in the fluid domain is at its highest, the low-pressure zone is bigger than for the time instance 2. Compared to the wavy pattern observed in the total pressure contour at time instance 2, the breakdown of the large low-pressure region at time instance 1 seems to be affecting the flow downstream the upper hydrofoil surface at time instance 2. Flow moves in the direction of negative pressure gradients, and as the large low-pressure region at time instance 1 grows, the flow at the upper hydrofoil surface may be slowed down as it is "attracted" to the low-pressure region. Once this region breaks down; it seems to exert a pressure pulse affecting the flow at the hydrofoil surface such that a wavy flow pattern is seen close to the hydrofoil surface.

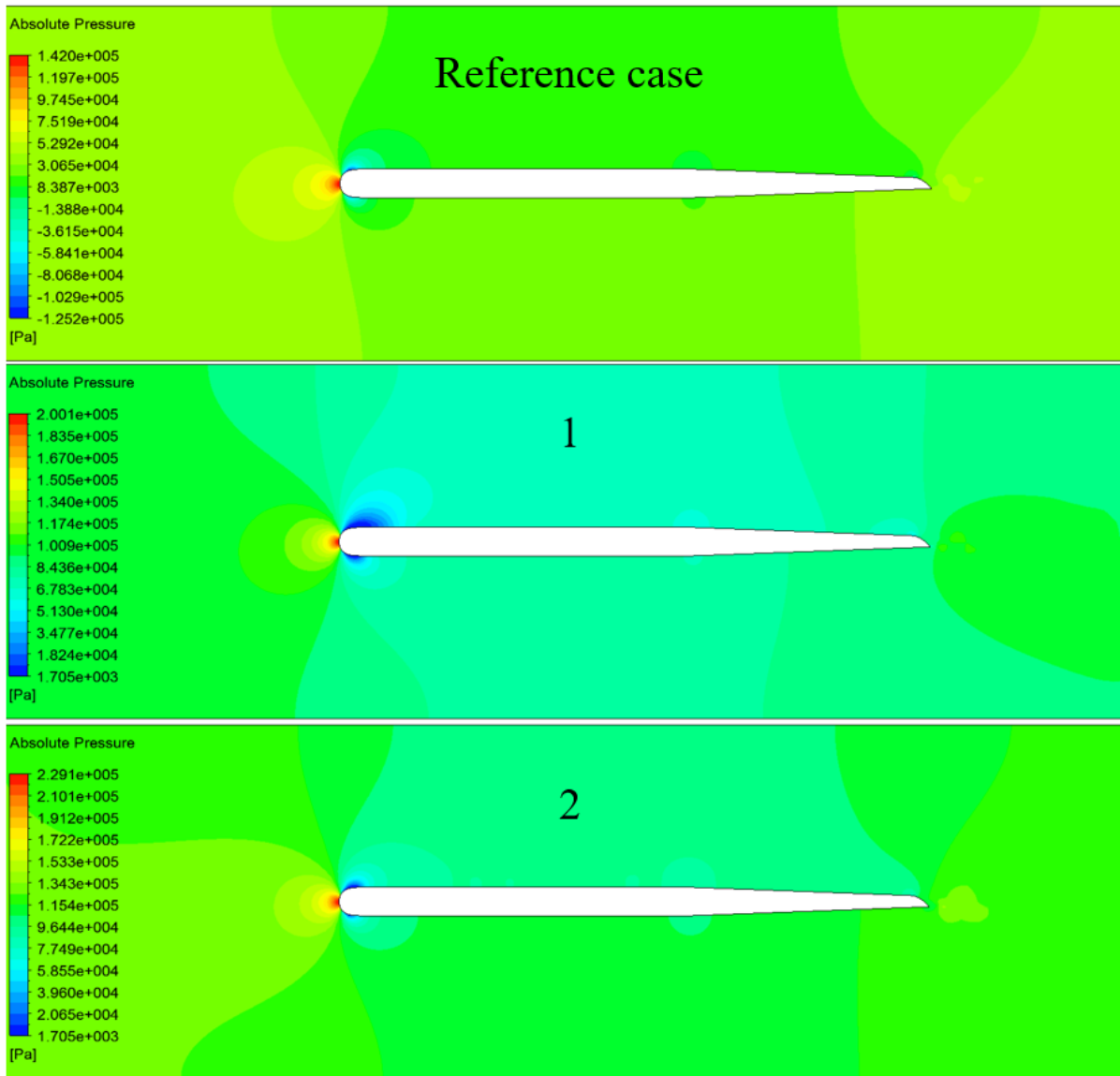


Figure 4.20: Absolute pressure contour, from top to bottom, without cavitation model, with cavitation model at time instance 1, with cavitation model at time instance 2. All at a velocity of 14 m/s.

### 4.3 General Discussions

This section presents some general considerations on the numerical setup used for the fluid flow investigations.

First of all, the 2D computational domain is not directly comparable to the flow observed during the experimental observations in the cascade test rig. The symmetry boundary condition set at the left and right wall is disregarding the actual left and right wall of the cascade test rig. The flow close to the walls is prone to produce secondary flows which may affect the main flow.

One consequence of the choice of the 2D domain was that the cross-sectional area on top and bottom of the hydrofoil was increased as the fillets between the hydrofoil and the walls were not present. The increased cross-sectional area will lead to a lower flow velocity, which is believed to slightly lower the observed vortex shedding frequency.

Another consequence of the chosen 2D domain is that turbulence, which is a highly three-dimensional phenomenon, is modelled in a very simplified way. The flow velocities investigated in this thesis are all forcing turbulent flow conditions. The exact effect of neglecting the three-dimensional component of the velocity during turbulent flow conditions is hard to foresee. Still, as the fillets between the hydrofoil and the walls is shaped in a way that leads flow closer to the centre of the pipe, it is assumed that this component of the velocity is slightly affecting the flow conditions.

Regarding the mesh independence study presented in the previous chapter, this was not performed with the final numerical setup. Optimally, the mesh independence study should have been performed with the adjusted mesh, the SST-SAS turbulence model and at the new time step. However, the relative difference between results obtained for different hydrofoil designs is not considered to be significantly affected by the numerical setup.

It is important to note that the mesh used for all studies was optimised for the original hydrofoil, which in practice means that the mesh used for all other studies are different. For the constant thickness hydrofoil, which occupies more of the space in the test section, the mesh is denser, and a higher accuracy might have been achieved. For the proposed new hydrofoil design the opposite is the case, a less dense mesh was used, and the accuracy of the results might not have been as good as for the investigations performed on the original hydrofoil design.

The difference between the results obtained from the SST and SST-SAS turbulence model was small. Some time could be reduced by using the SST model for the final numerical setup. However, the difference between the models could have been seen to be higher if they were compared at the final time step.

A way to improve the efficiency of the design procedure for the design of a new hydrofoil would be to only run the constant thickness hydrofoil tests at two or three different flow velocities. This should have been sufficient to find the optimal trailing edge. Still, if the tests were not done over such a large flow velocity range, it might not have been revealed that the vortex shedding frequency was highly influenced by the first spacing, and hence  $y^+$ , at the hydrofoil surface.

The blocking strategy of the mesh could also have been changed. The used blocking strategy is both giving high aspect ratios for many of the cells in the domain, and is unnecessary leading to the same mesh density all the way from the leading and trailing edge to the inlet and outlet of the computational domain respectively. A domain length study could also help to reduce the number of nodes. The 5 meter increase of the pipe length

upstream and downstream the cascade test rig is believed to be more than necessary.



## 5 Conclusions

This thesis has presented the theoretical background and a summary of previous work on the flow past hydrofoils, which substantiate the problems investigated and the methods used to address these problems. The objectives of this thesis was to move the lock-in condition for an existing experimental setup, the cascade test rig at NTNU, by designing a new hydrofoil, and investigate the occurrence of cavitation in the test rig.

The proposed new hydrofoil design has a new trailing edge, and the chamfer point is moved 100 mm towards the leading edge. The trailing edge angle is changed from 45 to 30 degrees, and the rounding of the edge is increased from two to four times the thickness.

By comparing the performance of the original and new hydrofoil design, the following conclusions are made:

- The vortex shedding frequency of the new hydrofoil is increased by 36.7 Hz at a flow velocity of 10 m/s compared to the original hydrofoil.
- The vortex shedding amplitude of the new hydrofoil is approximately a tenth of the original hydrofoil.
- The natural frequency is decreased by 151.81 Hz by moving the chamfer point.
- The new lock-in point is expected to be moved from 11 m/s to 7.87 m/s, and the lock-in velocity range is expected to be decreased as of the decreased vortex shedding amplitude.

The comparison of the two hydrofoil designs revealed that:

- The wake of the new hydrofoil is similar to the original hydrofoil but slightly narrower and elongated which indicates that the separated shear layers are closer together, leading to a small increase in the vortex shedding frequency.
- The "bump" seen in the velocity field at a point close to hydrofoil surface at the trailing edge, might be due to a vortex structure forcing the flow to move closer to the body.
- The lowest pressure region in the fluid domain was largest for the new hydrofoil, making it more susceptible to cavitate.

By using the Rayleigh-Plesset cavitation model, the occurrence of cavitation in the existing cascade test rig was investigated. The results showed the following:

- Low-pressure zones were located at the bottom and top of the leading edge and at the chamfer point of the hydrofoil. These low-pressure zones made the flow close to the hydrofoil surface prone to cavitate.
- The investigations with the cavitation model showed the presence of water vapour on top and bottom of the leading edge of the hydrofoil.
- The volume fraction of water vapour in the fluid domain varied periodically with a frequency of 35.13 Hz at a flow velocity of 13.5 m/s. This was close to that obtained in experimental observations at 14 m/s.
- The vortex shedding frequency was observed to decrease by 1.39 % under the cavitating conditions at a flow velocity of 14 m/s.
- The varying amount of water vapour in the domain corresponded well to the size of the low-pressure zone located on top of the leading edge of the hydrofoil.
- The breakdown of the low-pressure zone seemed to cause disturbances which lead to a wavy flow pattern on top of the hydrofoil surface.

## 6 Further Work

Further investigations on the proposed hydrofoil design and the occurrence of cavitation in the original cascade test rig is suggested.

A one-way and a two-way FSI analysis with coupling between the fluid and mechanical fields at and close to the lock-in condition would provide highly interesting results for investigations on both the original and new hydrofoil design. Knowledge in how fluid flow subject to a vibrating structure is affected by the motion of the body may be increased. This was at the beginning of this work intended done in the form of a blade flutter analysis. However, as the natural frequency and vortex shedding frequency obtained in the numerical investigations done in this thesis were far apart, the results from a blade flutter analysis would not be physically comparable to the results obtained in the experiment.

As the proposed hydrofoil design is thinner, a structural analysis where the hydrofoil is subject to fluid pressure should be performed on the new design to investigate possible fatigue leading to crack formation on the hydrofoil. The modal analysis could also be performed with applied pressure forces from CFD, where the pressure is varied based on different flow velocities. That would provide information on how the natural frequency changes subject to the pressure forces from the fluid flow.

Regarding the new proposed design, this should also be tested experimentally to identify the correct new lock-in velocities. The experimental setup may also be improved by for example measure the pressure at the hydrofoil surface. A pitot probe placed downstream the trailing edge may identify the vortex shedding frequency present in the numerical investigations for all flow velocities in the experiment as well. To get an even better reference for future numerical considerations, a Particle Image Velocimeter will also provide better knowledge of the flow field around the hydrofoil.

The final design proposed in this thesis was shown to be more prone to cavitate than the original design. The leading edge of the hydrofoil could be redesigned to achieve higher pressures where the low-pressure zones are today. An oval shaped leading edge is assumed to reduce the low-pressure zones significantly. Further investigations on trailing edge profiles could also be done. If more time were available creative trailing edge designs could provide interesting results. Air injection and suction chambers on the hydrofoil could also manipulate the vortex shedding frequency. Other design considerations is to change the transverse design of the hydrofoil.

Regarding cavitation in the original cascade test rig, a more extensive research at different pressure levels and velocities could reveal interesting patterns in how the vortex shedding frequency is influenced by these parameters. The proposed design could also be investigated subject to cavitating conditions to identify how the geometrical changes affect the flow under such conditions. A blade flutter analysis with cavitation is also a suggestion for further studies that may prove highly interesting results.

Regarding what flow instabilities is causing the water vapour content to vary with a frequency close to 30 Hz at the investigated flow velocity, this is still unknown. Further work, both numerically and experimentally, is suggested to find the cause of this phenomena.

Another consideration that could be made is to investigate a cascade test rig with two or three hydrofoils. This may provide interesting results on how the blades in High-Head Francis Turbines interacts with each other subject to vibration and cavitation.

In the field of flow-induced vibration in hydraulic machinery, many other paths than the ones presented in this chapter exist. As presented early in this thesis, credible estimation of hydrodynamic damping during variable operating conditions are still to be fully understood, and further research in this field is important to increase knowledge necessary to secure reliable energy systems in the future.

# Bibliography

- [1] Statistisk Sentralbyrå. Elektrisitet 2015. <https://www.ssb.no/energi-og-industri/statistikker/elektrisitet/aar>. [Online; accessed 14-December-2016].
- [2] Nancy Kroner, Roger Bérubé, BN Kroner, et al. Maintaining power grid reliability through individual unit stability. *Hydro Vision*, pages 1–10, 2008.
- [3] Chirag Trivedi and Michel J Cervantes. Fluid-structure interactions in francis turbines: A perspective review. *Renewable and Sustainable Energy Reviews*, 68:87–101, 2017.
- [4] Peter Dörfler, Mirjam Sick, and André Coutu. *Flow-Induced Pulsation and Vibration in Hydroelectric Machinery: Engineer’s Guidebook for Planning, Design and Troubleshooting*. Springer Science & Business Media, 2012.
- [5] André Coutu, Michel D Roy, Christine Monette, and Bernd Nennemann. Experience with rotor-stator interactions in high head francis runner. In *Proceedings of 24th IAHR symposium on hydraulic machinery and systems at Foz do Iguassu, Brazil*, 2008.
- [6] Andre Coutu, D Proulx, S Coulson, and A Demers. Dynamic assessment of hydraulic turbines. *Proceedings of Hydro Vision*, pages 16–20, 2004.
- [7] Chirag Trivedi. A review on fluid structure interaction in hydraulic turbines: A focus on hydrodynamic damping. *Engineering Failure Analysis*, 2017.
- [8] Chirag Trivedi. *Investigations of Transient Pressure Loading on a High Head Francis Turbine*. PhD thesis, Luleå tekniska universitet, 2015.
- [9] Jarle Vikør Ekanger. Master thesis: Morphing skins to improve local flow behavior in a hydroturbine context, 2011.
- [10] Arne Kjølle. Mechanical equipment. *Waterpower laboratory, NTNU*, 2001.
- [11] Alireza Zobeiri. Investigations of time dependent flow phenomena in a turbine and a pump-turbine of francis type. 2009.
- [12] Amirreza Zobeiri. Effect of hydrofoil trailing edge geometry on the wake dynamics. 2012.
- [13] Hermann Schlichting. *Boundary-layer theory*. 1968.

- [14] JH Gerrard. The mechanics of the formation region of vortices behind bluff bodies. *Journal of Fluid Mechanics*, 25(02):401–413, 1966.
- [15] Anatol Roshko. On the development of turbulent wakes from vortex streets. 1954.
- [16] John H Lienhard. *Synopsis of lift, drag, and vortex frequency data for rigid circular cylinders*, volume 300. Technical Extension Service, Washington State University, 1966.
- [17] Vivianne Holmén. Methods for vortex identification. *Master’s Theses in Mathematical Sciences*, 2012.
- [18] Jinhee Jeong and Fazle Hussain. On the identification of a vortex. *Journal of fluid mechanics*, 285:69–94, 1995.
- [19] C A Gongwer. A study of vanes singing in the water. 1952.
- [20] RM Donaldson. Hydraulic turbine runner vibration. *ASME J. Eng. Power*, 78:1141–1147, 1956.
- [21] D R Heskestad, Gunnar Olberst. Influence of trailing-edge geometry on hydraulic-turbine-blade vibration resulting from vortex excitation. 1960.
- [22] Torbjørn K Antonsen, Øyvind Nielsen. Cfd simulation of von karman vortex shedding. 2004.
- [23] H Brekke. A review on oscillatory problems in francis turbines and simulation of unsteady flow in conduit systems. In *Proceedings of the 17th IAHR Symposium, Beijing, China*, pages 15–19, 1994.
- [24] Zhifeng Yao, Fujun Wang, Matthieu Dreyer, and Mohamed Farhat. Effect of trailing edge shape on hydrodynamic damping for a hydrofoil. *Journal of Fluids and Structures*, 51:189–198, 2014.
- [25] Xin Liu, Lingjiu Zhou, Xavier Escaler, Zhengwei Wang, Yongyao Luo, and Oscar De La Torre. Numerical simulation of added mass effects on a hydrofoil in cavitating flow using acoustic fsi. *Journal of Fluids Engineering*, 2016.
- [26] Charles Seeley, André Coutu, Christine Monette, Bernd Nennemann, and Hugues Marmont. Characterization of hydrofoil damping due to fluid–structure interaction using piezocomposite actuators. *Smart Materials and Structures*, 21(3), 2012.
- [27] Philippe Ausoni, Mohamed Farhat, Youcef Ait Bouziad, Jean-Louis Kueny, and François Avellan. Kármán vortex shedding in the wake of a 2d hydrofoil: Measurement and numerical simulation. In *IAHR Int. Meeting of WG on Cavitation and Dynamic Problems in Hydraulic Machinery and Systems*, number LMH-CONF-2006-002, 2006.
- [28] Philippe Ausoni, Amirreza Zobeiri, François Avellan, and Mohamed Farhat. The effects of a tripped turbulent boundary layer on vortex shedding from a blunt trailing edge hydrofoil. *Journal of Fluids Engineering*, 134(5):051207, 2012.

- [29] Philippe Ausoni, Mohamed Farhat, and François Avellan. Hydrofoil roughness effects on von karman vortex shedding. In *2nd IAHR International Meeting of the Workgroup on Cavitation and Dynamic Problems in Hydraulic Machinery and Systems*, number LMH-CONF-2007-011, 2007.
- [30] Amirreza Zobeiri, P Ausoni, F Avellan, and M Farhat. How oblique trailing edge of a hydrofoil reduces the vortex-induced vibration. *Journal of fluids and structures*, 32:78–89, 2012.
- [31] Philippe Ausoni, Mohamed Farhat, Xavier Escaler, Eduard Egusquiza, and François Avellan. Cavitation influence on von kármán vortex shedding and induced hydrofoil vibrations. *Journal of fluids engineering*, 129(8):966–973, 2007.
- [32] O De La Torre, X Escaler, E Egusquiza, and Mohamed Farhat. Experimental investigation of added mass effects on a hydrofoil under cavitation conditions. *Journal of Fluids and Structures*, 39:173–187, 2013.
- [33] Antoine Ducoin, Jacques André Astolfi, François Deniset, and Jean-François Sigrist. Computational and experimental investigation of flow over a transient pitching hydrofoil. *European Journal of Mechanics-B/Fluids*, 28(6):728–743, 2009.
- [34] Cécile Münch, Philippe Ausoni, Olivier Braun, Mohamed Farhat, and Francois Avellan. Fluid–structure coupling for an oscillating hydrofoil. *Journal of Fluids and Structures*, 26(6):1018–1033, 2010.
- [35] Peter W Bearman. Vortex shedding from oscillating bluff bodies. *Annual review of fluid mechanics*, 16(1):195–222, 1984.
- [36] B. Mutlu Sumer. *Lecture Notes on Turbulence: Revised/Updated 2007*. 2007.
- [37] David C Wilcox. Multiscale model for turbulent flows. *AIAA journal*, 26(11):1311–1320, 1988.
- [38] CFX Ansys. Ansys cfx-solver theory guide. *ANSYS CFX Release*.
- [39] Florian R Menter. Two-equation eddy-viscosity turbulence models for engineering applications. *AIAA journal*, 32(8):1598–1605, 1994.
- [40] Su-Jong Yoon, Yun-Je Cho, Kwang-Yong Kim, Min-Hwan Kim, Won-Jae Lee, and Goon-Cherl Park. Experimental evaluation of the bypass flow in the vhtr core. *Transactions of SMiRT*, 19:12–17, 2007.
- [41] Florian R Menter. Review of the shear-stress transport turbulence model experience from an industrial perspective. *International Journal of Computational Fluid Dynamics*, 23(4):305–316, 2009.
- [42] Frank M White. *Fluid Mechanics*, volume 7. McGraw-Hill New York, 2011.
- [43] Xavier Escaler, Jarle V Ekanger, Håkon H Francke, Morten Kjeldsen, and Torbjørn K Nielsen. Detection of draft tube surge and erosive blade cavitation in a full-scale francis turbine. *Journal of Fluids Engineering*, 137(1):011103, 2015.

- [44] Lord Rayleigh. Viii. on the pressure developed in a liquid during the collapse of a spherical cavity. *The London, Edinburgh, and Dublin Philosophical Magazine and Journal of Science*, 34(200):94–98, 1917.
- [45] Milton S Plesset and Andrea Prosperetti. Bubble dynamics and cavitation. *Annual review of fluid mechanics*, 9(1):145–185, 1977.
- [46] F Bakir, R Rey, AG Gerber, T Belamri, and B Hutchinson. Numerical and experimental investigations of the cavitating behavior of an inducer. *International Journal of Rotating Machinery*, 10(1):15–25, 2004.
- [47] John D Robson, Colin J Dodds, Donald B Macvean, and Vincent R Paling. Vibration theory i: Receptance. In *Random Vibrations*, pages 35–44. Springer, 1971.
- [48] Mike Mui Bank Ting. Master thesis: Study of vortex shedding from a vibrating hydrofoil. 2017.
- [49] Antoine Ducoin and Yin L Young. Hydroelastic response and stability of a hydrofoil in viscous flow. *Journal of fluids and structures*, 38:40–57, 2013.
- [50] Rupak Biswas and Roger C Strawn. Tetrahedral and hexahedral mesh adaptation for cfd problems. *Applied Numerical Mathematics*, 26(1-2):135–151, 1998.
- [51] ICEM CFD ANSYS. 11.0 help manual. *ANSYS Inc*, 2009.
- [52] CFX ANSYS. Reference guide. *Release*, 2013.
- [53] Mathworks. fft. <https://se.mathworks.com/help/matlab/ref/fft.html>. [Online; accessed 13-December-2016].
- [54] Arden L Buck. New equations for computing vapor pressure and enhancement factor. *Journal of applied meteorology*, 20(12):1527–1532, 1981.
- [55] Carlos Guedes Soares and Wolfgang Fricke. *Advances in marine structures*, 2013.
- [56] Pressure loss from fittings – excess head (k) method. [https://neutrium.net/fluid\\_flow/pressure-loss-from-fittings-excess-head-k-method/](https://neutrium.net/fluid_flow/pressure-loss-from-fittings-excess-head-k-method/).



# Appendices

## Appendix A: Pressure Loss Calculation

As presented in section 3.2.8, the pressure levels in the cascade test rig was not measured during the experimental observations of cavitation. To imitate the experimental observation as closely as possible, the pressure loss from the pressure tank to the inlet of the computational domain was estimated. The pressure loss across the computational domain was obtained in a CFD analysis at the investigated flow velocity.

The estimation of the pressure loss from the pressure tank to the inlet of the computational domain is done by using the Bernoulli equation with frictional losses from tees and bends. Figure 6.1 shows the piping system from the pressure tank to the start of the computational domain at point 3. The absolute pressure at point 1, where the water is still, is the only known pressure. Two equations are therefore needed in order to find the pressure at point 3. These two equations are given as equations 6.1 and 6.2. Note that all pressures in these equations are gage pressures.

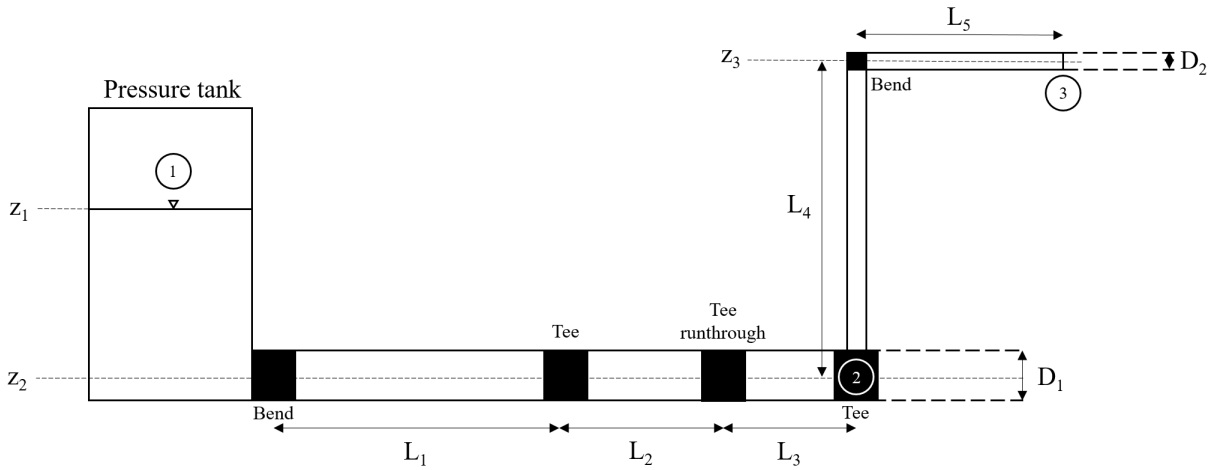


Figure 6.1: Pressure tank and piping system upstream numerical domain of the cascade test rig.

$$\frac{p_1}{\rho g} + \frac{V_1^2}{2g} + z_1 = \frac{p_2}{\rho g} + \frac{V_2^2}{2g} + z_2 + \frac{V_2^2}{2g} \left( \frac{f(L_1 + L_2 + L_3)}{D_1} + K_{bend} + 2K_{tee} + K_{tee\ run} \right) \quad (6.1)$$

$$\frac{p_2}{\rho g} + \frac{V_2^2}{2g} + z_2 = \frac{p_3}{\rho g} + \frac{V_3^2}{2g} + z_3 + \frac{V_3^2}{2g} \left( \frac{f(L_4 + L_5)}{D_2} + K_{bend} \right) \quad (6.2)$$

Table 6.1 presents the data needed to find the pressure at point 3. With these input parameters the gage static pressure at point 3 was found to be 81.140 kPa.

A steady state CFD analysis at 14 m/s with 1 atmosphere reference pressure and 0 atmosphere outlet static pressure revealed that the average inlet pressure at the inlet boundary and average outlet pressure at the outlet boundary was 16 141 Pa and 7 Pa

respectively, leading to an additional pressure loss of 16 133 Pa. Hence, the total gage static pressure loss from the pressure tank to the outlet of the computational domain was 65 007 Pa.

Quantity	Symbol	Unit	Value
Static gage pressure in pressure tank	$p_1$	bar	1
Flow rate	$Q$	$m^3/s$	0.315
Diameter of pipes with length $L_1$ , $L_2$ and $L_3$	$D_1$	$m$	0.6112
Diameter of pipes with length $L_4$ and $L_5$	$D_2$	$m$	0.3
Velocity at point 1	$V_1$	$m/s$	0
Velocity at point 2	$V_2$	$m/s$	1.0738
Velocity at point 3	$V_3$	$m/s$	4.4563
Relative elevation (to point 2) at point 1	$z_1$	$m$	2.2
Relative elevation (to point 2) at point 2	$z_2$	$m$	0
Relative elevation (to point 2) at point 3	$z_3$	$m$	2.45
Length of pipe section 1	$L_1$	$m$	2.9
Length of pipe section 2	$L_2$	$m$	1.35
Length of pipe section 3	$L_3$	$m$	0.75
Length of pipe section 4	$L_4$	$m$	2.37
Length of pipe section 5	$L_5$	$m$	1.4
Friction factor	$f$	-	0.015
Loss coefficient bend*	$K_{bend}$	-	0.3
Loss coefficient tee**	$K_{tee}$	-	1
Loss coefficient runthrough tee**	$K_{tee\ run}$	-	0.4

Table 6.1: Input data pressure loss calculation.

\* Adapted from [42]

\*\* Adapted from [56]

## Appendix B: Modal Analysis Mesh Independence

The modal analyses was performed in order to predict the natural frequency of the new proposed hydrofoil design with a moved chamfer point. As described in section 3.3, some parts of the square test section was included in the model in addition to water, which was modelled as an acoustic body. Figure 6.2 shows a cross-section of the final mesh used in the modal analysis of the new hydrofoil design. The mesh has 531 280 nodal points. The final mesh used for the original hydrofoil had 328 924 nodal points.

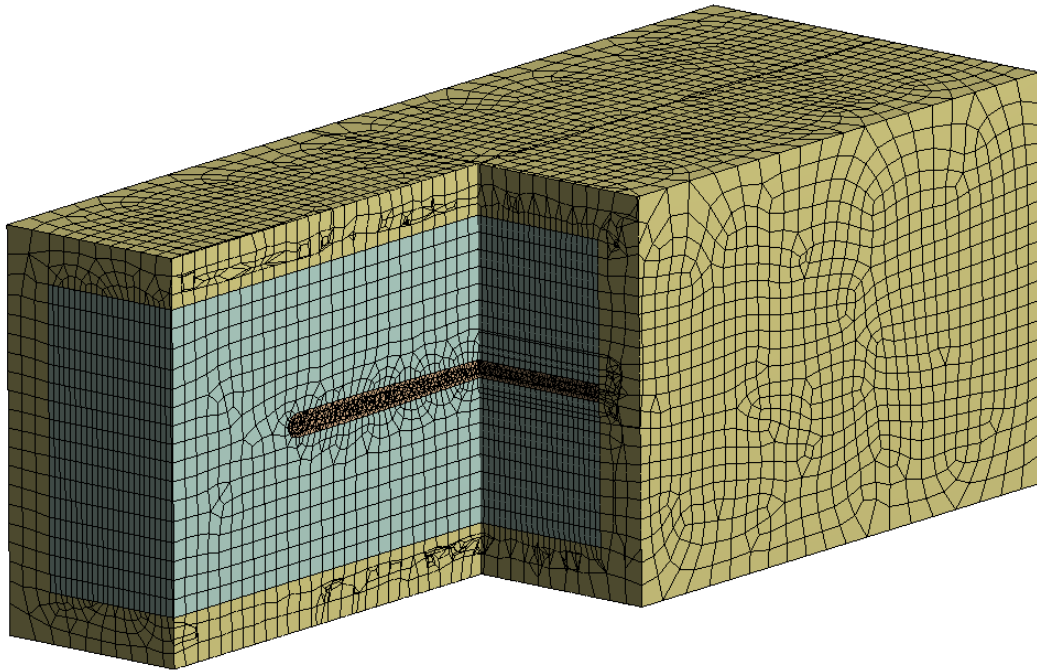


Figure 6.2: Mesh used for the modal analysis of the new hydrofoil design.

The mesh used for mechanical analyses is less sensitive than meshes used in CFD. Still a mesh independence study with respect to the first mode of the two different designs was done. The result from this study is presented in Figure 6.3. As can be seen the converged natural frequency of the original and new design was found to be 681.37 Hz and 529.56 Hz respectively.

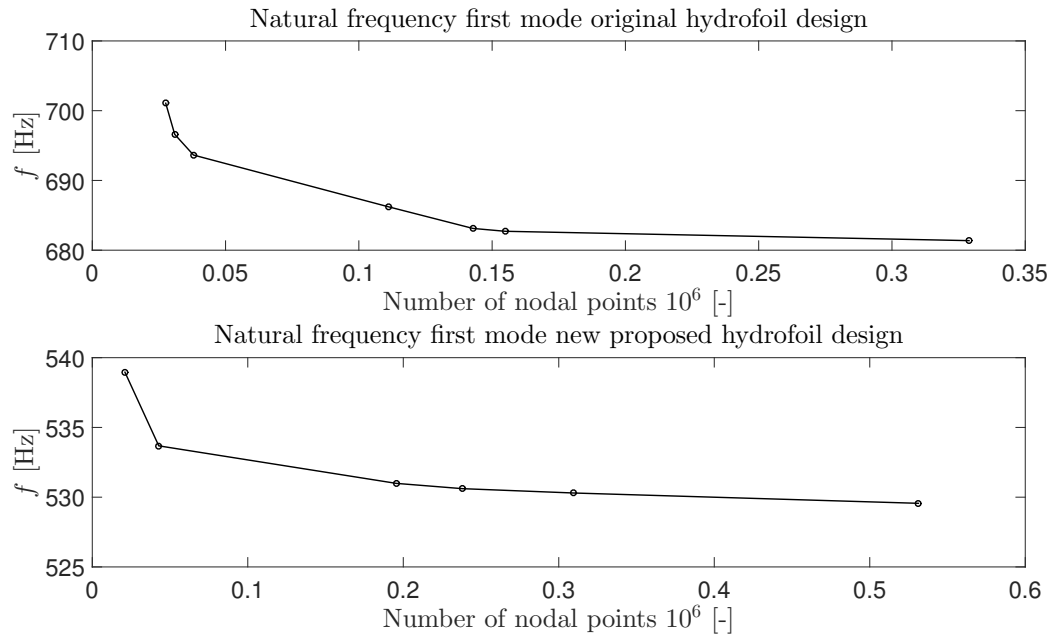


Figure 6.3: Results from modal analysis mesh independence test.

Appendix C: Paper Submitted to the  
*International symposium on  
Current Research in Hydraulic Turbines (CHRT-VII)*

## **Numerical Investigation of Flow Field subject to Vibrating structure**

**Sondre Leonhardsen<sup>1\*</sup>, Chirag Trivedi<sup>1</sup>, Ole Gunnar Dahlhaug<sup>1</sup>**

<sup>1</sup>*Department of Energy and Process Engineering, Norwegian University of Science and Technology, Høgskoleringen 1, 7491 Trondheim, Norway*

*\* Corresponding author ([sondrle@stud.ntnu.no](mailto:sondrle@stud.ntnu.no))*

---

### **Abstract**

Hydraulic turbines are subject to both high-cycle and low-cycle fatigue during power generation. Currently, the key challenge is the credible estimation of the added mass, natural frequencies and hydrodynamic damping. The natural frequency is dependent on the flow conditions in the turbine. It is difficult to estimate the vibration characteristics for prototypes due to involved complexities in the design phase. To understand the flow physics and associated mechanical characteristics of the turbine blade, a hydrofoil test rig was developed at the Waterpower laboratory at NTNU. Measurements were conducted at different flow conditions. Strong vibrations were experienced during the lock-in condition. The lock-in condition is within the range of flow velocities that generally exist in prototype turbines. The operational range of the test rig is average inlet velocities between 0 and 40 m/s, and the lock-in phenomena was present at velocities between 10 and 12 m/s with the original hydrofoil.

The main objective of the current study is to investigate the lock-in frequency with respect to different trailing edge profiles. The original hydrofoil with available measurement data was selected to validate the numerical model. Then, the modified trailing edge profiles were used to push the lock-in condition to a lower flow rate (velocity). By changing the trailing edge profile, it is expected that the lock-in condition may be pushed down by approximately 22 %.

**Keywords:** Hydropower, High head Francis turbines, Flow induced vibration, Lock-in, CFD

---

### **1. Introduction**

An increased amount of intermittent energy sources in addition to rapid introduction of new technologies lead to more instability in the electric grid. In Norway, a country where over 95 % of the electric power generation comes from hydropower, hydropower plants contribute to stabilize the electric grid because of its regulative benefits. This forces hydropower plants to run at off-design conditions frequently. Frequent start and stops may lead to excessive vibrations causing unwanted fluid behavior, which again may cause stress, fatigue and premature cracks on runner blades [6]. Especially the blades of high head Francis turbines have been subjected to such phenomena recent years. Resonance occur when the frequencies of pressure oscillations coincide with the natural frequencies of mechanical equipment, and may lead to severe damage. The main questions unanswered within this topic are how to estimate the hydrodynamic dampening when a turbine is subject to resonance conditions, and how the added mass effect changes the vibration characteristics [7].

When a vibrating structure is surrounded by a viscous fluid, it experiences a reacting force. The force may be interpreted as an added mass and hydrodynamic damping which is dependent on the local flow condition. A hydraulic turbine is a complex structure that includes both rotating and stationary components. The runner is an important component which is surrounded by the stationary vanes and the labyrinth seal. While designing the runner, a certain amount of added mass and dampening effect is assumed. This is based on decade old empirical relations and the experience from the past design parameters. However, such

approximations is no longer trustable following the current trend of turbine operation and related damages. To make safe designs, which can cope with the current electricity demand, estimation of hydrodynamic damping is important as the turbine efficiency is significantly reduced when the turbine is damaged. Some efforts have been made to investigate the damping and how damping can be useful during resonance in the recent years. The reviewed literature indicates that the hydrodynamic damping can be an important parameter to reduce the vibration amplitudes [8, 9, 10, 11, 12].

At the Waterpower Laboratory at NTNU, an experimental rig consisting of a hydrofoil mounted in a pipe with 150x150 mm cross-section, is set up to investigate vibration characteristics in hydropower plants. The hydrofoil test setup provides information of basic mechanism between the fluid flow and the structure under different flow conditions. Moreover, this setup provides flexibility of controlling different parameters such as vibration level, wide range of frequency control, flow rate and the material.

### 1.1. Problem statement and objectives

In the current Cascade rig at the Waterpower Laboratory at NTNU the appearance of the lock-in effect in the operational range causes issues because of its presence in the middle of the operational range. The lock-in effect was present in a velocity range between 10 and 12 m/s. The first natural frequency of the system is approximately at 680 Hz, meaning that the vortex shedding frequency at these velocities are at a similar frequency. The appearance of the lock-in effect complicates the study of vibrational characteristics in hydraulic turbines, which is the purpose of the Cascade rig. At velocities, around 27 m/s, the flow cavitates because the testing facilities do not allow further increases in inlet pressure.

The objective of the study presented in this paper is to design a hydrofoil where the lock-in effect is present at a lower flow rate than in the current test rig. Previous studies have shown that for hydraulic turbines, which the cascade rig is analogous to, the natural frequency of the runner is normally lower than the shedding frequency close to the best efficiency point [1]. The new proposed design of the hydrofoil may either increase the shedding frequency, lower the natural frequency or utilize the effect from a combination of both. The original hydrofoil design and test section dimensions are optimized according to the operational range and the testing facilities, hence the length of the hydrofoil and the pipe dimensions are to be kept the same.

## 2. Experimental and numerical setup

### 2.1. Experimental setup

The test section, as presented in Fig. 1, consists of a circular inlet diffuser converging into a square pipe where the hydrofoil is mounted. In the square test section, there are several pressure transducers and two plexiglas windows. The outlet diffuser eventually forms into a circular pipe. The operational range of average velocities at the inlet of the square test section for the Cascade rig is from 0 to 40 m/s.

The inner and outer dimensions of the square test section are  $\text{\O}150$  mm and  $\text{\O}200$  mm respectively. The hydrofoil has a length of 250 mm from leading to trailing edge, and a thickness of 12 mm. Fig. 1b shows the original hydrofoil part, which is entirely made of aluminum. The original hydrofoil has a chamfer point at a position 150 mm from the leading edge, which can be seen in Fig. 1d. The thickness at the end of the hydrofoil, the trailing edge (TE), is 4.5 mm. The hydrofoil part consists of two different sized plates with the hydrofoil connected in between by rounded off fillets. Two piezoelectric (PZT) patches are placed on top and bottom of the hydrofoil, close to the trailing edge. These provides forced excitation and thereby vibration of the hydrofoil. The PZT patches measures the receptance (displacement), and can identify the natural frequencies of the system by applying forced excitation in a wide range of frequencies. Receptance is the ratio of displacement to the excited force in a vibration.



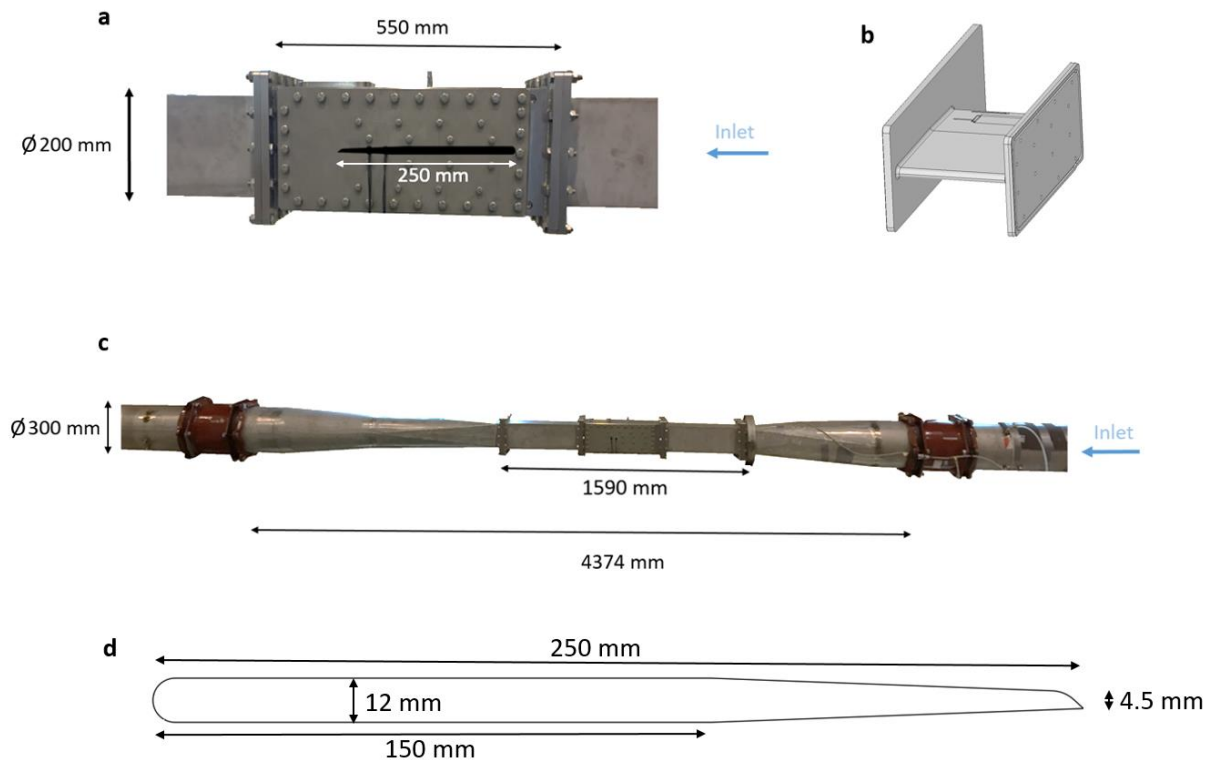


**Figure 1.** Experimental setup. (a) Square test section with hydrofoil position visualized as black, (b) original hydrofoil part, (c) full pipe arrangement with main dimensions and (d) original hydrofoil profile.

## 2.2. Computational domain

The results presented in this paper are from numerical investigations conducted on a two-dimensional hydrofoil. The 2D computational domain has the same dimensions as a cross section of the experimental setup, but is extended upstream and downstream of the hydrofoil to allow for proper boundary layer development. The upstream and downstream section have been extended by 5 meters each. This results in a computational domain being 26.81 chord lengths upstream the LE of the hydrofoil and 29.69 chord lengths downstream the TE of the hydrofoil. Similar setups and velocity ranges has proved this domain length to be sufficient [2].

## 2.3. Numerical setup and convergence

The mesh used for all simulations was generated using the software ICEM CFD. All mesh elements are hexahedral. The mesh has been developed in the following way

- Create initial mesh and achieve average  $y^+$  of 30 at the hydrofoil surface of the original design at a velocity of 40 m/s.
- Perform mesh independency test at a velocity of 40 m/s by doubling the amount of nodal points at all mesh edges until convergence of average pressure is achieved.

The mesh size and all edge parameters of the converged mesh developed for the original hydrofoil design will be used for all other designs as well.

Ansys CFX is used for the numerical simulations. The analyses have been performed with a time step of 0.00025 seconds (4000 Hz) with a total time of 2 seconds. The chosen turbulence model is the  $k-\omega$  Shear Stress Transport Turbulence (SST) model. The accuracy of the turbulence model is set to first order turbulence numerics. The SST model accounts for the transport of the turbulent shear stress and gives highly

accurate predictions of the onset and the amount of flow separation under adverse pressure gradients. The advection and transient schemes are set to high resolution and second order backward Euler respectively. The convergence criteria used in the simulations is  $10^{-5}$  RMS.

The inlet boundary condition is a mass flow, which corresponds to an average velocity at the inlet of the square test section varied between 0 and 40 m/s. The simulations have been performed with intervals of 5 m/. The reference and outlet pressure is set to 1 atm and 0 atm, respectively. The left and right walls are given the symmetry condition. The upper and lower walls are given the no-slip wall condition.

In order to investigate mesh convergence, several monitor points are placed in the numerical domain to monitor absolute pressure at different locations. Fig. 2 shows the position of the 81 monitor points used in the analyses. Mesh convergence of average absolute pressure at the points P26, P19, P28 and P323 are documented in the following section.

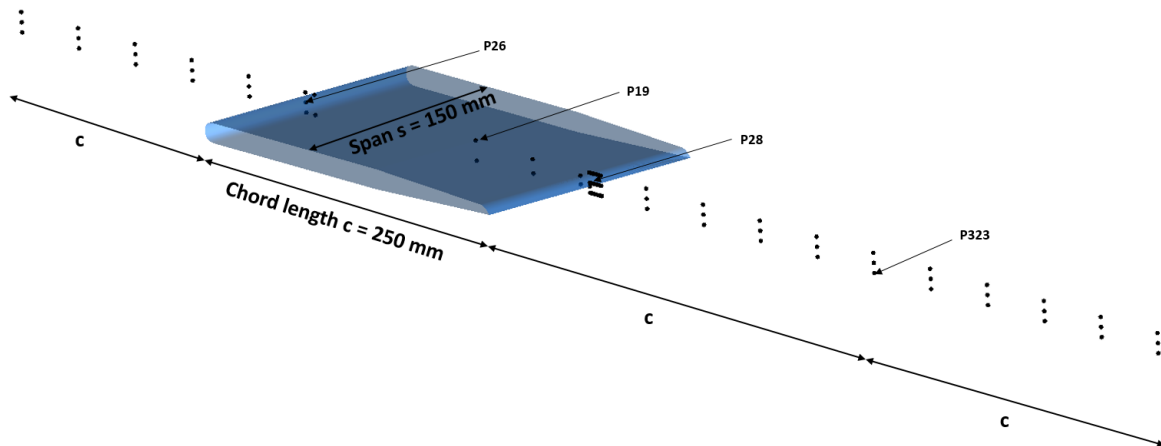


**Figure 2.** Illustration of 2D hydrofoil setup for the original hydrofoil design and the 81 monitor points. The points P26, P19, P28 and P323 is used in a mesh convergence test.

#### 2.4. Mesh convergence

The mesh for the original hydrofoil design is visualized in Fig. 5. For the studies on the three hydrofoils with constant thickness and different shaped TE, the same mesh size and mesh parameters will be used.

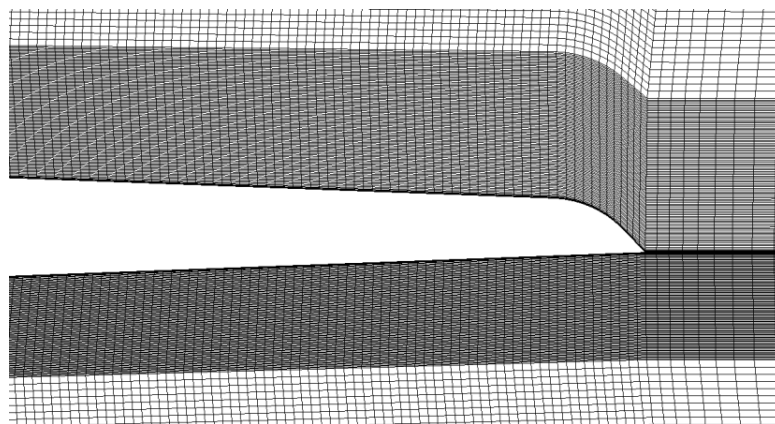


**Figure 5.** Mesh at trailing edge of original hydrofoil design.

The mesh convergence study showed convergence for the absolute pressure at the points P26, P19, P28 and P323, see Fig. 4. Based on the results from the convergence study, the mesh with 2 240 824 nodes was used for further studies. The average pressure at the thickest point and the LE is not fully converged at this amount of nodes, but as the difference is small, this mesh has been used for further studies.

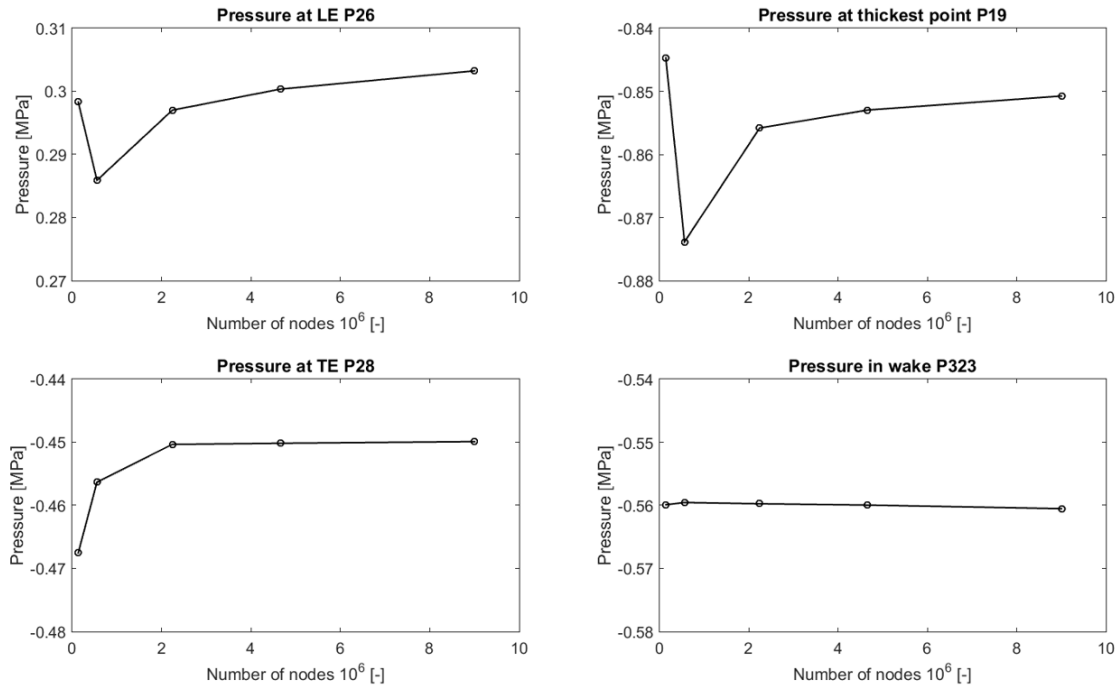


**Figure 4.** Results from the mesh convergence study of the original hydrofoil at a velocity of 40 m/s.

### 2.5. Trailing edge shapes

To propose a new hydrofoil design, the effect of trailing edge shape is isolated by studying three different trailing edges on a hydrofoil with a constant thickness of 12 mm. The leading edge is the same as in the original design. The original trailing edge design (Hydrofoil 1), a similar design with less curvature (Hydrofoil 2) and a symmetrical design (Hydrofoil 3) is studied. These designs are selected from [3]. The three profiles are shown in Fig.3. These hydrofoils will be studied in the entire operational velocity range from 0 to 40 m/s.



**Figure 3.** (a) Hydrofoil 1, (b) Hydrofoil 2, (c) Hydrofoil 3.

### 3. Results and discussion

#### 3.1. Original hydrofoil design

Fig. 7 shows the Fast Fourier Transform of the normalized pressure signal at monitor point P28 for the original hydrofoil design. The pressure is normalized according to the highest amplitude in the pressure signal at each flow rate. I.e. locally normalized, not globally. The frequency is increasing linearly until 15 m/s is reached. Beyond this the frequency is nearly constant until 30 m/s where the pressure signal is very noisy, leading to less distinguishable frequencies.

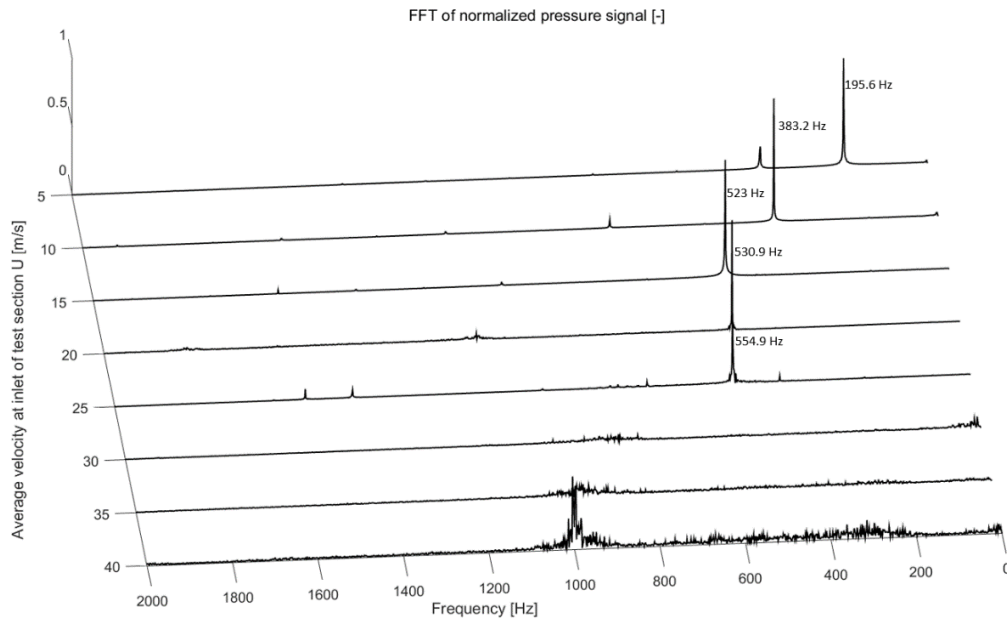


**Figure 6.** FFT of normalized pressure signal at monitor point P28 [-] for original hydrofoil design.

To better understand the physics of the flow and the frequencies of the pressure signal at the TE, iso-surfaces with the  $\lambda_2$ -criterion with velocity contours is visualized in Fig. 6. The  $\lambda_2$ -criterion correctly represent vortex cores [4]. The laminar separation bubbles seen in all three figures at the chamfer point and at the TE suggests that the flow separates due to the large curvature of the geometry and a large adverse pressure gradient forms in these areas.

By inspecting the flow at 5 and 20 m/s, the size of the vortices downstream the TE seem to decrease with an increase in flow rate. This suggest that the turbulent structures of the flow are smaller at higher flow rates. At 35 m/s the periodically shed off vortices no longer exists. A large vortex structure has formed behind the trailing edge. Compared to studies like [5], the result obtained at 35 m/s does not seem to model the turbulence correctly. There should have been an area at and downstream the TE with formation of small turbulent structures in a chaotic pattern. In order to obtain adequate results for higher flow rates for the original hydrofoil design, showing the turbulent structures of the flow, a 3D simulation may be required as turbulence is three-dimensional. The above mentioned study also utilizes DNS, which may be needed in order to predict turbulence accurately in the case investigated.

Another issue with the numerical model is that the same mesh is used for all simulations. This means that  $y^+$  varies with respect to the flow. At the lower flow rates  $y^+$  is close to 1 and at the higher flow rates it is closer to 30, as the mesh was designed for. When performing full 3D simulations on a final design later on, a constant  $y^+$  will be beneficial in order to reduce possible errors in the prediction of the vortex shedding frequencies.

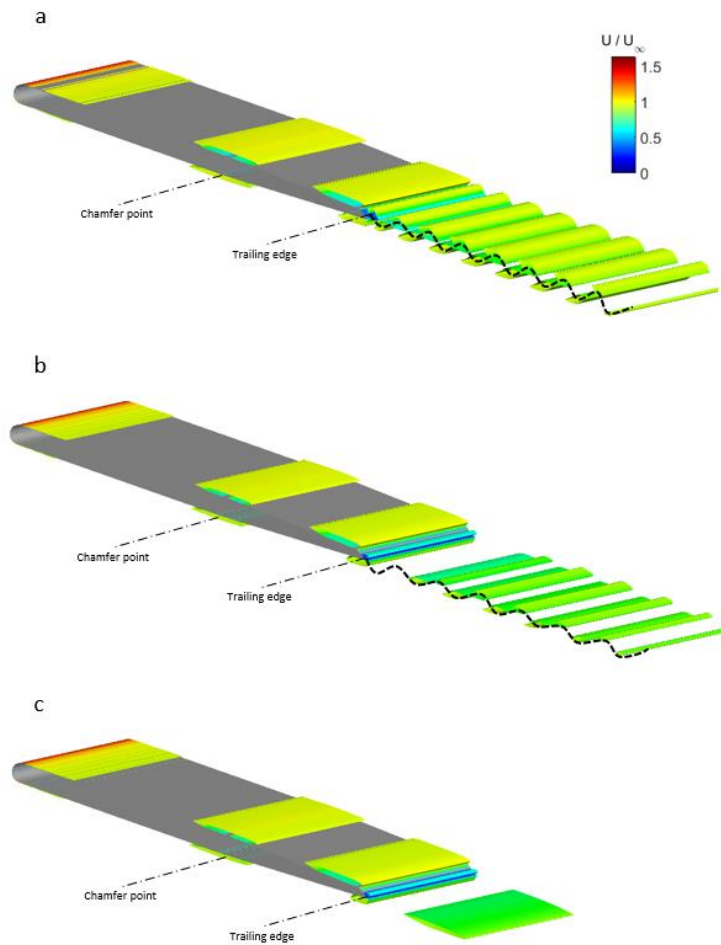


**Figure 7.** Iso-surfaces of  $\lambda_2$ -criterion at level 0.001 with velocity contours. (a) 5 m/s, (b) 20 m/s, (c) 35 m/s. Velocity range is normalized with respect to average velocity at the inlet of the square test section, being 5 m/s, 20 m/s and 35 m/s from top to bottom.

### 3.2. The effect of trailing edge shape

By studying the frequencies obtained from the simulations performed on Hydrofoil 1, as presented in Fig. 8, the frequencies seem to increase linearly until a velocity of 35 m/s. As for the original hydrofoil design, the result exerts an unphysical behavior for higher velocities. Previous studies, including [3], suggests that the vortex shedding frequency should increase for an increase in flow rate. When investigating the  $\lambda_2$ -criterion of the original hydrofoil design, the above-mentioned reasons may explain the rather unexpected result in this case as well. The less dominant frequencies marked out at 836.6 and 848.6 Hz for velocities 35 and 40 m/s respectively, would prove to be more reliable. If  $y^+$  were close to 1 for these simulations these frequencies may have been the dominant frequencies of the pressure signal.

Eq. 1, as found in [3], where  $f$  [Hz] is the shedding frequency,  $B$  [-] is a geometrical factor,  $t$  [mm] is the hydrofoil thickness, and  $c$  [m/s] is the velocity, states that the shedding frequency is inversely proportional to the thickness  $t$  and a constant. When comparing Fig. 7 and 8 this is seen to be the case. The original hydrofoil with chamfer has a lower thickness at the trailing edge.

$$f = 190 \frac{B}{100t + 0.56} \frac{c}{c} \quad (1)$$

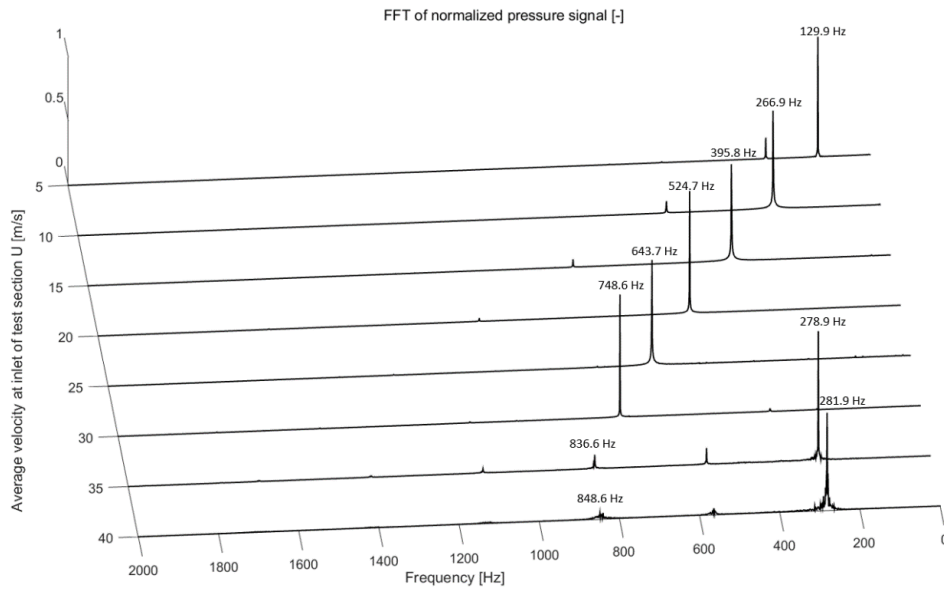


**Figure 8.** FFT of normalized pressure signal at monitor point P28 [-] for Hydrofoil 1.

By comparing Fig. 8 and 9 it is seen that Hydrofoil 2 has an increased shedding frequency at the TE for all flow rates. This, and the linear increase of shedding frequency for all flow rates, is in accordance with [3]. By comparing the shedding frequency at 10 m/s it is observed that Hydrofoil 3 has increased the shedding frequency by about 22 %.

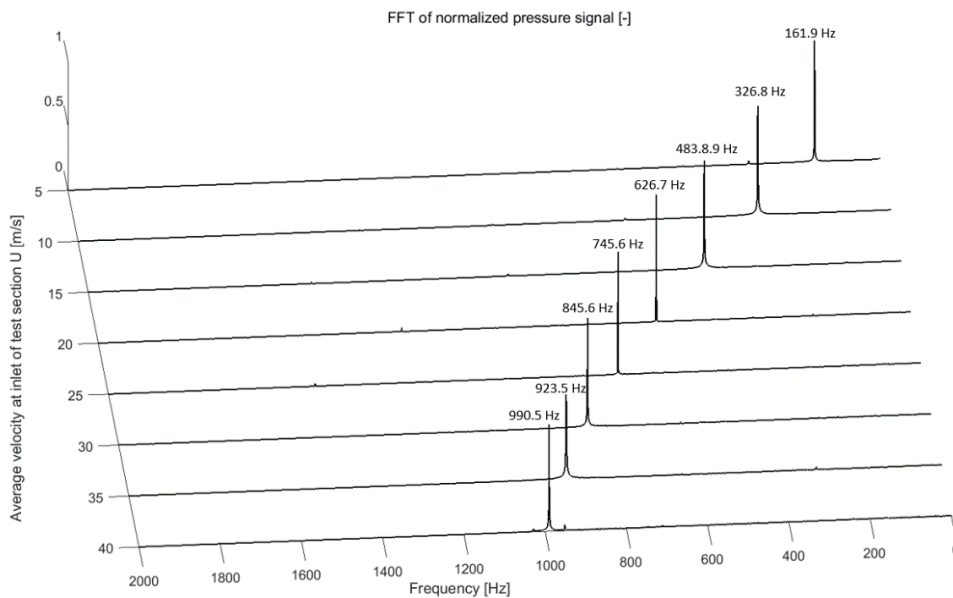


**Figure 9.** FFT of normalized pressure signal at monitor point P28 [-] Hydrofoil 2.

Hydrofoil 3 produces pressure signals where the shedding frequency is not easy to identify. Periodic shedding does not seem to be present. There are several dominant frequencies in the signal. Throughout investigations of these results will not be done here, but Hydrofoil 3 is disregarded for further studies.

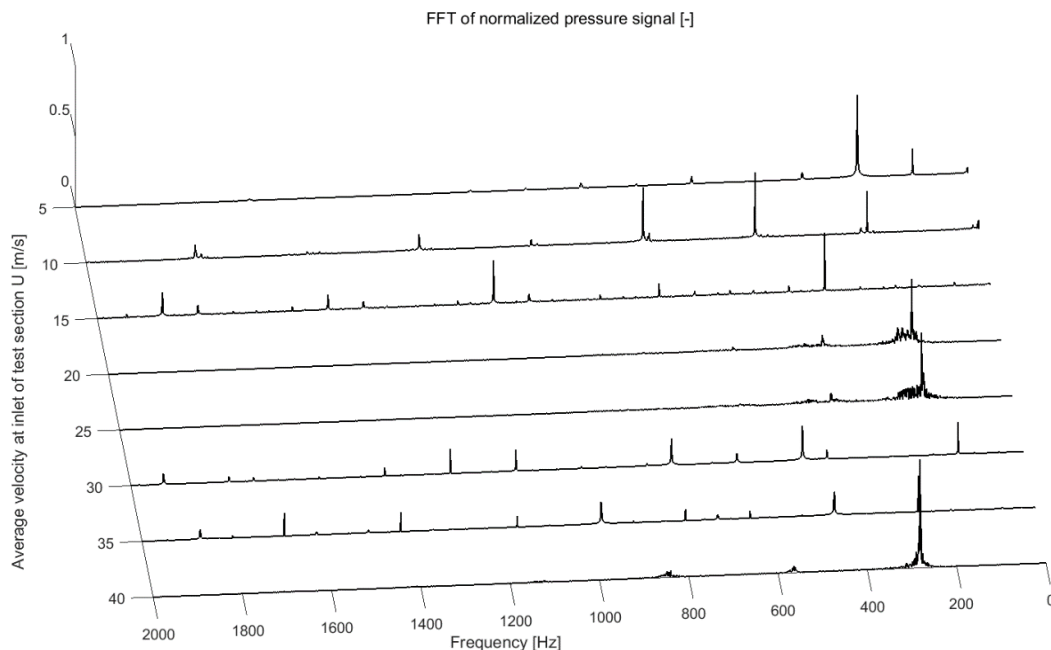


**Figure 10.** FFT of normalized pressure signal at monitor point P28 [-] for Hydrofoil 3.

#### 4. Conclusion

In this numerical study, the effect of TE shape for the cascade rig at NTNU have been investigated. The results indicate that a TE shape with less curvature than in the original design is beneficial in terms of increasing the shedding frequency in the operational range of the rig. It is anticipated that the lock-in condition may be moved by 30 % in the velocity range.

#### 5. Further work

The shedding frequency at the lock-in operational point obtained in the CFD analyses deviates from what experienced in the experiment. By performing full testing in 3D, the results may be closer to the experimental results. A blade flutter analysis on the original hydrofoil design may also provide new information. Still, the results are within a range that is close to what has been experienced, which suggests that the relative difference in the results obtained when studying new trailing edge designs are reliable. The effect of chamfering the hydrofoil as in the original design is desired, as the constant thickness hydrofoils will increase the natural frequency of the system.

#### Acknowledgement

I want to thank my supervisor Ole Gunnar Dahlhaug for an exciting topic and the great learning facilities at the Waterpower Laboratory at NTNU. I also want to thank Chirag Trivedi who has provided great help in setting the objectives of this work in addition to being a great discussion partner.

## References

- [1] Dörfler, P., Sick, M., Coutu, A., "Flow-Induced Pulsation and Vibration in Hydroelectric Machinery: Engineer's Guidebook for Planning, Design and Troubleshooting", Springer Science & Business Media, 2012, 75-77
- [2] Ducoin, A., Young, Y. L., "Hydroelastic response and stability of a hydrofoil in viscous flow", Journal of fluids and structures, 2013, 38:40-57
- [3] Brekke, H., "Pumper & Turbiner", 2003, 96-97
- [4] Jeong, J., Hussain, F., "On the identification of a vortex", Journal of Fluid Mech. vol. 285, 1994, 69-94
- [5] Ducoin, A., Loiseau, J.-Ch., Robinet, J.-Ch. "Numerical investigation of the interaction between laminar to turbulent transition and the wake of an airfoil", European Journal of Mech. B/Fluids vol. 57, 2016, 231-248
- [6] Trivedi, C., Gandhi, B., and Cervantes, M., 2013, "Effect of Transients on Francis Turbine Runner Life: A Review," Journal of Hydraulic Research, 51(2), 2012, 121-132
- [7] Trivedi, C., 2017, "A Review on Fluid Structure Interaction in Hydraulic Turbines: A Focus on Hydrodynamic Damping," Engineering Failure Analysis 77, 2017, 1-22
- [8] Gauthier, J., Giroux, A., Etienne, S., and Gosselin, F., "CFD Evaluation of Added Damping Due to Fluid Flow over a Hydroelectric Turbine Blade", Proc. 28th IAHR Symposium on Hydraulic Machinery and Systems, Grenoble, France, IAHR, 2016.
- [9] Nennemann, B., Monette, C., and Chamberland-Lauzon, J., "Hydrodynamic Damping and Stiffness Prediction in Francis Turbine Runners Using CFD", Proc. 28th IAHR Symposium on Hydraulic Machinery and Systems, Grenoble, France, IAHR, 2016.
- [10] Monette, C., Nennemann, B., Seeley, C., Coutu, A., and Marmont, H., "Hydro-Dynamic Damping Theory in Flowing Water", Proc. IOP Conf. Series: Earth and Environmental Science, IOP Publishing, 2014,32044-32053.
- [11] Coutu, A., Seeley, C., Monette, C., Nennemann, B., and Marmont, H., "Damping Measurements in Flowing Water", Proc. IOP Conference Series: Earth and Environmental Science, 2012, 062060
- [12] Yao, Z., Wang, F., Dreyer, M., and Farhat, M., 2014, "Effect of Trailing Edge Shape on Hydrodynamic Damping for a Hydrofoil", Journal of Fluids and Structures, 51(0), 2014, 189-198



## Appendix D: Risk Assessment

NTNU		Prepared by		Number		Date	
		HSE section		HMSRV2601E		09.01.2013	
HSE		Approved by		Replaces			
		The Rector				01.12.2006	
<b>Hazardous activity identification process</b>							

Unit: (Department)

Energy and Process Engineering

Date: 13.01.2017

Line manager: -

Participants in the identification process (including their function): Ole Gunnar Dahlhaug (supervisor), Sondre Leonhardsen (Student), Chirag Trivedi (Co-supervisor), Carl W. Bergan (Co-supervisor), Bjørn W. Solemslie (Co-supervisor)

Short description of the main activity/main process: Master project for student Sondre Leonhardsen. Numerical investigation of Flow Field subject to vibrating structure.

Is the project work purely theoretical? (YES/NO): YES Answer "YES" implies that supervisor is assured that no activities requiring risk assessment are involved in the work. If YES, briefly describe the activities below. The risk assessment form need not be filled out.

Signatures: Responsible supervisor:

*Ole G. Dahlhaug*

Student:

*Sondre Leonhardsen*

ID nr.	Activity/process	Responsible person	Existing documentation	Existing safety measures	Laws, regulations etc.	Comment
1	Literature study on the vortex shedding at the trailing edge of hydro profiles utilized in high head Francis turbines					
2	Parametric study of a hydrofoil in order to see the relationship between geometry and vortex shedding frequency					
3	Investigate the vortex shedding frequency versus blade flutter					
4	If there is time available: Investigate the vortex shedding frequency versus cavitation.					